National Technical University of Athens
Department of Naval Architecture and Marine Engineering
Shipbuilding Technology Laboratory

Construction of Data-Driven Models for the Identification of Large-Scale Damages in Stiffened Panel Geometries

Diploma Thesis

of

Georgios I. Aravanis

Supervised by

Konstantinos N. Anyfantis, Assistant Professor

Athens, May 2023

"When one admits that nothing is certain one must, I think, also add that some things are more nearly certain than others."

Bertrand Russell, *Am I An Atheist Or An Agnostic?* 1947

Abstract

In recent years, growing concern for the reliability of ship structures has emerged among stakeholders in the maritime sector. In looking to enable a paradigm shift towards predictive maintenance, the field of Structural Health Monitoring (SHM) has emerged as a viable option. The goal of SHM systems is to infer the existence or level of structural degradation using large amounts of in situ sensor-obtained data. In the present work, the problem of damage diagnosis in stiffened panel geometries is treated. Out-of-plane deflections of the panel's plate elements are considered as the damage case of interest, while strain response data are employed as the damage-sensitive features. By accounting for different sources of operational variability, two different approaches that rest on a probabilistic foundation are employed for damage detection. In the first, the problem is cast as one of multi-class classification, where the different classes correspond to discrete deflection levels, and a detection theory-based classifier is employed. In the second, the problem is treated as one of probabilistic regression, where the goal is to map strain readings to the probability distribution of the deflection magnitude. Both methods are implemented on a realistic stiffened panel geometry, based on an existing vessel, with all the employed data acquired through a numerical workflow that involves a high-fidelity Finite Element (FE) model and a surrogate model.

Keywords: Structural health monitoring, hull stiffened panel, uncertainty quantification, surrogate modeling, strain sensing

Περίληψη

Τα τελευταία χρόνια έχει σημειωθεί αυξανόμενο ενδιαφέρον για την αξιοπιστία των ναυπηγικών κατασκευών από τα ενδιαφερόμενη μέρη που εμπλέκονται στον ναυτιλιακό τομέα. Επιδιώκοντας την πυροδότηση μιας μεταβολής παραδείγματος προς την προγνωστική συντήρηση, ο τομέας της Παρακολούθησης Δομικής Ακεραιότητας (ΠΔΑ) κατασκευών έχει αναδειχθεί ως βιώσιμη επιλογή. Ο στόχος των συστημάτων ΠΔΑ είναι η εξαγωγή συμπερασμάτων σχετικά με την ύπαρξη ή το βαθμό δομικής υποβάθμισης, χρησιμοποιώντας μεγάλες ποσότητες δεδομένων από επιτόπιους αισθητήρες. Στην παρούσα εργασία, το πρόβλημα της διάγνωσης βλαβών εστιάζεται στις γεωμετρίες ενισχυμένων ελασμάτων. Ως βλάβες ενδιαφέροντος θεωρούνται οι βυθίσεις των επιμέρους πλακιδίων του ενισχυμένου ελάσματος, ενώ ως παράμετροι προς εποπτεία λαμβάνονται οι αποκρίσεις παραμόρφωσης του συστήματος. Λαμβάνοντας υπόψη διαφορετικές πηγές επιχειρησιακής μεταβλητότητας, δύο διαφορετικές προσεγγίσεις πιθανοθεωρητικής φύσεως χρησιμοποιούνται για τον εντοπισμό βλαβών. Στην πρώτη προσέγγιση, το πρόβλημα ανίχνευσης προσεγγίζεται ως ένα πρόβλημα ταξινόμησης πολλαπλών κλάσεων, όπου οι επιμέρους κλάσεις αντιστοιχούν σε διαφορετικά επίπεδα βυθίσεων, ενώ χρησιμοποείται ένας ταξινομητής βασισμένος στην θεωρία ανίχνευσης. Στην δεύτερη, το πρόβλημα συντάσσεται ως πρόβλημα πιθανοθεωρητικής παλινδρόμησης, όπου ο στόχος είναι η αντιστοίχιση των μετρήσεων παραμόρφωσης στις κατανομές πιθανότητας των διαφόρων μέτρων βύθισης. Και οι δύο μέθοδοι εφαρμόζονται σε μια ρεαλιστική γεωμετρία ενισχυμένου ελάσματος, βασισμένη σε ένα υπάρχον πλοίο, με όλα τα δεδομένα να εξάγονται μέσω μιας αριθμητικής ροής εργασιών που περιλαμβάνει ένα μοντέλο Πεπερασμένων Στοιχείων (ΠΣ) υψηλής ακρίβειας και ένα υποκατάστατο μοντέλο.

Λέξεις-κλειδιά: Παρακολούθηση δομικής ακεραιότητας κατασκευής, ενισχυμένο έλασμα γάστρας, ποσοτικοποίηση αβεβαιοτήτων, υποκατάστατη μοντελοποίηση, αισθητήρια μέτρηση παραμόρφωσης

Acknowledgments

The completion of my thesis would not have been possible without the support I received from numerous individuals.

First and foremost, I want to express my gratitude to my thesis supervisor, Assistant Professor Konstantinos Anyfantis, for providing me with exceptional guidance and for acting in a highly professional manner. Over the past year, he has provided me with invaluable advice, encouragement, and inspiration; his knowledge of the topic and his boundless enthusiasm for sharing it have not only led to fruitful collaboration between us, but have also truly stoked my interest in scientific research. As times were tough, it was especially his principles and good natured attitude, as well as his unwavering faith in my talents, that kept me going.

In addition to my supervisor, I owe a debt of gratitude to Ph.D. candidate, Nicholas Silionis, for his invaluable contribution to the completion of this thesis through his assistance and advice, and for always taking the time to have insightful discussions with me about the fascinating fields involved in my work. Always insightful, he never failed to praise my efforts and offer constructive criticism. As someone who has experienced only a mild taste of the cumbersome path of a researcher, I can only wish him the best of luck in his pursuit of a doctorate.

I would also like to thank my thesis committee, which consisted of Professor Nicholas Tsouvalis and Associate Professor Dimitris Vamvatsikos, for all of their helpful comments and recommendations.

To my friends, I express my appreciation for all the experiences and memories we shared during these past years and for their understanding towards this challenging period of my life.

And last but not least, I want to express my deepest gratitude to my parents, Giannis and Niki, and my sister, Eleni, for their unconditional love and support throughout my life.

Georgios Aravanis
Athens, 2023

Table of Contents

List of Figures

List of Tables

List of Acronyms

FN	false negative	22
FP	false positive	22
NLL	negative log-likelihood	34
TP	true positive	24
ANN	Artificial Neural Network	7
BGD	batch gradient descent	31
CBM	Condition-based Maintenance	2
CDF	cumulative distribution function	10
CoV	coefficient of variation	40
DL	Deep Learning	25
DOFs	degrees of freedom	17
DT	Digital Twin	3
FE	Finite Element	4
FEM	Finite Element Method	7
FPSO	Floating Production Storage and Offloading	3
IACS	International Association of Classification Societies	1
KDE	Kernel Density Estimation	22
LHS	Latin Hypercube Sampling	10
LRT	Likelihood Ratio Test	20
MAE	Mean Absolute Error	49
MC	Monte Carlo	24
MCS	Monte Carlo Simulation	7
MGD	mini-batch gradient descent	31
ML	Machine Learning	7
MLE	Maximum Likelihood Estimation	33
MLP	Multilayer Perceptron	25
MSE	Mean Squared Error	49

MVE	mean-variance estimation	32
NASA	National Aeronautics and Space Administration	3
NDT	Non-Destructive Testing	1
NP	Neyman-Pearson	24
PDF	probability density function	9
PI	prediction interval	32
PICP	prediction interval coverage probability	34
PINAW	prediction interval normalized average width	34
PNN	Probabilistic Neural Network	26
PT	Physical Twin	3
QoI	quantity of interest	10
ReLU	rectified linear unit	29
RMSprop	Root Mean Square propagation	57
ROC	Receiver Operating Characteristic	24
SGD	stochastic gradient descent	31
SHM	Structural Health Monitoring	3
SPR	Statistical Pattern Recognition	5
UQ	Uncertainty Quantification	7
WGN	White Gaussian Noise	9

[This page has been intentionally left blank.]

Chapter 1

Introduction

1.1 Current state of damage identification practices

Preservation of structural integrity is a challenging task for infrastructure systems with geometry- and operational-level complexities, such as ships, offshore and land-based structures. This task starts as early as the design phase, which is viewed as the optimal time to incorporate measures for reducing failure risk, and continues through the entire service life of the asset by planning proper preventive maintenance regimes. For ship structures, which lie within our primary area of interest, these are framed around periodic surveys and self-regulatory inspections. The former are undertaken by classification societies, which act as private third parties under the auspices of the International Association of Classification Societies (IACS), while the latter are promoted by industry initiatives [1, 2]. Due to scale, time and access constraints, inspection practitioners typically perform visual examinations on certain damage-prone locations, following empirically-derived guidelines. If the visual method does not suffice, a suitable Non-Destructive Testing (NDT) technique is deployed on-site for a more refined assessment. The current NDT methods that dominate the field can be classified into three main categories; namely, (enhanced) visual and radiographic, acoustic, and magnetic techniques [3]. Once structural damage has been identified by means of the employed inspection method, the operator must determine whether or not appropriate repair/renewal and maintenance should be performed. Selecting a suitable repair alternative involves a great deal of judgment and engineering insight, and is typically a trade-off between robustness and cost.

For a system with significant structural redundancy, like a ship structure [4], this methodology has proven effective to safeguard its integrity, primarily until the next special survey. Admittedly, however, there are several inherent limitations in visual and NDT techniques, placing current practice in a less than optimal position. The human factor is one ring of the chain that poses significant influences on the inspection outcomes, while also being very difficult to quantify due to its multivariable, complex nature. Technical constraints as well as external and/or uncontrollable factors also add up to the variables affecting the inspection performance. In any case, existing procedures, at their core, provide discrete measurement points in time and are mostly preferred to be performed in-shore, which is quite unsuited to the important concept of a continuously safe operating envelope. Given the operational and aging process stochasticity involved in ship structures, the aforementioned may precipitate unforeseeable events, which, in the worst-case scenario, may be translated into a total structural failure of the asset (i.e., hull girder collapse) with catastrophic economical, social, and environmental consequences.

Normally, the likelihood of a hull girder collapse grows with the accumulation of localized, unrepaired damage at individual structural components of the hull, which reduces their ultimate

strength performance. The risk increases even more when damage occurs to elements furthest from the ship's cross-section neutral axis (i.e., the main deck or bottom), where stresses during regular navigation are greatest. Parameters that can affect the ultimate strength of these structural elements range from material uncertainties to externally induced factors. One that is of high influence and potentially may go undetected is associated with the fabrication-related initial imperfections (i.e., initial distortions and residual stresses) [3], inherent to welded thin-walled structures. Considering that the ship structure is in essence an assembly of plates and stiffened panels, it is evident that the initial deflections of plate elements are of primary detection interest for ensuring safe structural operation. This applies particularly in the case of plates in compression, where the impact of initial deflections magnifies significantly, considering that the added destabilizing moment causes the plate to enter a pre-buckled state almost immediately after loading starts. The recent accident of the 8000 TEU containership MOL Comfort in the hogging condition (i.e., convex hull girder bending) could be cited as an example of this type. According to the relevant investigation reports [5–7], evidence suggests that the occurrence of pre-existing buckling damage in the shell plates of her midship bottom (see Figure 1.1a) most likely acted as a catalyst for the accident. Apparently then, the degraded double bottom structure in tandem with other, relatively intractable factors (e.g., misdeclared cargo weights, bottom local loads, whipping vibrations, etc.) led to an unexpected overloading scenario amidships, as seen in Figure 1.1b.

(a) (b)

Figure 1.1: Photos capturing (a) the buckling deformations observed in the bottom shell plating of a sister vessel of MOL Comfort, and (b) her condition at the time of the accident. Reproduced from Sumi et al. [7].

Although the preceding is undoubtedly not a singular example of the inadequacy of the existing conventional regime, it is one of the more profound examples illustrating the need for enabling a paradigm shift into a more holistic and proactive approach to maintenance, i.e., Condition-based Maintenance (CBM). Indeed, the maritime sector, empowered by the advancements brought by the fourth industrial revolution (Industry 4.0), has recently turned its sights towards this direction as a means of staying ahead of the competition and

globalizing. Essentially, CBM recommends maintenance actions (i.e., decisions) based on data gathered through a process of condition monitoring allowing operators to gain access to salient benefits [8]. Weighed against preventive maintenance, the primary advantages CBM offers are the increased system reliability as well as the significant cost savings due to the reduced material wastage and the decreased mean downtime as a result of less reliance on periodic inspections. The next section delves into the concepts of Digital Twin (DT) and Structural Health Monitoring (SHM), which both play an increasingly important role in the realization of the CBM paradigm.

1.2 Digital Twin technology and Structural Health Monitoring

The DT concept was originally introduced by Michael Grieves at the University of Michigan in 2002. In 2010, the National Aeronautics and Space Administration (NASA) formalized the DT concept in a draft strategic roadmap, with the intention of using it to run simulations of space capsules targeted at their service performance and operational safety upgrades [9].

From a practical perspective, a DT can be defined as the computerized companion of a real-world physical asset, i.e., the Physical Twin (PT), intended to serve as a dynamic and accurate replica of the PT's behavior within a target setting [10–12]. To ensure solid physical interpretability, the DT should be augmented with high-fidelity physics-based models, which will be constantly updated as data from permanently installed sensors on the PT will be received in a real-time fashion. The DT can then be leveraged for conducting different "what-if" scenarios of service function (i.e., operation, inspection, etc.) for the life-cycle integrity management of the PT. The extant literature underlines many of the prospective and immediate benefits of the DT intervention in the industrial arena that accumulate to the PT's overall efficiency, including risk [13] and cost [14] reduction; security [15], resilience [16], and reliability [10, 17] enhancement; and, of course, decision-making assistance [18–20].

The breadth of the aforementioned potential benefits has ignited great interest across different sectors of the engineering spectrum. Speaking of the maritime industry, it appears more natural for classification societies to incorporate DT-related technologies into their pool of future plans compared to shipping companies themselves. Namely, in [21], authors already implied that classification societies, in an effort to keep pace with digitalization, should take the initiative to proactively reduce the risk of operational errors, and, indeed, several major ones have referred to the DT concept as the backbone in their strategy for digitalization [22–24]. An example of a DT of an Floating Production Storage and Offloading (FPSO) hull structure is represented in Figure 1.2.

As a modern branch of structural engineering founded on remote data retrieval schemes, SHM plays a key role in the future trajectory of DT technology development. Essentially, the main challenge behind every SHM system deployed on a given asset is to infer the state of its structural health from (filtered and processed) in-situ sensor signal data. It is a field that

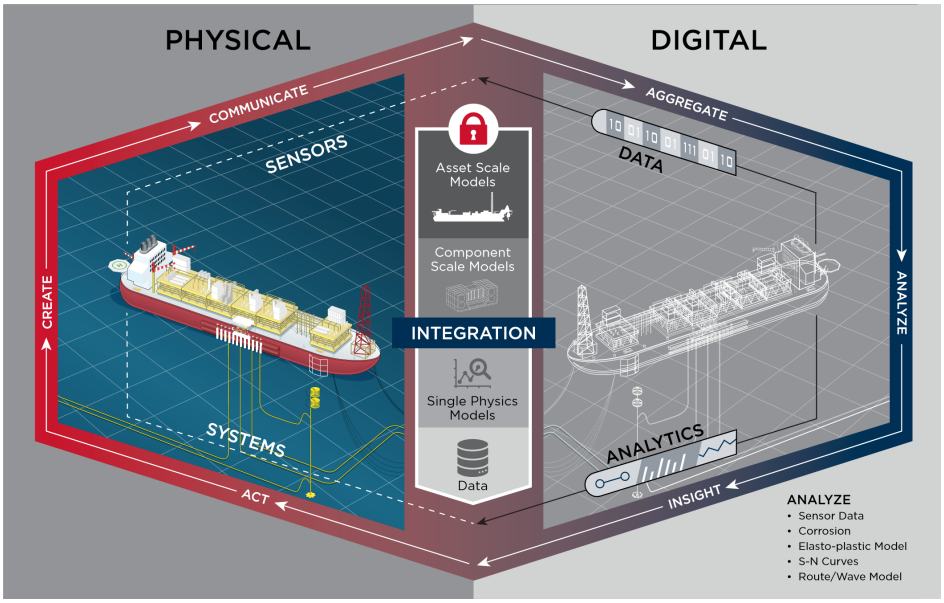

Figure 1.2: DT technology for an FPSO hull structure: Interaction between the physical space and the digital space. Reproduced from [22].

encompasses knowledge and expertise sourcing from a variety of disciplines (e.g., structural engineering, data management, computer science, etc.) and has been a major subject of study for the better part of the last four decades [25]. The three primary drivers for SHM, as discussed in the relevant literature, are: (1) the life-safety gains attainable by continuously monitoring critical components; (2) the economic benefits attainable by avoiding unnecessary inspection and maintenance actions that could result in disruptive and costly downtime; and (3) the potential for optimized performance of newly erected structures, whose health state may be monitored and, by extension, determined from the onset [26]. SHM methodologies can be broadly classified as either diagnostic or prognostic, depending on whether they are used for pre- or post-event analysis. By definition, diagnostics is intended to shed light on the presence (Level I), location (Level II), and extent (type and/or severity —- Level III) of the damage, whereas prognostics on the remaining useful life of the monitored system (Level IV) [27]. This work's center of gravity resides in the diagnostic aspect.

Regardless of the event analysis considered, SHM methodologies may be further partitioned in a formal manner into two subsets; the model-based and the data-based ones [28]. Model-based approaches use the predictions of a representative physics-based model of the target structure, typically within a Finite Element (FE) model updating setting. Therefore, any health-related decisions can be made based on the changes in the updated structural parameters. The model updating problem is an inverse problem in mathematics and, thus, has an inherent capability to implicitly quantify uncertainties arising from both inherent (physical) variability and prediction/modeling errors, bridging the gap to real-world applications. Despite the success of this approach for damage identification purposes, a critical challenge still remains. Capturing relatively small-scale damage states necessitates high-resolution FE models, which

in turn leads to a high-dimensional inverse problem that can quickly become computationally intractable. In the data-driven paradigm, SHM problems may be posed in the context of Statistical Pattern Recognition (SPR) [29], where the characteristics of the current structural condition are identified directly by analyzing, in probabilistic terms, the change of structural response patterns induced by the presence of damage. The primary distinction between the two methods resides in the fact that, in the data-driven method, only information from previously collected data (training data) is available, without the need to explicitly analyze any model. The pragmatic and agile nature of this approach equates to the real-time operation of the applied damage identification algorithm, which suits better for deploying CBM on complex systems. Propelled by the latter statement, the detection problem pursued in this work is cast within a data-driven scheme.

1.3 Vibration- and strain-based SHM methodologies

Within the framework of SHM, the damage to be identified is defined as "changes introduced into a system that adversely affect its current or future performance" [25]. As Axiom IVa of SHM states [30], however, sensors cannot directly measure damage. This indicates that measured quantities need to be collected, wherein features informative of the structure's health state lie. Both static and dynamic response data have been utilized for SHM applications. The latter approach, is broadly known as vibration-based SHM, whereas the former, as (static) strain-based SHM.

Vibration responses (i.e., accelerations, dynamic strains) and, primarily, their extracted features (e.g., vibration frequencies, mode shapes, modal curvatures, etc.) have long occupied a prominent place in SHM systems, shaping low-cost solutions suitable for continuous monitoring of large-scale structures [31–33]. Significant effort has been devoted to vibration-based damage detection and/or localization within SHM in recent research activities as well, such as those concerned with civil infrastructure systems [34–39], aerospace structures [40–42], ship hull structures [43–45], as well as with critical parts of offshore [46, 47] and onshore [48–50] wind turbines. However, small-scale damage states in extensive structures that operate under considerable ambient vibration (e.g., a localized manufacturing defect in a 250 m ship hull) can pose difficulties for conventional vibration-based techniques in distinguishing the resultant differences in the dynamic characteristics. Approaches exploiting static responses, on the other hand, are not bound by such limitations since they directly transform the strain redistribution caused by damage to information on its presence and/or extent. In this direction, a sensor layout that registers static strains might well serve the aforementioned purpose. Static strain-based approaches can be found in some legacy studies published in the pertinent literature [51, 52]. Recent studies [53–58] and practical applications [59] have effectively implemented the same principle for SHM of aerospace structures. The concept of strain-based SHM is also finding applications in the field of marine engineering. Namely, it has been used for problems concerning simplified thin-walled geometries that abstractly represent a ship

hull [60, 61], as well as a more representative structure, i.e., a marine vessel [62].

1.4 Thesis objectives and overview

The previous sections were aimed at providing a condensed version of the necessary context so that the reader naturally arrives at the centerpiece of this thesis. Namely, using the MOL Comfort accident as a motivation while acknowledging the overall added value of SHM implementation, this work envisages the design of SHM detectors capable of identifying localized damages in large-scale structures through a limited number of strain sensors. Considering that most large-scale structures operate in a stochastic environment, a crucial feature of this study is the identification and early allowance of potential sources of variability in the design phase; therein appears to lie both the challenge and the novelty value of this thesis. This can be accomplished by describing the various sources of uncertainty as basic random variables, which suggests that a probabilistic treatment of the problem is to be required.

In this direction, the present work aims to assess probabilistic neural networks and binary signal detection theory as formulation tools for the detection problem under operational and fabrication-induced geometric variability. From this point onward, these are grouped under the heading of input source variability, for the sake of brevity. For demonstration purposes, an 8000 TEU and 316 m long containership (i.e., MOL Comfort) is considered as the representation of the large-scale critical structure. The localized damage of detection interest is represented by an array of bathtub-shaped plate deflections, typical of shipbuilding and repair operations, located at the external bottom of the central hold, which exceed a deterministic maximum allowable limit. Strain response data are employed as the damage-sensitive features, obtained from a surrogate model trained on the outputs of a high-fidelity FE model.

The succeeding chapters build on the aforementioned subjects and describe in depth the rationale and procedures followed to methodically arrive at the purpose of this thesis. In Chapter 2 the theoretical underpinnings related to the concepts and tools used in this thesis are laid out. In Chapter 3 the development of the problem at hand is described followed by the details on the FE modeling procedure. The procedure behind the choice of the damage-sensitive features is presented in Chapter 4 along with the construction of the surrogate model used to alleviate the burdensome computational demands of the numerical modeling campaign. Chapter 5 features the formulation of the damage identification methods employed in this work, as well as a review of the results and discussion upon them. Finally, Chapter 6 concludes with a summary of this work, some concluding remarks on the subject, and suggestions for future extensions.

Chapter 2

Theoretical background

This chapter presents in theoretical terms the basic concepts and tools of analysis tied with the technical portion of this thesis. By the end of this chapter, the reader should have a solid understanding of the concepts such as Statistical Pattern Recognition (SPR), Uncertainty Quantification (UQ), Monte Carlo Simulation (MCS), surrogate modeling, Finite Element Method (FEM), detection theory, and Artificial Neural Networks (ANNs). For a further exposure to the discussed topics, the interested reader is referred to the cited references encountered throughout this chapter.

2.1 SHM as a problem in Statistical Pattern Recognition

Pattern recognition is not a new field of research; applications around the topic trace back up to the early 1970s. In its most basic definition, it may be defined as a tool dedicated to the automated recognition of regularities in data. Basic mathematical models framed around a shared domain concerning a particular application can oftentimes be used to extract patterns from a data-set and associate them with different classes. In the early 1990s, however, it was realized that rather of depending on models designed by researchers to classify data, machines could be used to learn from the data and use that knowledge to generate the most probable outcome (i.e., prediction) of an unseen event. The outcome of this prediction is the product of Statistical Pattern Recognition (SPR) algorithms, which are part of the broader field of Machine Learning (ML).

In the context of SHM, the SPR paradigm starts with sensor data from the monitored structure and ends with damage identification to assess its structural condition. The goal is to distinguish between variations of the measured response associated with the healthy state under operational and environmental variability, and those related to damaged structural conditions. In accordance with the description provided by Farrar et al. [63], the SPR paradigm can be partitioned into four stages: (1) operational evaluation; (2) data acquisition; (3) feature extraction and generation; and (4) statistical model development. Inherent in the last three stages are the numerical physics-based models and the ML algorithms.

Typically, the ML algorithms employed in statistical model development fall into one of the following categories:

(i) Group classification: In this case, the algorithm predicts a discrete class label for a given input.

(ii) Regression analysis: In this case, the algorithm predicts one or more continuous variables.

(iii) Outlier detection: In this case, the algorithm is expected to only indicate whether or not the data originates from normal operating conditions.

The appropriate algorithm is selected based on whether supervised or unsupervised learning is possible, which is directly tied to data availability, as well as on the characteristics of the data to be analyzed. Supervised learning refers to the training of algorithms with data derived from the structure in both its intact and damaged states. In this case, group classification and regression are the most common tasks. Unsupervised learning refers to the case where all available training data come from the undamaged state. This type of learning suits well for outlier detection. However, it only gives indications about the presence of damage. Conversely, in the supervised mode, the statistical algorithms can be used to address the entirety of the damage identification hierarchy. The present study focuses on supervised learning, as the problem at hand solely involves fully labeled data obtained numerically using a Finite Element (FE) model.

Consistent with the aims of the SPR paradigm, this study employs a probabilistic framework to tackle the damage identification problem from two different perspectives. In the first, the problem is viewed through the prism of detection theory [64]. In this setting, damage identification is treated as a discrimination problem (binary and potentially, multi-class classification) in which classes are associated with different levels of deflection. Detection theory-based classifiers rely on a robust probabilistic foundation and are therefore capable of capturing uncertainty present in the data as well as quantifying predictive uncertainty, since they are assessed through performance metrics that quantify the risk associated with a decision. In the SHM literature, this is a prevalent and well-established methodology [62, 65–69].

In the second, the damage identification problem is expressed by casting it as one of probabilistic regression. In this case, the goal is to learn a mapping between features of interest (i.e., in our case strain readings), and a quantity that can be considered as an indicator of damage (i.e., plate deflection magnitude), or more accurately, a probability distribution of that quantity. By setting an appropriate threshold on the latter, that signifies the existence of damage, then the problem of damage identification can be tackled directly. This approach has been implemented using a variety of techniques, including Bayesian neural networks [70], Gaussian process regression [71, 72], and probabilistic neural networks [73, 74], the latter of which will be employed in the current study.

2.2 Probabilistic analysis of structures and Uncertainy Quantification

2.2.1 Sources and types of uncertainty

There is no argument that, in practice, structural systems are subject to a multitude of uncertainty sources. Uncertainties generally fall into two categories; namely, aleatoric and epistemic [75]. The concept of “aleatoric uncertainty” is related to the unavoidable inherent randomness or variability of the systems. Aleatoric uncertainty in engineering problems may become present in structural loads, as well as in material properties, structural dimensions (scantlings), and fabrication-related geometric tolerances, just to mention a few. Errors associated with

the deployed data acquisition system (e.g., measurement noise, sensor misplacements, etc.) also fall under this category. Essentially, inherent variability is a state of nature, and the accompanying uncertainty is irreducible; in layman's terms, aleatoric uncertainty is something we have to live with. Due to its random nature, it is typically described in probabilistic terms with a probability density function (PDF). In contrast, epistemic uncertainty is associated with the discrepancies in relation to the real state of nature that result from the lack of knowledge/modeling errors in general. Foremost among the sources of epistemic uncertainty is the prediction error related to the computational modeling procedures that have gained popularity in the last decades for several applications of practical interest in science and engineering. Theoretically, the uncertainty associated with these types of errors can be reduced by employing better physical-mathematical models or gathering additional data. From a more practical standpoint, the prediction error component is oftentimes represented under an idealized additive White Gaussian Noise (WGN) assumption, together with the uncertainty arising from measurement noise.

2.2.2 Monte Carlo Simulation-based UQ

The response of a system subject to uncertain inputs is inherently stochastic. Uncertainty quantification (UQ) is gaining increasing importance in computational analysis of complex physical systems, particularly in the areas of risk analysis, reliability analysis, and decision-making. Within a forward propagation framework, UQ analyzes and quantifies the impact of input uncertainties on the system response. Typically, the system is represented by a deterministic computational model $\mathcal{M}$ (e.g., an FE model). The input is described as a random vector $\mathbf{X}$ that includes d possibly coupled parameters, and has a joint PDF denoted as $f_{\mathbf{X}}$. The computational model converts a specific realization of $\mathbf{X} = \mathbf{x}$ into an uncertain output $y = \mathcal{M}(\mathbf{x})$, which, for the sake of simplicity, is assumed here to be an observed realization of a univariate random variable Y. The generalization to multivariate outputs is trivial.

In UQ problems, various properties of Y, such as its underlying PDF f_Y, its moments, and its sensitivity to the different components X_i of $\mathbf{X}$, are of interest. Specifically, to estimate the main statistical descriptors of the outputs represented by $Y \sim f_Y$, the mean value can be expressed as:

$$\mu_Y = \mathbb{E}[y] = \mathbb{E}[\mathcal{M}(\mathbf{x})] = \int_{S_{f_{\mathbf{X}}}} \mathcal{M}(\mathbf{x}) f_{\mathbf{X}}(\mathbf{x}) d\mathbf{x} \tag{2.1}$$

where $S_{f_{\mathbf{X}}} = \{\mathbf{x} \in \mathbb{R}^d : f_{\mathbf{X}}(\mathbf{x}) > 0\}$ is the support of $f_{\mathbf{X}}(\mathbf{x})$; subsequently, the variance can be expressed as:

$$\sigma_Y^2 = \mathbb{V}[y] = \mathbb{V}[\mathcal{M}(\mathbf{x})] = \mathbb{E}[\mathcal{M}^2] - \mathbb{E}[\mathcal{M}]^2 \tag{2.2}$$

Considering that $\mathcal{M}$ is often a complex model that is explicitly unknown, the integrals in these equations are analytically intractable. The system's behavior can only be determined in a point-by-point fashion in relation to the inputs $\mathbf{x}^{(j)}$ sampled from $f_{\mathbf{X}}$, where the model

generates responses $y^{(j)} = \mathcal{M}(\mathbf{x}^{(j)})$ (non-intrusive or "black-box" method). The standard, and most general, method for tackling problems of this type is the Monte Carlo Simulation (MCS) method.

MCS is a sampling-based approach that is used to compute summary statistics for the quantity of interest (QoI) and evaluate its probability density. To approximate the integrals in Equation 2.1 and 2.2, sampling methods rely on the law of large numbers. Essentially, the concept behind it is that the PDF of the QoI can be estimated by repeatedly running the simulation with inputs randomly drawn from their corresponding PDF. There are three steps in its implementation:

1. Random sampling: Draw N_{MC} points $\mathbf{x}^{(j)}$ as independent and identically distributed (i.i.d) samples from $f_{\mathbf{X}}$ using a random number generator that usually implements the inverse-transform technique (see [76] for further details).
2. Numerical experimentation: Evaluate the output for the jth sample, $y^{(j)} = \mathcal{M}(\mathbf{x}^{(j)})$.
3. Statistical analysis: Compute the statistics on the discrete output points $y^{(j)}$.

Elaborating on the third step, the expected value of Y in Equation 2.1 can be estimated as:

$$\mu_Y = \frac{1}{N_{MC}} \sum_{j=1}^{N_{MC}} y^{(j)} = \frac{1}{N_{MC}} \sum_{j=1}^{N_{MC}} \mathcal{M}(\mathbf{x}^{(j)}) \tag{2.3}$$

while the unbiased estimate of the variance (Equation 2.2) is computed as:

$$\sigma_Y^2 = \frac{1}{N_{MC} - 1} \left(\sum_{j=1}^{N_{MC}} \left(y^{(j)} \right)^2 - N_{MC} \mu_Y^2 \right) \tag{2.4}$$

MCS has many advantages, including being non-intrusive, robust, versatile, and easy to apply. Particularly, its prediction capability remains robust against the problem of high dimensionality in the probabilistic UQ framework, owing to the randomization of all input variables for each sample. However, because it is a sampling technique, the obtained results are subject to sampling errors. According to the central limit theorem [77], the statistical error of mean μ_Y and variance σ_Y^2 is proportional to the square root of the sample size N_{MC}, which means that to get another digit of accuracy (factor of 10) requires about 100 times more samples. This makes MCS a very time-consuming method, rendering its application impracticable for simulations with great complexity and detail.

One method for achieving converged statistics with fewer iterations is Latin Hypercube Sampling (LHS). LHS is a well-known sampling technique based on a random process that achieves a better representation of the parameter space than pure random sampling, which exhibits clustering. One-dimensional LHS is implemented by splitting the cumulative distribution function (CDF) F_X of a random variable X into n equal partitions (called strata;

LHS is a stratified approach) and then selecting a random data point in each partition, i.e., $F_X(x_i)$. This method has the advantage of guaranteeing that at least one value from each partition is included in the sample. An example of LHS is illustrated in Figure 2.1. The y-axis displays a small number of indicative samples drawn from the uniform distribution. The points are evaluated using the inverse CDF F_X^{-1} represented by the arrows going through F_X (as described before) for a standard normal distribution. If sufficient samples are collected, the resulting distribution will correspond to the PDF representing X. This approach can be extended to any distribution.

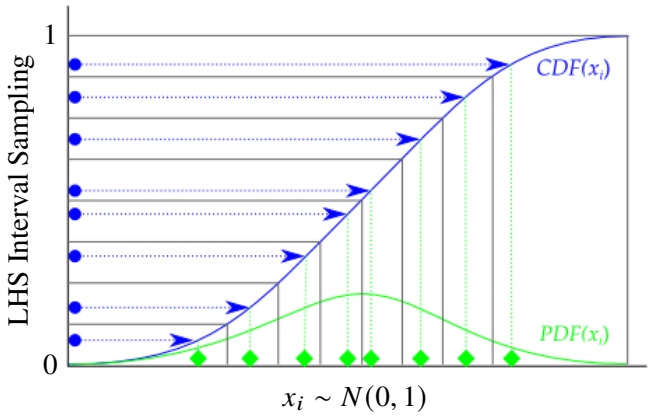

Figure 2.1: An example of LHS with a normal distribution. Reproduced from [78].

2.2.3 Surrogate modeling

The computational costs of UQ within a statistical simulation scheme, such as the one described before, requires the use of surrogate modeling to gain computational efficiency. Surrogate modeling, also known as metamodeling, refers to the practice of constructing an approximate, yet less expensive, representation of the input-output relationship of a complex, physical process. The produced model can then be evaluated at negligible cost to predict the outputs for a new set of inputs that exist within the initial observation domain. The rise of Machine Learning (ML) and data-driven modeling has made the concept of surrogate modeling even more viable, with potential applications in many areas, including SHM [79–82], materials science [83, 84], radiation dosimetry [85], and many others.

In general, a surrogate model does not maintain any virtual representation of the exact nature of the physical system of interest, but rather approximates its complex behavior exclusively based on a finite set of simulation data (support points) without requiring problem-specific knowledge (black-box model). Therefore, operational (e.g., loads) or state (e.g. damage features) information about the structure is integrated within the constructed surrogate model, allowing immediate access to predictions when a batch of input data is obtained from the system. As the approximate function is created based on the information carried by the support points, it is essential to generate informative pairs of data samples. To this end, the employed physics-based model $\mathcal{M}$ is typically exploited within a simulation framework, which ends up

with a list of data points (or better known as training data), expressed as:

$$\left\{\mathbf{x}^{(j)}; \mathbf{y}^{(j)}\right\} \tag{2.5}$$

Where $\mathbf{x}^{(j)}$ is the jth input vector from the sampling plan, and $\mathbf{y}^{(j)}$ includes the corresponding outputs from evaluating the model $\mathcal{M}$, i.e., $\mathbf{y}^{(j)} = \mathcal{M}(\mathbf{x}^{(j)})$. The learning stage of the surrogate models is usually undertaken offline, whereas only the evaluation of model predictions occurs during the online stage, allowing for future re-use and re-production. In case of changes to the physical system, however, the surrogate model normally needs to be retrained.

Depending on the degree of non-linearity of the mapping function a different modeling approach may be used. Among the most prevalent approximation approaches are linear/polynomial regression, Gaussian processes, neural networks, and support vector machines, to name a few. In this work, a standard feed-forward back-propagation Artificial Neural Network (ANN) was employed to construct a surrogate that learns a mapping between the parameters describing the input source variability and the strain response. The ANN model is selected due to its advantages in estimating complex functions over high-dimensional manifolds, as well as its re-usability and the modern hardware technologies built for deep learning. In addition, using gradient descent and back-propagation greatly minimizes the optimization procedure's computational expense. These terms are defined in further detail in the section related to ANNs.

2.3 Preliminaries on Finite Element procedures

The recent advances in computational resources have allowed the development of high-fidelity numerical models to address the increased complexity of modern engineering systems. This work makes use of such a model to generate a sufficient amount of structural response data (i.e., strains) that is necessary for training the employed surrogate model. For its formulation, the Finite Element Method (FEM) was employed, which is a widely used numerical technique for the simulation of complex physical phenomena. The following are the basic theoretical components of FEM tailored to the scopes of the present study.

2.3.1 Formulation of the Finite Element Method

The FEM is a discretization method for the approximate solution of partial differential equations pertaining to complex domains. Essentially, the physical system that may be of interest, such as the component shown in Figure 2.2, is reduced to a discrete form of simpler constituent parts, referred to as finite elements, interconnected at a discrete number of nodes. Of course, this abstraction cannot precisely reflect the response of the continuum, which is described by variables at an infinite number of points. For solving structural mechanics problems, the standard approach is the displacement-based FEM [86]. In this case, the analyst seeks to calculate the displacement field of the model, a method that has been initially used in

the analysis of beams and truss structures. The displacement-based FEM is a very general formulation and provides the basis of almost all FE analyses in practice. Its formulation is based on the idea of virtual work, which is similar to the Ritz/Galerkin method to minimize the system's total potential (see [86]).

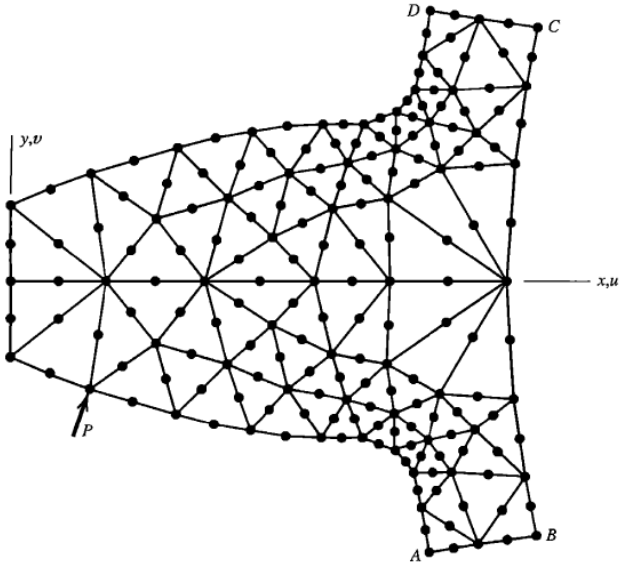

Figure 2.2: Two-dimensional model of a gear tooth comprised of triangular elements. Reproduced from Cook [87].

To demonstrate the general FEM formulation as approached in [86], let us suppose a general 3D body in steady-state conditions that is adequately supported on the area S_u with prescribed displacements $\left\{\mathbf{U}^{S_\mathrm{u}}\right\}$. The body is considered to be subjected to surface loads $\left\{\mathbf{f}^{S_\mathrm{f}}\right\}$ on the surface area S_f, body forces $\left\{\mathbf{f}^{B}\right\}$, and concentrated forces $\left\{\mathbf{F}^{i}\right\}$ where i denotes the point where the load is applied. Generally, these forces have three components corresponding to the three coordinate axes X, Y, Z:

$$\begin{aligned}\left\{\mathbf{f}^{S_\mathrm{f}}\right\} &= \left[f_X^{S_\mathrm{f}},\ f_Y^{S_\mathrm{f}},\ f_Z^{S_\mathrm{f}}\right]^T,\\ \left\{\mathbf{f}^{B}\right\} &= \left[f_X^{B},\ f_Y^{B},\ f_Z^{B}\right]^T,\\ \left\{\mathbf{F}^{i}\right\} &= \left[F_X^{i},\ F_Y^{i},\ F_Z^{i}\right]^T\end{aligned} \tag{2.6}$$

The displacements of the body from the unloaded configuration are:

$$\{\mathbf{U}\} = [U,\ V,\ W]^T \tag{2.7}$$

where we demand $\{\mathbf{U}\} = \left\{\mathbf{U}^{S_\mathrm{u}}\right\}$ on S_u. The strains corresponding to $\{\mathbf{U}\}$ are:

$$\{\boldsymbol{\varepsilon}\} = [\varepsilon_{XX},\ \varepsilon_{YY},\ \varepsilon_{ZZ},\ \varepsilon_{XY},\ \varepsilon_{YZ},\ \varepsilon_{ZX}]^T \tag{2.8}$$

and are related to $\{\mathbf{U}\}$ through the well-known strain-displacement relations of the form:

$$\begin{aligned} \varepsilon_{XX} &= \frac{\partial U}{\partial X}; \quad \varepsilon_{YY} = \frac{\partial V}{\partial Y}; \quad \varepsilon_{ZZ} = \frac{\partial W}{\partial Z} \\ \varepsilon_{XY} &= \frac{\partial U}{\partial Y} + \frac{\partial V}{\partial X}; \quad \varepsilon_{YZ} = \frac{\partial V}{\partial Z} + \frac{\partial W}{\partial Y}; \quad \varepsilon_{ZX} = \frac{\partial W}{\partial X} + \frac{\partial U}{\partial Z} \end{aligned} \tag{2.9}$$

The stresses corresponding to $\{\boldsymbol{\varepsilon}\}$ are:

$$\{\boldsymbol{\sigma}\} = [\sigma_{XX},\ \sigma_{YY},\ \sigma_{ZZ},\ \tau_{XY},\ \tau_{YZ},\ \tau_{ZX}]^T \tag{2.10}$$

where

$$\{\boldsymbol{\sigma}\} = [\mathbf{C}]\,\{\boldsymbol{\varepsilon}\} + \{\boldsymbol{\sigma}'\} \tag{2.11}$$

with $[\mathbf{C}]$ denoting the constitutive matrix and the vector $\{\boldsymbol{\sigma}'\}$ denoting given initial stresses. Therefore, the problem to be solved is defined by the geometry of the body, the external loads acting upon it, the boundary conditions, the material law and the initial stresses. Ultimately, the goal is to determine the displacement field, which in turn allows us to calculate the strains and stresses involved.

At this point, we can concisely state the principle of virtual work, i.e., that the total virtual work performed by actual forces through geometrically compatible virtual displacements is zero for a system in equilibrium. This can be stated as:

$$\int_V \left\{\overline{\boldsymbol{\varepsilon}}\right\}^T \{\boldsymbol{\sigma}\}\, dV = \int_V \left\{\overline{\mathbf{U}}\right\}^T \left\{\mathbf{f}^B\right\} dV \ + \ \int_{S_\mathrm{f}} \left\{\overline{\mathbf{U}}^{S_\mathrm{f}}\right\}^T \left\{\mathbf{f}^{S_\mathrm{f}}\right\} dS \ + \ \sum_i \left\{\overline{\mathbf{U}}^i\right\}^T \left\{\mathbf{F}^i\right\} \tag{2.12}$$

where $\left\{\overline{\mathbf{U}}\right\}$ is the virtual displacement field and $\left\{\overline{\boldsymbol{\varepsilon}}\right\}$ denotes the corresponding virtual strains. As indicated earlier, the fundamental concept of FEM is the approximation of the body as an assemblage of finite elements, which are connected through nodal points along their boundaries. In each element, the displacements are assumed to be a function of the displacements at the nodes. Therefore, for a given element e, we can write:

$$\{\mathbf{u}\}^{(e)} = [\mathbf{H}]^{(e)} \left\{\hat{\mathbf{U}}\right\} \tag{2.13}$$

where $[\mathbf{H}]^{(e)}$ is the matrix of shape functions, the superscript e indicates the element e, and $\left\{\hat{\mathbf{U}}\right\} = [U_1 V_1 W_1 \quad U_2 V_2 W_2 \quad \ldots \quad U_N V_N W_N]^T$ is a $3N$-dimensional vector containing all nodal displacements. The mathematical expression of the shape functions is defined when selecting the element types to be set into the model. This is generally an application-dependent task and consists a crucial part in FEM as the shape functions essentially dictate the nature of the approximation of the field quantity (i.e., the displacement). To meet displacement compatibility, the shape functions should offer displacement continuity within the elements

and across the interrelement boundaries. Physically, these constraints ensure that there are no gaps or overlaps as elements deform.

With the assumptions on the displacements in Equation 2.13 the corresponding element strains can be evaluated,

$$\{\boldsymbol{\varepsilon}\}^{(e)} = [\mathbf{B}]^{(e)} \left\{\hat{\mathbf{U}}\right\} \tag{2.14}$$

where $[\mathbf{B}]^{(e)}$ is the matrix of derivatives of shape functions constructed based on the relations of Equation 2.8. The strain compatibility requirement is automatically satisfied when continuity of the displacement field is valid.

Finally, the stresses in a finite element follow from inserting the element strains into Equation 2.11,

$$\{\boldsymbol{\sigma}\}^{(e)} = [\mathbf{C}]^{(e)} \{\boldsymbol{\varepsilon}\}^{(e)} + \{\boldsymbol{\sigma}'\}^{(e)} \tag{2.15}$$

where $[\mathbf{C}]^{(e)}$ is the constitutive matrix of element e, and $\{\boldsymbol{\sigma}'\}^{(e)}$ are the given element initial stresses.

By rewriting Equation 2.12 as a sum of integration over the volume and areas of all finite elements, one may deduce the equilibrium equations that correspond to the finite element assemblage:

$$\begin{aligned}\sum_e \int_{V^{(e)}} \left\{\overline{\boldsymbol{\varepsilon}}\right\}^{(e)T} \{\boldsymbol{\sigma}\}^{(e)} \, dV^{(e)} = \sum_e \int_{V^{(e)}} \left\{\overline{\mathbf{U}}\right\}^{(e)T} \left\{\mathbf{f}^B\right\}^{(e)} dV^{(e)} \\ + \sum_e \int_{S_1^{(e)} \ldots S_q^{(e)}} \left\{\overline{\mathbf{U}}^S\right\}^{(e)T} \left\{\mathbf{f}^S\right\}^{(e)} dS^{(e)} \; + \; \sum_i \left\{\overline{\mathbf{U}}^i\right\}^T \left\{\mathbf{F}^i\right\}\end{aligned} \tag{2.16}$$

where $e = 1, 2, \ldots, k$ with k being the total number of elements, and $S_1^{(e)} \ldots S_q^{(e)}$ denotes the element surfaces that are part of the body surface S.

Substituting the virtual displacements and strains in the above equation with the expressions given by Equation 2.13 and Equation 2.14, yields:

$$\left\{\overline{\hat{\mathbf{U}}}\right\}^T \left[\sum_e \int_{V^{(e)}} [\mathbf{B}]^{(e)T} [\mathbf{C}]^{(e)} [\mathbf{B}]^{(e)} \, dV^{(e)}\right] \{\hat{\mathbf{U}}\} = \left\{\overline{\hat{\mathbf{U}}}\right\}^T \{\mathbf{R}\} \tag{2.17}$$

In order to obtain the equations for the unknown nodal point displacements, we use the principle of virtual work by imposing unit virtual displacements for all components of $\left\{\overline{\hat{\mathbf{U}}}\right\}$. The result is:

$$[\mathbf{K}]\{\hat{\mathbf{U}}\} = \{\mathbf{R}\} \tag{2.18}$$

The matrix $[\mathbf{K}]$ is the stiffness matrix of the element assemblage,

$$[\mathbf{K}] = \sum_e \int_{V^{(e)}} [\mathbf{B}]^{(e)T} [\mathbf{C}]^{(e)} [\mathbf{B}]^{(e)} \, dV^{(e)} \tag{2.19}$$

and $\{\mathbf{R}\}$ is the load vector that includes the effect of the element body forces expressed as equivalent forces on every node.

The preceding formulation demonstrates that the principle of virtual displacements incorporates the three conditions that must be satisfied in a structural problem; equilibrium, compatibility, and the constitutive law. It should be stressed that the first criterion is satisfied in an average or integral sense, as equilibrium within each element cannot be achieved in its entirety. With an appropriate FE discretization, however, the differential equation of equilibrium is satisfied more precisely as the mesh of the elements is repeatedly refined.

2.3.2 FE modeling of stiffened thin-walled structures

Thin-walled structures are to be found in various engineering fields, especially in the field of shipbuilding. This has been justified by the demand for structural systems that are optimized to be lighter, more efficient, and offer increased strength and stiffness. The ship hull structure is an excellent example of thin-walled structures, as it can essentially be viewed as a box girder composed of several stiffened panels that comprise plates together with primary and secondary structural members. A typical stiffened panel structure can be displayed in Figure 2.3. A distinctive characteristic of this type of structures is that one of the dimensions of their main structural components is much smaller than the rest, i.e., their thickness. In light of this, it is reasonable to ponder over the earlier realization and suppose that 2D plane (membrane) elements are adequate for modeling thin-walled structures. However, in realistic applications, a ship operates under a complex system of loads with several localized effects. Membrane elements, by their very nature, are unable to sustain out of plane loading leading to the alternative of 3D solid or 2D shell elements. On the other hand, solid elements require a relatively higher computational cost in contrast to shell elements. Therefore, shell elements can operate as a compromise between those two extremes offering reliable and effective model representations for thin-walled structures.

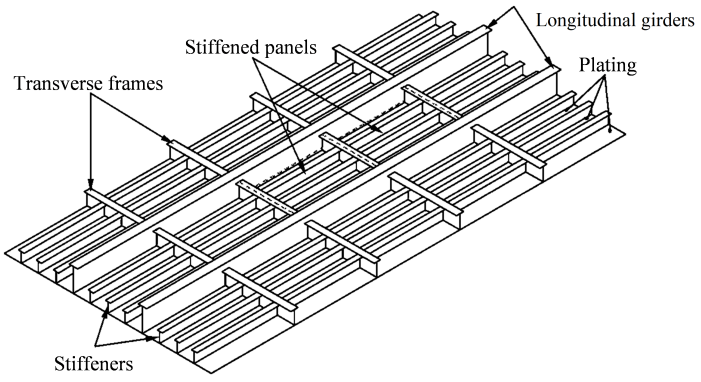

Figure 2.3: Typical stiffened panel structure. Reproduced from Paik [88].

Regarding beam structural members, these can be analyzed by a sequence of different mathematical models, each one yielding a different prediction accuracy level. Namely, an

hierarchy of models ranging from Bernoulli or Timoshenko beam theory to a full three-dimensional continuum is at the analyst's disposal. In this context, studying the structural response of beam structural members in detail lies beyond the scope of this work. It is thus evident that using beam elements instead of solid or shell elements to represent beam members in a stiffened geometry is the optimal choice for this matter, as the latter ones would provide unnecessary and costly accuracy. At this point, further information on beam and shell elements is provided.

Starting with beam elements, these are typically defined by two or three nodes and are abstracted to 1D elements by storing the 2D cross-section as separate beam section property. This reduced representational scheme offers large computational time savings. The most comprehensive model that can be thought of for a beam element is the spatial one, which simultaneously carries axial, bending, and torsional loads. This means that, at each node of the beam, there are three translational displacements in the x, y, and z directions, and three rotational degrees of freedom (DOFs) with respect to the x, y, and z axes. A typical FE beam with six DOFs per node along with the local element reference frame and the associated Cartesian coordinates system are shown in Figure 2.4.

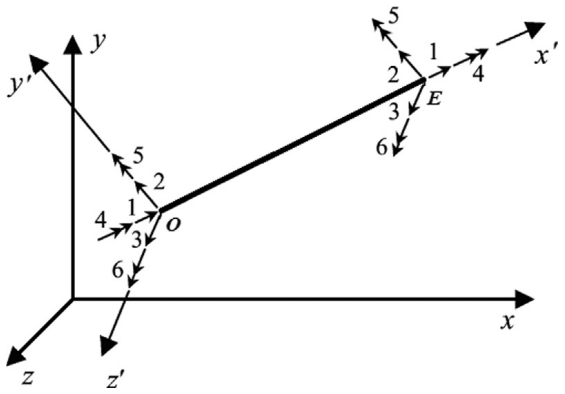

Figure 2.4: 3D beam element with six DOFs at each node in local coordinates. Reproduced from Goda et al. [89].

Beam elements are very widely used in structural engineering and are well-suited for linear, large rotation, and large strain nonlinear applications of any slender or stout structural entity. Generally, the applicability of the element may be assessed using the slenderness ratio of a beam structure. For large ratios (slender beam), the Bernoulli-Euler beam theory holds, and for smaller ones (stout beam), the Timoshenko beam theory prevails. Nevertheless, overly "thick" beams cannot be analyzed by 1D beam elements due to the limitations of Timoshenko's shear deformation theory, as variations in the distribution of shear stresses cannot be accounted for. As for their stiffness properties, these can be calculated in many cases by the solution of the differential equations of equilibrium, and such derivations are well-established in the literature. However, it can be also effective to evaluate the stiffness matrices using the FE formulation, i.e., the virtual work principle described earlier, in particular when considering

complex beam geometries [86].

Shell elements are 2D elements but can incorporate both bending and membrane actions, with their physical thickness represented implicitly via the underlying mathematical model of a given element formulation. Generally, they are are either triangular or quadrilateral in terms of their shape. For higher-order schemes, quadrilateral shells are preferred as they provide better results, numerical stability, and accuracy. A quadrilateral shell element is typically defined by four, eight, or nine nodes with three translational and three rotational DOFs at each node. However, in many cases, shell element formulations do not include a rotational DOF about the local z-axis, which is often termed as the drilling DOF.

To formulate a general shell element, two approaches have been established. First, shell elements can be developed directly through the superposition of plane stress and plate bending elements, and therefore the ingredients for obtaining the necessary stiffness matrices are available in elements already described in the literature. This approach is suited for the formulation of flat shells or facets, which are a special case of the general curved shell element. Figure 2.5 illustrates a flat rectangular shell element in a local coordinate system xyz, subject simultaneously to "in-plane" (far-right) and "bending" (middle) actions.

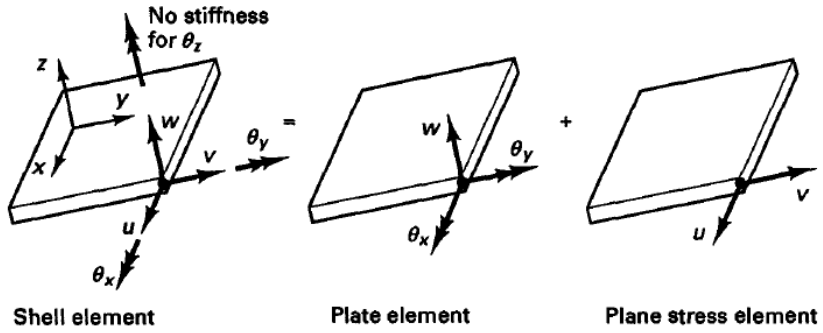

Figure 2.5: Formation of flat shell element. Reproduced from Bathe [86].

Second, shell elements can be formed by using degenerated isoparametric continuum elements, as illustrated in Figure 2.6. The first degenerated shell element was introduced by Ahmad et al. [90]. The initial step in this process is to discretize directly the 3D continuum equations. Then, by incorporating the assumptions that originals normal to the middle surface are inextensible and remain straight, and that elastic modulus in the normal direction is zero, the 3D formulation is degraded. This approach provides the most general shell element formulation as it is not dependent upon any shell theory, with the reduction to the resultant form typically carried out numerically rather than analytically. This formulation occupies a middle ground between facets and curved elements based on classical shell theory that is obviously more complex mathematically.

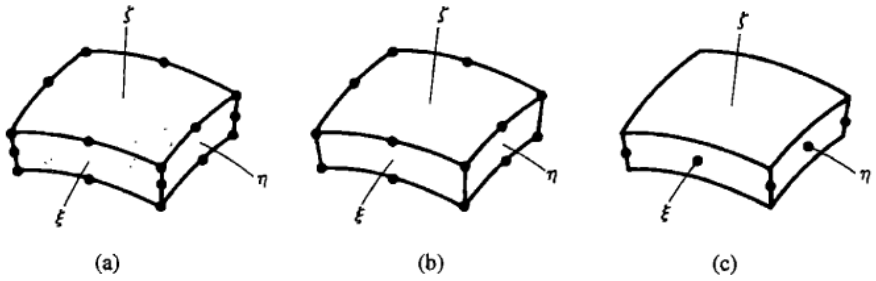

Figure 2.6: (a) A 20-node solid element. (b) Elimination of four midedge nodes yields a 16-node element. (c) Further constraint yields an eight-node element. Reproduced from Cook [87].

2.3.3 Modeling and validation procedures

Modeling is the simulation of a physical structure or process using an analytical or numerical substitute selected in accordance with the phenomenon to be predicted. On the basis of this definition, it is evident that the mathematical model adopted controls the accuracy of the physical problem to be described. For an analyst, a thorough understanding of the physics of the underlying problem, as well as the behavior and constraints of each element type, is necessary to successfully complete the FE modeling procedure. In essence, the expected behavior of the structure, i.e., the consequent mode of deformation in terms of structural mechanics, should be aligned with how elements are able to behave and the intended boundary conditions.

In addition, anticipating the variations related to the gradients of the field quantity in a qualitative and/or quantitative manner is pivotal in obtaining a good mesh structure. The mesh density level must be defined in a way that avoids too coarse of a discretization leading to inadequate representations, or unnecessarily fine discretization leading to a waste of computational resources. Moreover, in many cases where common sources of stress concentrations exist in the model (e.g., openings, fillets, etc.), a "graded mesh" (i.e., a gradation of element sizes) should be implemented to provide a more detailed modeling of these regions. Such a technique provides essential efficiency for reducing the computational burden without sacrificing accuracy. It is, however, more an art and experience than a predetermined sequence of steps, as no general rule exists on either the number or the size of elements that guarantee good accuracy.

The FE modeling process is completed once the boundary conditions are prescribed correctly. Boundary conditions of a mechanical system include the external loads and imposed displacements, both of which should appear at a node. Applying boundary control is to ensure that a unique solution can be obtained. More specifically, in order to avoid singularities during matrix decomposition, constraints must be sufficient to prevent all possible rigid-body motions. However, more often than not, boundary conditions are not obvious in a real-world problem, and the classic notions of support conditions do not apply exactly. Defects of a

poorly executed boundary control are identified either by error messages from the software or by the unexpectedly deformed shape of the structure due to misrepresented supports. Similar considerations apply to the determination of loads.

Finally, the analyst should validate the results in as many ways as reasonably possible after obtaining a solution. This ensures that the generated results are in line with both the analyst's expectations and the laws of physics. Displacements should be examined first, as these are the primary results from which strains and stresses are derived. Unexpected deformations, directions, and magnitudes in the displacement field indicate that the solution derived should not be trusted and should be revised. A further and most crucial stage of validation is comparing FE results with results acquired in other ways, whether that is from analytical solutions, existing similar structures, experiments, or even expectations of the analyst. Ultimately, the FE model is considered acceptable if the obtained results are realistic and the error estimates obtained from the aforementioned comparison are small. Otherwise, the procedure should be repeated once the model has been modified to achieve satisfactory results.

2.4 Detection theory

The field of detection theory arose with the development of communications and radar technology during the past century [91]. Peterson et al. developed the basic principle in 1954 [92] as a method for determining the effectiveness of statistical tests and classifiers. Later in 1966, it was employed in psychophysics; see, e.g., Swets & Green [93].

Detection theory follows directly from the theory of statistical hypothesis testing [64] and consists of a range of techniques for designing optimal detectors for signals buried in noise. In this light, detection theory can be considered as well-suited for SHM, which by definition seeks to transform data that include uncertainty into decisions on the health state of the system.

2.4.1 Damage detection

For a given damage detection problem, the goal is to correctly decide whether damage is present or not. This dichotomy directly indicates the use of the Likelihood Ratio Test (LRT) principle, which is, in essence, a statistical hypothesis test involving two mutually exclusive hypotheses. Naturally, the same tools can be used for multi-class problems, i.e., deciding among multiple possible statistical situations, as will be the case in this work. However, since this can be accomplished by simply extending the principles of the binary case, it will be omitted for the sake of brevity.

In this context, one of the two competing hypotheses is conventionally referred to as the null hypothesis H_0, and the other as the alternative hypothesis H_1. The former is naturally assumed as the healthy state H and the latter as the damaged state D of the system when it comes to damage detection. The data that serves as the basis for the decision is collected in an d-dimensional random vector $\mathbf{x}$, where d corresponds to the number of installed sensors. In the general case, vector $\mathbf{x}$ is considered to follow a multivariate distribution, with joint probability

density function (PDF) $f_H(\,\cdot\,;\boldsymbol{\Theta}_H)$, $f_D(\,\cdot\,;\boldsymbol{\Theta}_H)$ in the healthy and damaged states, respectively. The distribution parameter vectors $\boldsymbol{\Theta}_H, \boldsymbol{\Theta}_D \in D_{\boldsymbol{\Theta}_H}, D_{\boldsymbol{\Theta}_D} \subset \mathbb{R}^{d_{\boldsymbol{\Theta}}}$ are deterministic, and can be estimated from the available data, according to the employed distribution model, e.g., in the case of the multi-normal distribution they correspond to the mean vector and covariance matrix. Ultimately, the detection problem can be stated formally as the problem of testing between:

$$\begin{aligned} H_0 \equiv H: &\quad \mathbf{x} \sim f_H(\mathbf{x};\boldsymbol{\Theta}_H) \\ H_1 \equiv D: &\quad \mathbf{x} \sim f_D(\mathbf{x};\boldsymbol{\Theta}_D) \end{aligned} \tag{2.20}$$

Given some vector $\mathbf{x}'$ of observations, one can link $\mathbf{x}'$ with one of the two health states (H or D) by comparing the conditional probability of H occurring, $\Pr(H\,|\,\mathbf{x}')$, with the one of D occurring, $\Pr(D\,|\,\mathbf{x}')$. To be more exact, we say that $\mathbf{x}'$ is associated with D if and only if $\Pr(D\,|\,\mathbf{x}')$ is greater than $\Pr(H\,|\,\mathbf{x}')$, and vice versa, or mathematically given by:

$$\Pr(D\,|\,\mathbf{x}') \underset{H}{\overset{D}{\gtrless}} \Pr(H\,|\,\mathbf{x}') \tag{2.21}$$

In most cases, these probabilities are not readily available, hence Bayes' rule is applied to derive the following expressions:

$$\Pr(H\,|\,\mathbf{x}') = \frac{f_H(\mathbf{x}'\,|\,H)\Pr(H)}{f(\mathbf{x}')} \tag{2.22}$$

$$\Pr(D\,|\,\mathbf{x}') = \frac{f_D(\mathbf{x}'\,|\,D)\Pr(D)}{f(\mathbf{x}')} \tag{2.23}$$

In both instances, the evidence term $f(\mathbf{x}')$ in the denominator is identical, therefore it can be cleared from the equation. Moreover, the prior probabilities $\Pr(H)$ and $\Pr(D)$ for each class can normally be regarded as being equivalently probable. Considering all of this, we define the LRT as:

$$L(\mathbf{x}') = \frac{f_D(\mathbf{x}';\boldsymbol{\Theta}_D)}{f_H(\mathbf{x}';\boldsymbol{\Theta}_H)} \underset{H}{\overset{D}{\gtrless}} \gamma \tag{2.24}$$

where $L(\cdot)$ is the likelihood ratio and $\gamma \in (0, +\infty)$ is the decision threshold which helps in making decision either in favor of H or D by partitioning the feature space, such that:

$$\begin{cases} \mathbf{x}' \in S_H\,|\,H \text{ is true} \\ \mathbf{x}' \in S_D\,|\,D \text{ is true} \end{cases}, \quad S_H, S_D \subset \mathbb{R}^d \tag{2.25}$$

It is evident that the problem of damage detection using LRT-based detectors within a supervised learning regime boils down to the selection of the appropriate probability models that capture the likelihood functions $f_H(\mathbf{x}\,|\,H)$ and $f_D(\mathbf{x}\,|\,D)$, given the available data. This is a distinct problem that could be treated using several methods. Representative examples of such methods include probability plots, goodness-of-fit tests, and Kernel Density Estimation (KDE). The non-parametric method of KDE is an appealing option in that it does not require a priori specification of any particular functional form, which can potentially produce unnecessary bias (i.e., systematic error) in the employed procedure. Therefore, it is selected as the default tool in the process of the formulation of the first damage identification technique. A PDF estimated by KDE in the univariate case may be defined from a finite data sample as follows:

$$\hat{f}_h(x) = \frac{1}{mh}\sum_{i=1}^{m} K\Big(\frac{x - x_i}{h}\Big), \quad x \in \mathbb{R},\ h > 0 \tag{2.26}$$

where x_i refers to the ith observation out of a total of m observations in the available data-set, h is known as the bandwidth, and K is the kernel function. Similarly, KDE can be extended for the multivariate case:

$$\hat{f}_{\mathbf{H}}(\mathbf{x}) = \frac{1}{m\,|\mathbf{H}|}\sum_{i=1}^{m} K\Big(\mathbf{H}^{-1}\,(\mathbf{x} - \mathbf{x}_i)\Big), \quad \mathbf{x} \in \mathbb{R}^d \tag{2.27}$$

where $\mathbf{H}$ is a non-singular matrix generalizing the univariate bandwidth h. For more details on kernel functions and kernel methods the reader may refer to [94].

2.4.2 Performance criteria

In testing H versus D, or any pair of hypotheses in general, the decision of whether to reject or fail to reject the null hypothesis carries the risk of incorrectly inferring a hypothesis that does not reflect the true state of affairs. This amount of risk can be formally represented by the well-known Type I and Type II errors in the context of classical hypothesis testing. A Type I error, or false positive (FP), occurs when the test falsely rejects the null hypothesis, which in the case of damage detection means that the structure's condition has been identified as damaged when actually the opposite holds. A Type II error, or false negative (FN), refers to the case where the alternative hypothesis is falsely rejected, or in diagnostic terms, the case in which the structure is incorrectly diagnosed as being in the healthy state.

Tied to the errors made by the test are the performance criteria. Two important performance criteria are the probability of detection P_{D} (also called true positive rate), which corresponds to the probability of declaring damage detection under D, and the probability of false alarm P_{FA} (also called false positive rate), which refers to the probability of declaring damage detection under H. The former is defined as the complement probability associated with Type II error, while the latter is equivalent to Type I error. Mathematically, they can be expressed

using the following integrals:

$$P_{\mathrm{D}} = \Pr\{L(\mathbf{x};\boldsymbol{\Theta}_H,\boldsymbol{\Theta}_D) > \gamma; D\} = \int_{\varepsilon_T}^{+\infty} f_D(\mathbf{x};\boldsymbol{\Theta}_D)dx \tag{2.28}$$

$$P_{\mathrm{FA}} = \Pr\{L(\mathbf{x};\boldsymbol{\Theta}_H,\boldsymbol{\Theta}_D) > \gamma; H\} = \int_{\varepsilon_T}^{+\infty} f_H(\mathbf{x};\boldsymbol{\Theta}_H)dx \tag{2.29}$$

The aforementioned metrics are included in the schematic of Figure 2.7 for an indicative univariate case of a binary detection problem, as the shaded areas under the curves. As indicated by Equation 2.28 and 2.29, these performance metrics depend on the detection threshold γ, which, in turn, corresponds to a strain response threshold, denoted by ε_T, in tandem with the methodology applied in this study. For a given problem, the detector should be formulated to deliver the highest accuracy level by maximizing P_{D} and minimizing P_{FA}. However, there is an inherent trade-off between these two metrics, and a single, ideal threshold value that optimizes both simultaneously cannot be found. Therefore, the selection of the decision boundary is application-dependent and is frequently determined by failure criteria, inspection regulations, etc. When economic concerns drive SHM applications the goal is to minimize Type I errors, or, equivalently, minimize P_{FA}, whereas when life safety issues drive the SHM systems the goal is to minimize Type II errors, or, equivalently, maximize P_{D}.

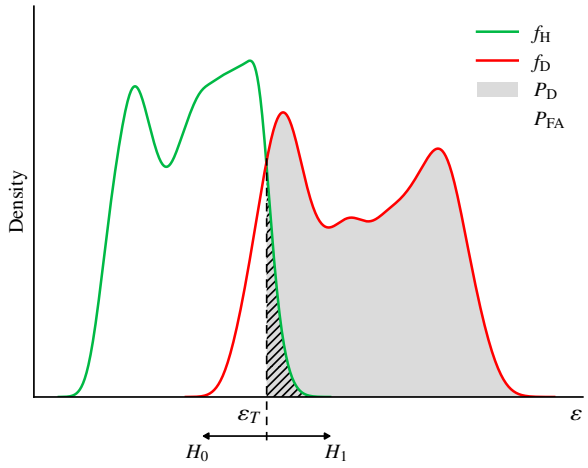

Figure 2.7: Schematic representation of binary classification problem and associated error types.

When hypothesis D is only rarely true, the primary factor in the average total cost of a system is connected to Type I errors, which result in some costly action to be taken in vain. In these conditions it is desirable for the observer to determine an affordable value of P_{FA} and to seek a decision strategy that attains this value while simultaneously maximizing P_{D}. Therefore, for a desirable $P_{\mathrm{FA}} = \alpha$, where α is the significance level of the test, Equation 2.29 can be solved with respect to the decision threshold as indicated by Equation 2.30:

$$\varepsilon_T = F_H^{-1}(1 - P_{\mathrm{FA}}\,|\,H) \tag{2.30}$$

where $F_H^{-1}(\cdot)$ is the inverse CDF under H. The obtained threshold value can then be employed for the calculation of the P_{D} according to Equation 2.28. This approach to optimal decision-making is known as the Neyman-Pearson (NP) criterion for damage detection [64].

2.4.3 Receiver Operating Characteristic (ROC) curves

A common way to holistically assess the performance of a binary detector is through the use of Receiver Operating Characteristic (ROC) curves. The ROC curve essentially shows P_{D} as a function of P_{FA} (see Figure 2.8) as the decision threshold spans through all possible values. This means that each point on the ROC curve belongs to a particular threshold, despite the fact that the threshold values are not obvious from the plot. The effect of modifying the threshold point is illustrated in Figure 2.8a along with the corresponding ROC curve in Figure 2.8b.

The diagonal line (dash line) that separates the ROC space into two areas represents a classifier that makes random classifications. Any point within the upper-left triangle indicates that the classifier has some understanding of the classes; the closer the ROC plot is to the upper-left corner, the greater the classifier's overall accuracy. Conversely, every point in the lower-right triangle indicates that the classifier is performing worse than random, i.e., the classifier possesses some knowledge about the classes but applies it improperly.

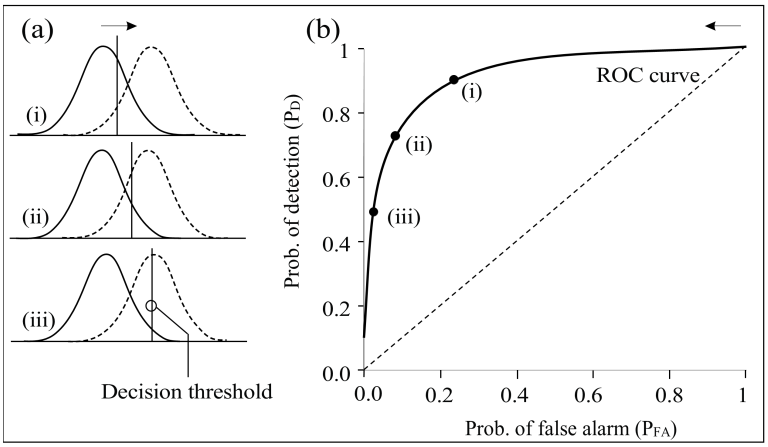

Figure 2.8: The correlation between the decision threshold (a) and the position on the ROC curve (b). By shifting the threshold to the right, the ROC curve points are obtained from right to left.

In most cases, the expressions defining the performance metrics are not available in closed form, which makes computational methods the only rational choice for their calculation. Monte Carlo (MC)-based schemes are arguably the most commonly used such methods and are based around the following principle. Namely, a sample of available data of size m is passed through Equation 2.24 and for a given threshold value, the true positives (TP) and false positives (FP) are tallied. Then, the P_{D} can be estimated as the true positive rate, i.e., TP/m, while the P_{FA} as the false positive rate, i.e., FP/m. Considering that, as already discussed, KDE-based PDFs were exclusively used throughout this work, MC methods were similarly used exclusively for the calculation of the performance metrics. The aforementioned

procedure will be described in greater depth in the section where the LRT-based detector is formulated.

2.5 Artificial Neural Networks

2.5.1 Introduction

Human-level intellectual and processing power capabilities are coming from the biological neural network that is composed of numerous chemically connected neurons; the functional units of the nervous system. Neurons take in information from several sources and each one produces a distinct output that can be, in turn, transmitted to other neurons. These functional units are essentially connected to one another via axons and dendrites, and the connecting sites between those two neuron parts are known as synapses. Synaptic architecture and strength frequently change in response to environmental stimuli, which is how learning occurs in organisms [95].

Although Artificial Neural Networks (ANNs), indisputably, do not reach the complexity of the brain, the study of these computing systems has been inspired by the simplified description of the biological mechanism above. As a matter of fact, there are two key similarities between ANNs and their biological counterparts [96]. First, the building blocks of both networks are simple computational units configuring a densely interconnected, parallel structure, and, second, the connections between neurons determine the function of the network. With this underlying rough analogy now established, it is believed that to aid the discussion, things must be put into perspective by first providing a concise definition of what ANNs are and how they function before diving deeper into their constituent parts. In this brief introduction to ANNs, focus will be placed on the fully connected, feed-forward ANN or Multilayer Perceptron (MLP), which is the most common and general-purpose ANN type.

Learning with ANNs is intrinsically connected with the term Deep Learning (DL), a specific subfield of ML that excels at handling unstructured data. Essentially, ANNs are intelligent pattern recognition techniques that use a densely interconnected network of neuronodes to learn ever deeper layers of meaningful representations [97]. Just as external stimuli are needed for learning in biological organisms, the external stimulus in ANNs is provided by the training data containing examples of input-output pairs of the function to be learned. Training inputs flow sequentially between layers, and each transition applies a new transformation to the incoming representation of the dataset. Each connection linking the neurons is assigned a weight that reflects its strength from one layer to the next. These weights are a set of numerical values that contain the information learned by the network. More specifically, their values are changed in a way that minimizes a certain loss function between the expected and current model output, with the help of an optimization function that implements the back-propagation algorithm. By gradually changing the weights of neurons over numerous inputs and outputs, the computed function is progressively refined to achieve more accurate predictions in future

calculations. Once properly trained, the ANN is able to make good predictions for unseen inputs as long as the latter lie within the training domain. This ability is referred to as model generalization.

In the following subsections, an attempt is made at providing insights into the concepts of network architecture, activation functions, and model training. A subsection is also dedicated to a class of probabilistic data-driven models called Probabilistic Neural Networks (PNNs), which are used in the second damage identification approach of this work.

2.5.2 Architecture

An artificial neuron is a simple mathematical model and the building block of an ANN. The basic architecture of a neuron is shown in Figure 2.9. The input layer contains a set of m nodes, connected to neuron k, that transmits m features $[x_0, \ldots, x_j, \ldots, x_m]$ with respective weights $[w_{k0}, \ldots, w_{kj}, \ldots, w_{km}]$ to an output node u_k. The term w_{k0} with $x_0 = +1$ acts as an equivalent of the bias value b_k that increases or decreases the net input in order for the neuron to span a target input range. The resulting products are summed up in a linear combination through a summing junction Σ. The output of the summing junction is then filtered by a selected activation function $\phi(\cdot)$, which determines the output y_k of the neuron. The aforementioned are summarized in mathematical terms by the following equations:

$$\begin{aligned} u_k &= \sum_{j=1}^{m} w_{kj} x_j + b_k = \sum_{j=0}^{m} w_{kj} x_j \\ y_k &= \phi(u_k) \end{aligned} \tag{2.31}$$

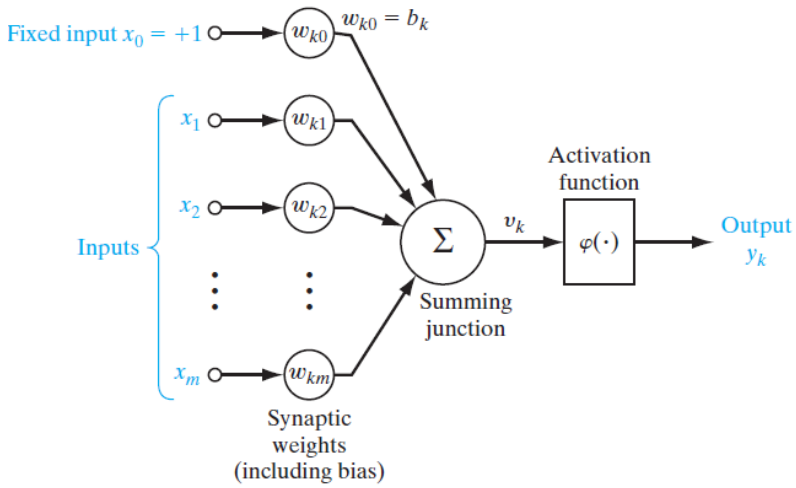

Figure 2.9: Basic structure of an artificial neuron. Reproduced from Haykin [98].

The arrangement of neurons in a neural network is referred to as the network topology or architecture. The type of architecture used in ANNs is intrinsically linked to the learning algorithm. ANN architectures can be loosely classified as either single- or multi-layer networks. This subsection discusses these architecture styles.

Single-layer perceptrons

The perceptron model was proposed by Rosenblatt [99] as an algorithm capable of supervised learning. The perceptron is the simplest version of an ANN and is, basically, a linear type classifier that can be applied for binary decision problems. It only contains a single neuron whose synaptic weights and bias can be adjusted. According to the perceptron convergence theorem given by Rosenblatt, convergence is only assured if the patterns used to train the perceptron fall neatly into two linearly distinct classes. Between the two classes, a hyperplane will represent the decision boundary.

In a layered model, the neurons are arranged in a layered fashion. The simplest structure of this model type is the single-layer network, where one or many input units compose an input layer connected to one or many output units that constitute the output layer. There is no signal transmission between the neurons in the output layer and their counterparts in the input layer (i.e., feed-forward or acyclic network). Since no computing occurs at the input layer, this layer is disregarded and the network is referred to as a single-layer network or single-layer perceptron. An indicative architecture of a single-layer perceptron is shown in Figure 2.10. A single-layer network with m output neurons clearly corresponds to m separate perceptrons.

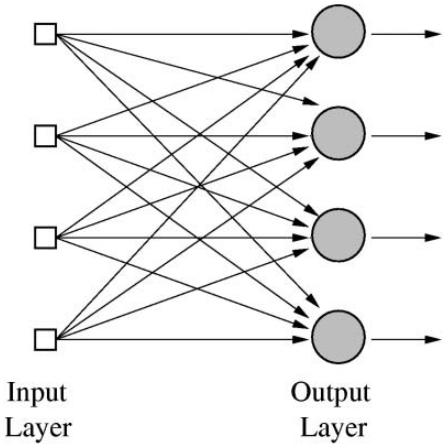

Figure 2.10: Indicative architecture of a single-layer perceptron.

Multilayer perceptrons (MLPs)

A multilayer perceptron (MLP) is the leading paradigm of feed-forward ANNs finding applications in numerous domains. To train this class of ANN models a feed-forward, supervised learning technique is implemented. The architecture of an MLP comprises an input layer, hidden layer(s), and an output layer, where connections are always made on a forward, layer-by-layer basis. Within a strict feed-forward MLP setting, a neuron on layer i always connects to a neuron on layer $i + 1$, with no internal loops nor skipping layers being allowed. It is evident that this type of network represents a generalization of single-layer perceptrons.

MLPs are used in conjunction with the back-propagation algorithm, which performs two phases of data flow; in the feed-forward phase, the inputs for a training instance are fed into the

network and propagated forward through the hidden layers, whereas in the backward phase, the predicted outcome is compared to the observed value leading to a prediction error; the weights of the network are updated right after in accordance with the error signal. Hence the name "back-propagation".

An indicative architecture of an MLP with more than two hidden layers may be seen in Figure 2.11. As indicated by the direction of the arrows, information processing flows from left to right layer-wise.

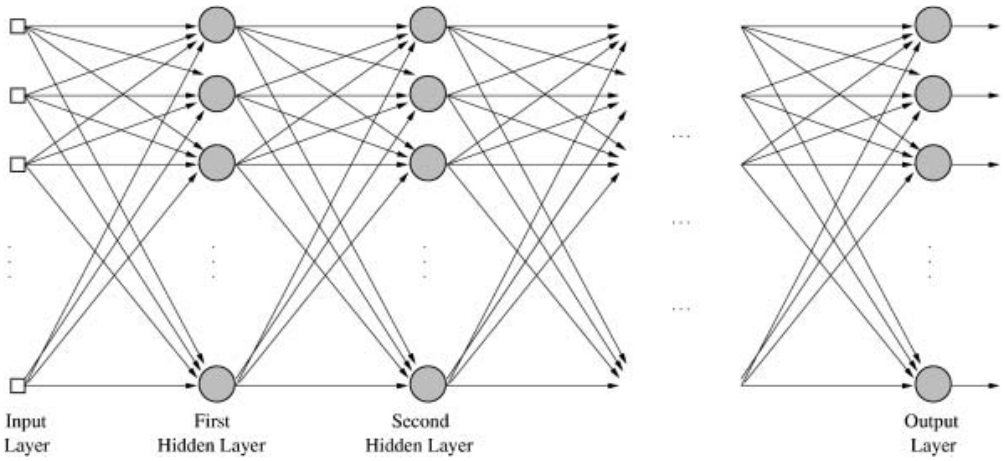

Figure 2.11: Indicative architecture of a multilayer perceptron.

2.5.3 Types of activation functions

Activation functions are a key component in ANNs as they add non-linearity to the network. This property becomes significant when a transition is made from the single-layered perceptron to the multi-layered architectures. If a neural network simply employs linear activations, its representational capacity will not be enhanced compared to a single-layer linear network, regardless of how deep the network may be. This derives from the fact that the repeated application of many linear transformations is itself a linear transformation. Additionally, of critical importance for the neural network design is the choice of the output layer activation, as it defines the type of predictions the model can make. To choose activation functions sensibly, it is generally necessary to assess their monotonicity, range, and differentiability as these properties affect the learning and generalization capabilities of ANNs. Some activation functions that are regularly employed are now presented, concretely.

One of the classical activation functions $\phi(\cdot)$ used in the earliest days of neural network development is the Heaviside step function, also known as the unit step function. The step function serves as a threshold that decides whether or not the neuron generates a signal; its derivative is zero at all values of u other than the selected threshold value, where it is discontinuous and non-differentiable, as seen in Figure 2.12a. The formula of the Heaviside

step function is:

$$\phi(u) = \begin{cases} 1 & \text{if } u \geq 0 \\ 0 & \text{if } u < 0 \end{cases} \tag{2.32}$$

Another standard activation function is the sigmoid function. The sigmoid function is a differentiable approximation of the Heaviside step function and was, for many years, the most popular tool of choice for introducing non-linearity in ANNs. Its output exists within $[0, 1]$, which is useful for doing computations that should be interpreted as probabilities. The mathematical formulation of the sigmoid function is as follows:

$$\phi(u) = \frac{1}{1 + \exp(-u)} \tag{2.33}$$

The hyperbolic tangent function, or tanh, has a similar structure to the sigmoid function, with the exception that it is rescaled horizontally and translated vertically to $[-1, 1]$. When both positive and negative outputs are sought for classification problems, the tanh function is preferred over the sigmoid function. In addition, its mean-centering and greater gradient (due to stretching) make it easier to train than the sigmoid. The tanh activation function is formulated as:

$$\phi(u) = \frac{\exp(2u) - 1}{\exp(2u) + 1} \tag{2.34}$$

As illustrated in Figure 2.12b and 2.12c, the primary issue with sigmoidal functions is that their derivative goes to zero as $|u| \to \infty$, which slows down the learning process of gradient-based networks. This is particularly the case in deep-structured architectures; when the gradient propagates and multiplies backward through each layer, the gradient's effect on the network parameters becomes insignificant. Thus, the network scarcely learns from the training instances.

The rectified linear unit (ReLU) function tackles the problem of vanishing gradients by having a gradient of one for positive inputs, and zero for negative inputs. ReLU is also computationally efficient since it does not involve the evaluation of an exponential or any other computation-intensive process. Additionally, the present function introduces sparsity in the model, which may lead to multiple benefits, such as the increased likelihood of sparse representations being linearly separable and the absence of highly entangled information, typical of ANNs that use dense representations [100]. As a result of these mathematical properties, ReLU has become the de-facto activation function in DL. The mathematical formulation of the ReLU function is given by Equation 2.35 while an indicative graph is shown in Figure 2.12d:

$$\phi(u) = \max(0, u) \tag{2.35}$$

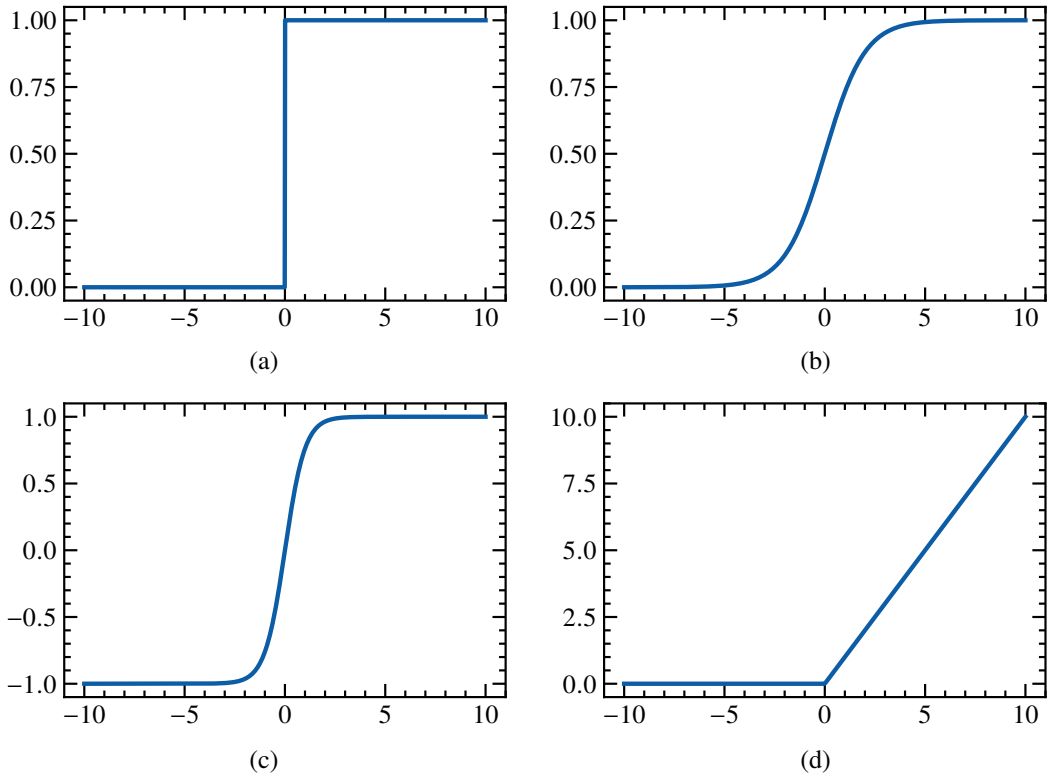

Figure 2.12: Various activation functions; namely, (a) Heaviside, (b) sigmoid, (c) tanh, and (d) ReLU.

2.5.4 Training process

Fundamentally, the basic concept of ANN model training is based on a maximum likelihood estimate in which the unknown parameters (i.e, weights and biases) are optimized such that the observed data obtain the greatest probability of occurrence conditioned on the inputs [101]. This is translated into the minimization of a scalar function, known as the loss function L, which is defined in terms of the predicted and observed values of the model. Mathematically, this can be expressed as:

$$\boldsymbol{\theta}^* = \underset{\boldsymbol{\theta}}{\operatorname{argmin}} \sum_{j=1}^{m} L(\hat{y}_j(\boldsymbol{\theta}), y_j) \tag{2.36}$$

where $\boldsymbol{\theta} = [w_1, w_2, \ldots, w_n]^T$ is the unknown parameter vector (i.e., n weights and biases), $\boldsymbol{\theta}^*$ contains the optimal values of $\boldsymbol{\theta}$, y is the observed value in the training sample, $\hat{y}$ denotes the predicted outcome, and m is the number of training instances. The loss function can generally be any function that is differentiable and several types are reported in the literature [97]. Their use depends on the specific task at hand. For example, in classification problems, the loss function might be based on the number of correctly classified examples. In regression problems, the loss function might be based on the mean squared error between the predicted and true values.

At the beginning of training, the unknown weights and biases are initialized at random and then

tuned iteratively to minimize the loss function. The calculations at the heart of ANNs involve matrix multiplications and activation functions. Since these operations are all differentiable, and the unknown parameter vector is typically high-dimensional, gradient-based optimization algorithms naturally come to the forefront. Analytically calculating the gradient of the loss function ∇L for each neuron is one naive way for estimating the gradient, considering the considerably large number of neurons of modern ANNs. On the other hand, since their structure is a composition of many differentiable simple functions chained together, the application of automatic differentiation is well-suited. The back-propagation algorithm, whose concept was introduced earlier, is a special case of automatic differentiation and is nowadays built into distributed training frameworks, like TensorFlow.

Among the existing gradient-based optimization methods, the steepest (or gradient) descent method is the most common option in ANN training owing to its simplicity. Despite not being the most efficient one, gradient descent has proved to be a successful optimization method for ML problems. Normally, gradient descent only gives convergence to some local minimum; however, it has been shown that differences between local minima and the real global minimum become trivial as the complexity of the model increases. Because of the slow nature of gradient descent in ML, the training process can be optimized by carefully defining a pre-selected parameter known as the learning rate α. Typically, as the conclusion of training approaches, the learning rate is decreased gradually to prevent falling short of the minimum.

The gradient at each update step can be calculated on all training data available; this is known as batch gradient descent (BGD). Essentially, BGD takes the average gradients across all data points to update the network's parameters. On large datasets, it is evident that this procedure is computationally expensive, but is guaranteed to converge to the global minimum for relatively smooth error manifolds. Stochastic gradient descent (SGD) is an alternative to BGD that calculates gradients using a single random training sample at each step. SGD can more easily escape shallow local minima due to the stochasticity introduced and thus speeds up the algorithm. One drawback of stochasticity is that the loss function does not decrease monotonically and does not converge to the real minimum. In order to reach the global minimum, one approach is to gradually decrease the learning rate throughout the training process. Mini-batch gradient descent (MGD) is a strategy that strikes a middle ground between BGD and SGD. MGD randomly takes a certain number of instances, i.e., mini-batches, to calculate model error. This method combines the advantages of the two preceding methods to provide the optimal balance between stability, speed, and memory requirements.

The mathematical description of the update rule of gradient descent along with the gradient of the loss function with respect to the parameter vector is now presented in Equation 2.37. In

Figure 2.13 a visual example of gradient descent down a 2D loss surface is presented.

$$\nabla L(\boldsymbol{\theta}) = \left[\frac{\partial L}{\partial w_1}, \frac{\partial L}{\partial w_2}, \ldots, \frac{\partial L}{\partial w_n}\right]^T$$
$$\boldsymbol{\theta} = \boldsymbol{\theta} - \alpha \nabla L(\boldsymbol{\theta}) \tag{2.37}$$

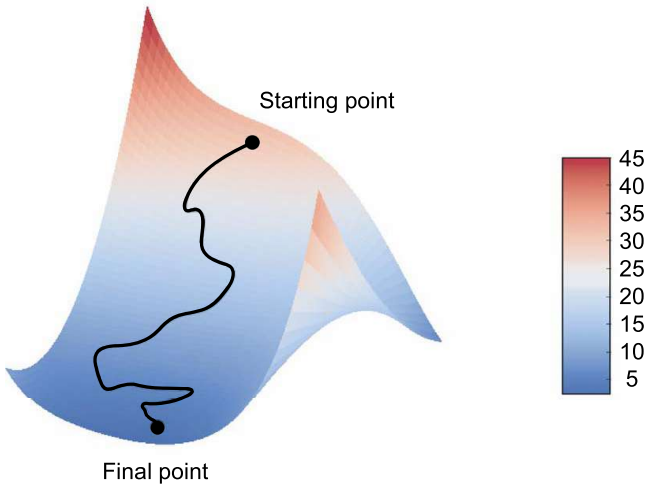

Figure 2.13: Illustration of a 2D loss surface atop the parameter space (two learnable parameters) and successful discovery of an optimum solution using gradient descent. Reproduced from Chollet [97].

2.5.5 Probabilistic Neural Networks

The nature of ANNs as universal function approximators makes them powerful tools to capture any complex nonlinear relationship between variables. One drawback of standard point estimate ANNs, however, is that they do not provide uncertainty measures for the model output in regression tasks; in the case of classification, contrariwise, a standard ANN can be seen as a probabilistic classifier where the estimated outputs are class probabilities. This poses problems for engineering applications where a measure of uncertainty is essential for risk and reliability assessment, as well as rational decision-making. Thus, ML-based probabilistic models are of interest for application in real-world, complex structures.

A feature inherent to probabilistic models is that they provide important statistics, such as mean and variance. Therefore, a model built with feed-forward ANNs that estimates the parameters of an assumed probability distribution over a target variable can be viewed as one of this sort and thus consists a Probabilistic Neural Network (PNN). The mean-variance estimation (MVE) method, which was first proposed by Nix and Weigend [102], is one technique that employs PNNs for the construction of prediction intervals (PIs), where the uncertainty in target values is treated as a normally distributed error term. Therefore, for a given set of input vectors $\mathbf{x}$ and target scalars t containing noise, the prediction problem can be expressed as:

$$t = y + e = g(\mathbf{x}) + e \tag{2.38}$$

where e is a zero-mean random variable. Uncertainty in Equation 2.38 can be measured by the variance of t, and $y = g(\mathbf{x})$ is the mean of t.

Within the MVE framework, two separate ANNs, whose architectures need not be identical, are employed to estimate the mean and variance. This offers considerable flexibility with respect to the variance structure of the data, and allows for the model to capture local patterns in the data and efficiently approximate cases with non-stationary (heteroscedastic) variance. A schematic representation of this technique is depicted in Figure 2.14. As shown, the model inputs, i.e., an input vector or more simply a value x_i, are fed to the two ANNs used to estimate the prediction mean and variance, denoted as NN_y and NN_σ, respectively. As mentioned in the previous subsections, these apply a composition of non-linear functions that result in predictions of the mean and variance, denoted as $\hat{y}$ and $\hat{\sigma}^2$, respectively. Training the model amounts to simultaneously training the two networks using a common loss function, following the same general process as in Equation 2.36, but using a different expression for the loss. This is necessary since, in this case, the model produces outputs that correspond to the mean and variance of a normal distribution, which cannot be compared in a 1-to-1 fashion with the target data, since they contain no variance. Therefore, the loss function is described through an equivalent expression, i.e., using a likelihood function, and thus the problem of calibrating model parameters is solved within a Maximum Likelihood Estimation (MLE) framework.

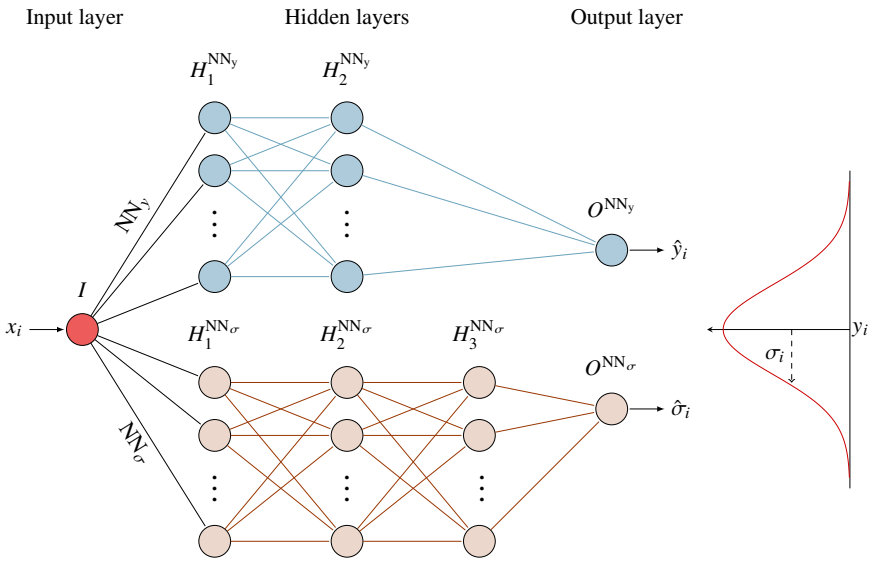

Figure 2.14: Schematic representation of the MVE method.

Considering that the error e in the predictions is Gaussian, the goal of the MLE may be formally written as:

$$w_y, w_\sigma = \underset{w_y, w_\sigma}{\operatorname{argmax}} \left\{ \prod_{i=1}^{n} \frac{1}{\sqrt{2\pi\hat{\sigma}_i^2}} \exp\left(-\frac{(t_i - \hat{y}_i)^2}{2\hat{\sigma}_i^2} \right) \right\} \tag{2.39}$$

where w_y, w_σ correspond to the parameters of NN_y and NN_σ respectively, t_i corresponds to a target value, $\hat{y}_i$, $\hat{\sigma}_i$ are the ANN predictions, and n is the number of samples. The different predictions can be considered to be statistically independent, and consequently the likelihood over the entire data-set can be obtained as the product of individual terms.

Ultimately, it is more computationally convenient to take the logarithm of the likelihood, which transforms the product to a sum and then multiplying this by -1, which makes this a minimization problem. The resultant loss function is known as the negative log-likelihood (NLL) and can be expressed as:

$$NLL = \sum_{i=1}^{n} -\log\left(\frac{1}{\sqrt{2\pi\hat{\sigma}_i^2}}\exp\left(-\frac{(t_i-\hat{y}_i)^2}{2\hat{\sigma}_i^2}\right)\right) \tag{2.40}$$

Using the quotient and power properties of logarithms and ignoring the constant terms of Equation 2.40, yields:

$$NLL = \frac{1}{2}\sum_{i=1}^{n}\left(\ln\hat{\sigma}_i^2 + \frac{(t_i-\hat{y}_i)^2}{\hat{\sigma}_i^2}\right) \tag{2.41}$$

and eventually the optimization problem can be stated as:

$$w_y, w_\sigma = \underset{w_y, w_\sigma}{\operatorname{argmin}}\, NLL \tag{2.42}$$

Similar to conventional ANNs, described in the previous subsection, this optimization problem can be solved using the back-propagation algorithm with the aid of automatic differentiation until the loss function has been sufficiently minimized. The constructed PIs with a $(1-\alpha)\%$ confidence level computed by the trained model are,

$$\text{PIs} = \left[\hat{y} - z_{1-\frac{\alpha}{2}}\sqrt{\hat{\sigma}^2},\ \hat{y} + z_{1-\frac{\alpha}{2}}\sqrt{\hat{\sigma}^2}\right] \tag{2.43}$$

Two indexes that are commonly used for evaluating the performance of PIs are the prediction interval coverage probability (PICP) and the prediction interval normalized average width (PINAW). PICP is the fraction of targets that lie within the lower and upper bounds of intervals, and a large PICP value indicates that a high amount of testing data have fallen within the PIs. The use of the PINAW metric serves the purpose of assessing the sharpness of PIs. In practice, for useful and reliable PIs, the value of PICP should not be less than the confidence level of PIs, and their width, as measured by the PINAW index, should be as small as possible, given that narrower PIs are theoretically more useful. These indexes are calculated in accordance with the definitions provided by Khosravi et al. [103]. Namely, PICP is defined as:

$$\text{PICP} = \frac{1}{n}\sum_{i=1}^{n} c_i \tag{2.44}$$

where, $c_i = 1$ if $t_i \in [L_i, U_i]$, otherwise $c_i = 0$; L_i and U_i are the lower and upper bounds of the ith PI respectively. PINAW is defined as follows:

$$\text{PINAW} = \sum_{i=1}^{n} \frac{U_i - L_i}{nR} \tag{2.45}$$

where R is the difference between the maximum and minimum target values in the test data-set, used to normalize the PI average width into a percentage value.

The method described here can capture aleatoric uncertainty but not epistemic uncertainty. In the context of ANNs, epistemic uncertainty is typically interpreted as uncertainty regarding the model parameters, i.e., the network's weights. This is a special case of what is referred to as approximation uncertainty. To quantify this kind of uncertainty, Bayesian neural networks have been proposed as a Bayesian extension of ANNs [104, 105]. In Bayesian networks, each real number representing a weight is replaced by a probability distribution (again, typically a Gaussian), and learning amounts to Bayesian inference. However, this is out of the scope of this study and was only mentioned for the sake of completeness.

Chapter 3

Problem definition

This section unfolds the particulars of the problem under consideration. The first part presents the general problem this work was concerned with. This is followed by the presentation of the employed case study, including all geometry-related considerations as well as the quantification of the input source variability taken into account. Finally, the development of the physics-based model of the structure used to generate synthetic strain data is introduced.

3.1 Problem description

As already presented in the introduction chapter of this thesis, this work revolves around the design of a localized SHM system on a large-volume structure, one that remains robust against various uncertainties in its damage detection performance, all while using a minimal strain sensing scheme. This concept is especially intriguing for the life-cycle monitoring of integral structural components with confined spaces, such as the double bottom compartment of a modern commercial ship, where conventional visual and/or NDT inspection is hindered. In practice, the successful in-service implementation of such a system revolves around three main aspects.

The first step consists of making informed decisions on the potential regions where damage might occur, with the goal of increasing the likelihood that the local diagnostic system will provide substantial health monitoring value for the entire structure. For this purpose, empirical findings from past inspections and accident investigations can be leveraged as viable information. These can be used to guide the choice of the number and location of sensors that comprise the SHM system. The second aspect pertains to the premise that damage identification requires a comparison between two system states [30]. Therefore, the employed damage-sensitive features must be such as to effectively reflect the transition of the structural system from one state to another, i.e., from the healthy to the damaged state. In the proposed framework, the disturbance in the strain field caused by the existence of excessive deflections in the plate elements of the stiffened panel is expected to serve this purpose. However, obtaining a prediction on the magnitude of the damage given some strain response data is not sufficient on its own for damage identification. A criterion must be defined to determine whether a plate deflection corresponds to the intact or the damaged condition. In this work, this criterion is encapsulated in the maximum allowable threshold value of 8 mm following the requirements of IACS [106]. Finally, a crucial aspect is the ability of the system to systematically incorporate potential sources of uncertainty, both in the inputs and the predictions, which in the case presented herein is achieved through the use of methods that rely on a probabilistic foundation.

Taking now a bird's-eye view of the problem, it can be stated that an SHM system like the one conceptually defined above, is intended to inform inspection whenever the underlying

conditions require doing so, thereby facilitating a CBM approach as opposed to the current time-based one. This can be neatly captured by a framework based on the concept of an alarm strain threshold indicator introduced in the last chapter.

3.2 Case study description

3.2.1 Reference system configuration

The subject geometry considered in this study is an idealized version of the double bottom assembly in the midship part of MOL Comfort, with the vessel's class-specific bottom plans serving as the basis [107]. The problem is simplified by focusing on a specific geometric domain, namely the double bottom module shown in Figure 3.1c, rather than the entire ship structure shown in Figure 3.1a and 3.1b. This reduction to the problem was possible because it was assumed that the damage of interest occurs only in particular unsupported platings located at the external bottom of Cargo Hold No. 6. Without any loss of generality, following the insights retrieved from a survey on one of MOL Comfort's sister vessels, it was decided to take the region denoted by the hatched rectangle as the suspect area for strain sensor placement. Essentially, the highlighted region in question encompasses the damage-critical zone and any nearby platings that could potentially be affected by the produced damage. We can thus safely infer that the section of the bottom (hereinafter referred to as "stiffened panel" for the sake of internal consistency) bounded lengthwise by the two watertight bulkheads of the hold and, breadthwise, by the centreline and outboard girders, is sufficient enough to allow for the stress/strain redistribution after damage.

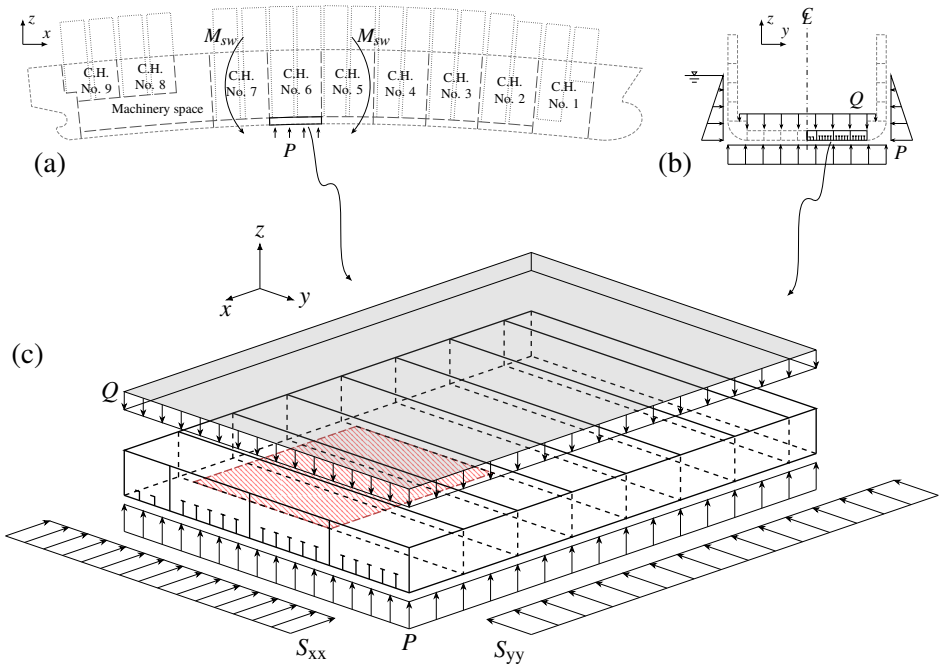

Figure 3.1: (a) Reference vessel side view, (b) section cut amidships, and (c) 3D view of the isolated stiffened panel geometry along with the exerted loading regime. Hatched area denotes the monitoring region.

A detailed top view of the external bottom which contains the monitoring region is shown in Figure 3.2a with the x axis taken parallel to the ship's centreline and the y axis normal to it. The idealized panel, framed both longitudinally and transversely, is a grillage-type structure with dimensions 27 m $\times$ 18 m $\times$ 2.2 m ($L \times B \times h_{\mathrm{DB}}$). The typical span between adjacent transverse floors is denoted by a equal to 3600 mm. Longitudinal stiffeners are non-uniformly distributed breadthwise, with spacing values varied at $b_1 = 898$ mm, $b_2 = 851$ mm, and $b_2 = 850$ mm, while there are five girders in number extending between the watertight bulkhead ends. In addition, Table 3.1 presents the scantlings of the structural members that comprise the transverse cross-section of the stiffened panel.

Table 3.1: Structural scantlings (plate, stiffeners, and primary supporting members).

Type	Geometry	Dimensions (mm)
1	Angle	$250 \times 90 \times 11/16$
2	T	$400 \times 11 + 150 \times 18$
Plate	External bottom	20
	Inner bottom	15
	Girder	14
	Floor	11

Additionally, the monitoring region with potential sensor locations is illustrated using the green and red ellipses that indicate the plate elements where initial deflections are considered possible to occur. A distinction is made between those deflections that will grow beyond the acceptable threshold (red ellipses) and those that will remain within nominal limits (green ones). On a side note, the maximum potential out-of-plane deflection was taken as 20 mm in the design, which is comparable to the deflection levels found during the investigations after the MOL Comfort accident. To model the welding-related bathtub shape of the deflection (Δz) at any location (u, v) on a plate element located between stiffeners, a sinusoidal expression was employed. This expression is defined as follows:

$$\Delta z(u, v; W_{\mathrm{o}}) = W_{\mathrm{o}} \sin\left(\frac{\pi u}{a}\right) \sin\left(\frac{\pi v}{b}\right) \tag{3.1}$$

where W_{o} denotes the amplitude of the deflection, $u \in [0, a]$ and $v \in [0, b]$. It is of note also that since, in practice, welding techniques lead to inward deformation for most panels, it was assumed that the condition of the initial deflections of the platings was of the symmetric sinusoidal one.

An indicative schematic of the potential sensor locations within the monitoring region is illustrated in Figure 3.2b. As indicated, these register the strain values at the center of each plate element, which was considered as the optimal location given the geometry of the target damage. In total, the number of available sensor locations is $N_s = 30$, while each sensor can monitor $N_c = 3$ strain components, namely normal strain along the x and y axes, denoted as

ε_{xx} and ε_{yy} respectively, and the in-plane shear strain component ε_{xy}. Note that the naming conventions follow those shown in Figure 3.2.

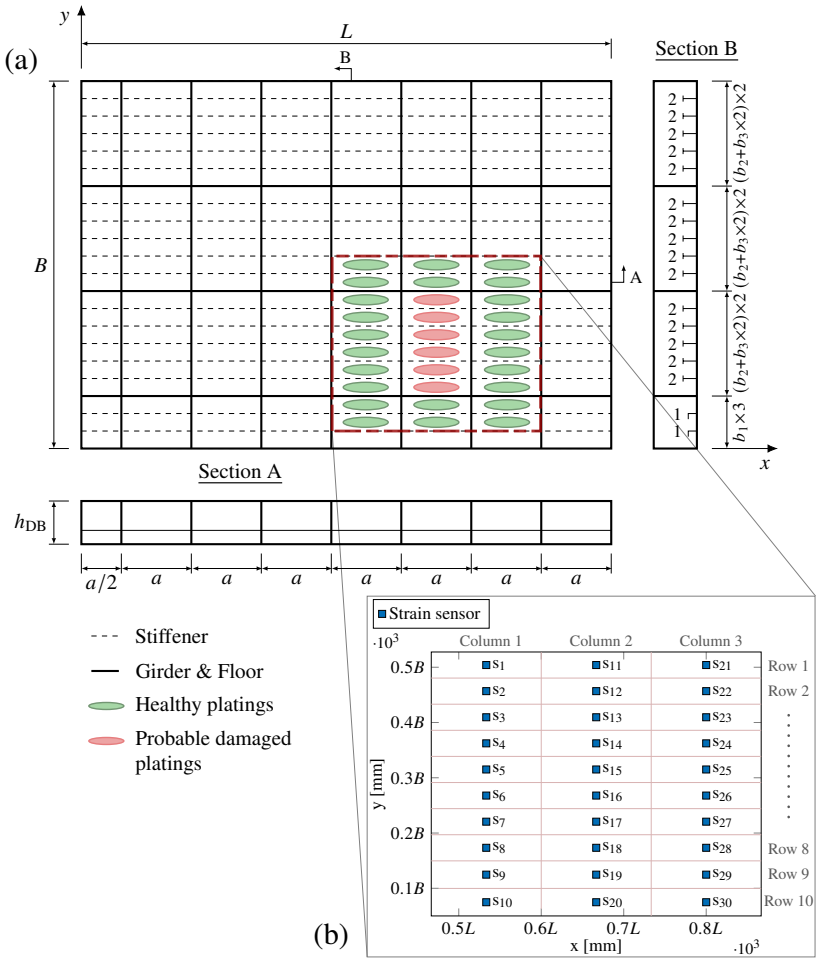

Figure 3.2: (a) Structural geometry and (b) deployed sensor topology. Green ellipses indicate the healthy platings, i.e., $W_o \in [0, 8]$ mm, while the red ones indicate the probable damaged platings, i.e., $W_o \in [8, 20]$ mm.

3.2.2 Input source variability definition

To effectively describe the input source variability, the basic random variables must be stated and associated with their respective PDFs. In terms of operational variability, the basic random variables correspond to the loads acting on the double-bottom structure. In this work, the loading scenario selected for the reference vessel and, by extension, the stiffened panel geometry, corresponds to still-water (steady-state) conditions. While this may appear restrictive in a realistic field scenario, the relatively slow temporal evolution of out-of-plane deflections allows for monitoring strategies with a less frequent sampling ratio (i.e. when the ship is in harbor or sailing in calm weather) without sacrificing on the quality of system predictions.

In this context, the loads acting at the panel level (see Figure 3.1c) are the hull girder bending stresses (S_{xx}) which are compressive since hogging is dominant in containerships [1], the

transverse in-plane compressive stresses (S_{yy}) due to side sea pressure, the direct lateral action of bottom sea pressure (P) on the hull exterior and the cargo weight (Q) per unit length on the inner bottom. To avoid confusion with σ, which represents standard deviation, it should be highlighted that S in this work relates to stress. Each of these load terms was assumed to follow a normal marginal distribution, namely: $S_{xx} \sim \mathcal{N}\left(s_{xx}; \mu_{S_{xx}}, \sigma^2_{S_{xx}}\right)$, $S_{yy} \sim \mathcal{N}\left(s_{yy}; \mu_{S_{yy}}, \sigma^2_{S_{yy}}\right)$, $P \sim \mathcal{N}\left(p; \mu_P, \sigma^2_P\right)$, and $Q \sim \mathcal{N}\left(q; \mu_Q, \sigma^2_Q\right)$.

All of the aforementioned parameters depend on the vessel's loading condition. Typically, loading conditions are discrete and strictly determined based on a vessel's expected operation. In order to reflect the whole operational profile of the vessel in terms of still-water loading, it was decided that the distributions would be defined independently for each loading scenario. Thus, their means were assumed to be equal to their respective nominal values, as determined by the loading manual of the vessel under each condition. The variance was computed using estimated coefficients of variation (CoVs) that can be obtained from the literature for each parameter. Ultimately, a total of 72 loading conditions were considered with mean ranges $\mu_{S_{xx}} \in [42.9, 135.5]$ MPa, $\mu_{S_{yy}} \in [15.1, 26.7]$ MPa, $\mu_P \in [0.11, 0.15]$ MPa and $\mu_Q \in [59.5, 151.4]$ kN/m. The reader can refer to Appendix A to obtain a more detailed insight into the population means corresponding to each loading condition. Their respective CoVs were taken as 3.33% [5] for S_{xx}, 1% for S_{yy} and P, which was assumed based on the low variability of these parameters due to their dependence on vessel trim, and finally 25% for Q taken indicatively following [108]. Ultimately, the load-related variability can be described concisely using a random vector $\mathbf{L} \in D_{\mathbf{L}} \subset \mathbb{R}^4$, which is arranged as $\mathbf{L} = [\, S_{xx},\ S_{yy},\ P,\ Q\,]^T$ and has a joint PDF given by:

$$f_{\mathbf{L}}(\mathbf{L} = \mathbf{l}; \boldsymbol{\mu}_{\mathbf{L}}, \boldsymbol{\Sigma}_{\mathbf{L}}) = \frac{1}{(2\pi)^{4/2} \left|\boldsymbol{\Sigma}_{\mathbf{L}}\right|^{1/2}} \exp\left(-\frac{1}{2}\left(\mathbf{l} - \boldsymbol{\mu}_{\mathbf{L}}\right)^T \boldsymbol{\Sigma}_{\mathbf{L}}^{-1}\left(\mathbf{l} - \boldsymbol{\mu}_{\mathbf{L}}\right)\right) \tag{3.2}$$

where $\boldsymbol{\mu}_{\mathbf{L}} \in D_{\boldsymbol{\mu}_{\mathbf{L}}} \subset \mathbb{R}^4$ and $\boldsymbol{\Sigma}_{\mathbf{L}} \in D_{\boldsymbol{\Sigma}_{\mathbf{L}}} \subset \mathbb{R}^{4\times4}$ are the mean vector and positive semi-definite covariance matrix of vector variable $\mathbf{L}$ respectively:

$$\boldsymbol{\mu}_{\mathbf{L}} = [\, \mu_{S_{xx}},\ \mu_{S_{yy}},\ \mu_P,\ \mu_Q\,]^T \tag{3.3}$$

$$\boldsymbol{\Sigma}_{\mathbf{L}} = \mathrm{diag}\left(\begin{bmatrix} \sigma_{S_{xx}} \\ \sigma_{S_{yy}} \\ \sigma_P \\ \sigma_Q \end{bmatrix}\right) \cdot \begin{bmatrix} 1 & c_{12} & c_{13} & c_{14} \\ c_{12} & 1 & c_{23} & c_{24} \\ c_{13} & c_{23} & 1 & c_{34} \\ c_{14} & c_{24} & c_{34} & 1 \end{bmatrix} \cdot \mathrm{diag}\left(\begin{bmatrix} \sigma_{S_{xx}} \\ \sigma_{S_{yy}} \\ \sigma_P \\ \sigma_Q \end{bmatrix}\right) \tag{3.4}$$

with $\mathrm{diag}(\cdot)$ denoting the diagonal matrix. Given that the various parameters exhibit physical correlation, this has been accounted for through the inclusion of correlation terms in the non-diagonal entries of the matrix. Their values were chosen based on physics-related considerations and were set to $c_{12} = 0.2$, $c_{13} = 0.2$, $c_{14} = 0.5$, $c_{23} = 0.9$, $c_{24} =$

0.2, $c_{34} = 0.2$. In general, however, since these are assumed for illustrative purposes, they can be conveniently replaced in practice if further information is available.

Apart from the load-related parameters, the input source variability also contains the out-of-plane deflection amplitude W_o, which according to Teixeira et al. [109] can be described using a lognormal distribution, i.e., $W_o \sim \ln \mathcal{N}\left(w_o; \mu_{W_o}, \sigma^2_{W_o}\right)$. For the sake of comprehension, its functional form is provided by Equation 3.5. Given the mean value m_{W_o} and variance v_{W_o}, the lognormal distribution population parameters μ_{W_o} and σ_{W_o} can be calculated through the method of moments as described by Equation 3.6. As a result, the parameters of the PDF representing W_o are $\mu_{W_o} = 0.511$ mm and $\sigma_{W_o} = 1.114$ mm. Finally, a visual representation of the underlying statistical structure of W_o is presented in Figure 3.3. Based on the distribution, it appears that W_o is less than 8 mm in 92% of the observations, and is greater than 8 mm in 8% of the observations.

$$f_{W_o}(W_o = w_o; \mu_{W_o}, \sigma_{W_o}) = \begin{cases} \dfrac{1}{\sqrt{2\pi}\sigma_{W_o} w_o} \exp\left(-\dfrac{1}{2}\left(\dfrac{\ln w_o - \mu_{W_o}}{\sigma_{W_o}}\right)^2\right) & \text{if } w_o > 0 \\ 0 & \text{elsewhere} \end{cases} \tag{3.5}$$

$$\mu_{W_o} = \ln\left(\frac{m^2_{W_o}}{\sqrt{v_{W_o} + m^2_{W_o}}}\right), \quad \sigma_{W_o} = \sqrt{\ln\left(\frac{v_{W_o}}{m^2_{W_o}} + 1\right)} \tag{3.6}$$

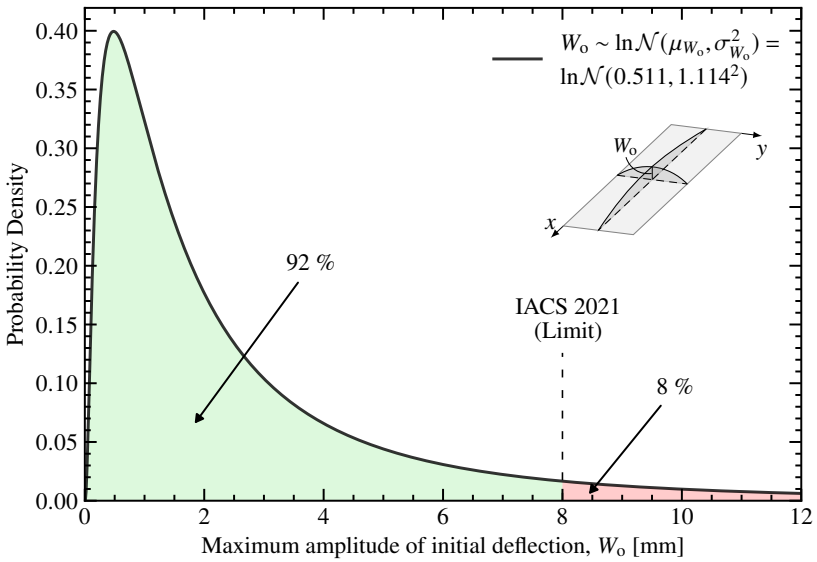

Figure 3.3: Statistical structure of maximum magnitude of initial deflection W_o.

3.3 Finite Element Modeling

In response to the increased complexity of the problem at hand, an FE model of the stiffened panel geometry was generated. The FE model was ultimately intended to serve as a synthetic data generator whereby a computationally cheap surrogate model can be further trained to alleviate its burdensome computational demands. For this purpose, the ANSYS Mechanical commercial software by means of its integrated scripting language (APDL[1]) has been employed. This allowed the model to be parameterized in terms of the input source variability parameters to enable an MCS-based iterative solution scheme. An indicative view of the FE model of the analyzed system may be seen in Figure 3.4. The problem has been cast in a linear static setting with the material being regarded as linear elastic and isotropic, as it was expected that the applied loads would not result in plastic deformation. In this context, a Young's modulus of 207 GPa and a Poisson's ratio of 0.3 were used as representative values of shipbuilding steels.

To streamline the modeling process, a grid of effective girders and floors was used to emulate the stiffness contributed to the overall system by the inner bottom shell. These were represented by 2-node linear beam elements with cross sectional properties equivalent to the original topology. The same element type was registered for the stiffeners of the panel. The external bottom was discetized using 4-node quadrilateral shell elements with a nominal global mesh size of 900 mm. Selective mesh refinement was adopted to maintain a feasible analysis without sacrificing accuracy, with the finest element size (~100 mm) used in the region concerned with initial deflections (monitoring area). This was gradually succeeded through transition layers of moderately distorted elements arranged in a way that mesh compatibility was never compromised, as seen in Figure 3.4a. The obtained mesh resolution of a total content of N_e = 9422 shell elements ensured an almost unity aspect ratio of element size for the subject area and was able to capture the intended deflection amplitudes of the steel platings.

Regarding the loads, the in-plane stresses (S_{xx}, S_{yy}) were applied using their equivalent concentrated loads (N_x, N_y) by first coupling the fore and outboard edges of the panel with a reference node, as seen in Figure 3.4a. Essentially, coupling is a way to force a set of nodes to have the same DOF value; this way, each side remained straight and normal to the corresponding in-plane load throughout the whole loading procedure. Water pressure P and container weight Q were applied as a surface load distributed over the outer bottom and as a grid of line loads appropriately distributed on the effective beam elements, respectively.

As far as boundary conditions are concerned, symmetry conditions were applied along the free edge of the panel coinciding with the centreline of the ship. All nodal displacements at the remaining model edges were constrained in the vertical direction with zero displacement conditions. Moreover, free rotation around their respective axis was constrained using the same condition, as both the transverse and the side longitudinal bulkheads are usually much stiffer

[1]ANSYS Parametric Design Language

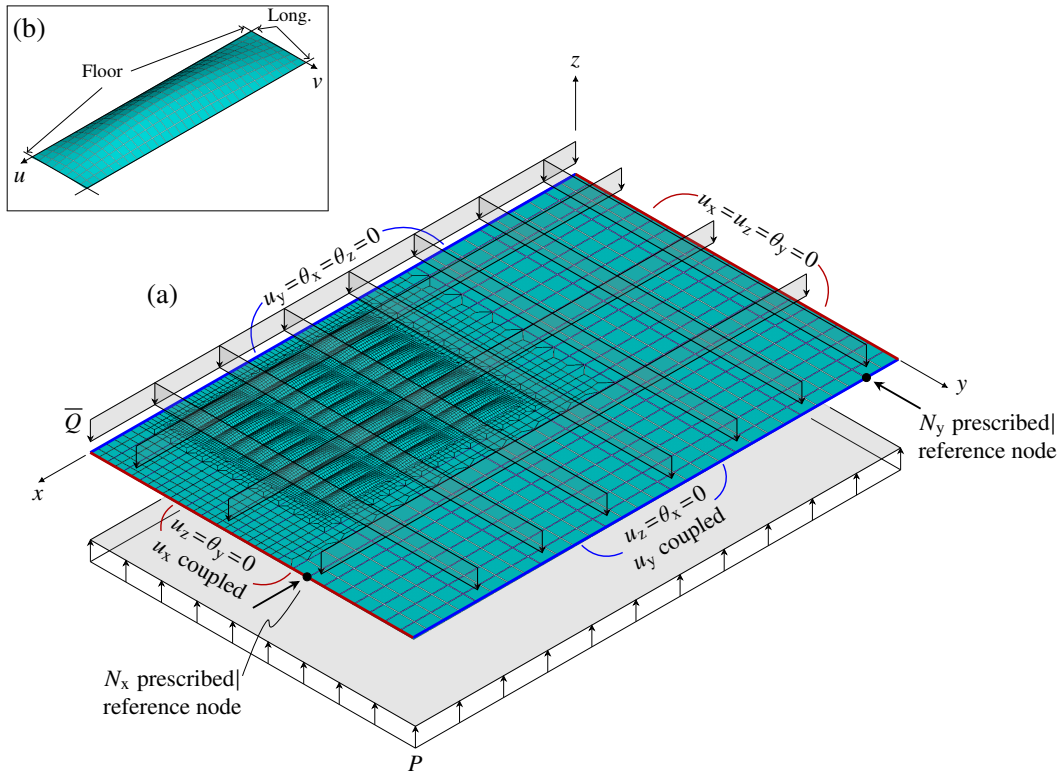

Figure 3.4: (a) FE mesh resolution of the modeled geometry with imposed boundary control and applied loads, and (b) inset display of an indicative initial deflection (with magnification factor of 10).

than the remaining double bottom configuration. Finally, in order to avoid rigid body motions in the longitudinal direction, the displacement of the aft end section nodes was constrained in that direction imposing zero displacement. The imposed boundary conditions of the model are visually summarized in Figure 3.4a. Where u_x, u_y, and u_z denote the translations along x, y and z axes. Similar, θ_x, θ_y and θ_z denote the rotations around x, y and z axes.

For the damage, the deflection of the element nodes within each local plating was defined by changing their vertical position following Equation 3.1, considering a local coordinate system with the axes set as shown in Figure 3.4b.

In addition, before employing the developed FE model to obtain synthetic strain response data, it was considered essential to conduct a qualitative exploration to test the validity of the adopted modeling approach. Due to the complexity of the system of interest, it was not possible to obtain a solution to the problem by straightforward analytical techniques to act as a reference for comparative tests. Besides that, neither experimental data nor studies on existing similar structures have been found in the broader literature. Therefore, in the absence of these means, it was decided to rely on the expectations and the engineering judgment of the writer.

Due to the complex interplay between the combined loads applied to the FE model, it was decided that splitting the applied loads into individual components would be a good modeling practice for this non-formal validation process. This was implemented so as to better

understand the effect induced by each load type individually. Each one was thereafter evaluated independently for each set of strength attachments supporting the exterior bottom. This indicates that triplets of baseline FE analyses were carried out for each individual external load, corresponding to a stiffener-, girder-, and floor-only case. The deformed shape of the structure was eventually displayed for each of these sub-cases computed by the solver, demonstrating that it agrees well with the intuitive approximation of its corresponding counterpart. The analysis was brought to a conclusion by assessing the FE model in a similar manner with all of its members assembled. Overall, the collected findings revealed sufficient validity for the model to be deployed as a credible generator of synthetic data.

On a closing note, it should be pointed that the elapsed time per simulation was on average 45 sec using an Intel® Core™ i5-5200U CPU with 6 GB RAM (parallel ANSYS® processing over 2 threads). Considering that the forward uncertainty propagation of the input source variability to the strain response data is associated with a significant number of model evaluations within an MCS, it can be determined that, to generate training data for the damage identification models at reasonable offline cost, a surrogate would be required.

Chapter 4

Feature selection and surrogate modeling

Having developed the high-fidelity model, a two-step exploratory study is described, which was undertaken to analyze the damage-sensitive information specific to each strain component and eventually arrive at the most insightful one to be used in the damage identification process. The section is concluded with a description of the surrogate model used to automate the prediction of the selected damage-sensitive features.

4.1 Exploratory analysis for feature selection

Identifying damage-sensitive features from the collected system response data is crucial for the design of reliable SHM architectures. However, not all quantities provide high damage detection performance, nor do they necessarily connect in any meaningful way to damage presence, not even under a most powerful ML algorithm manipulation. The physics-based FE model described in the previous section was used to assess the discriminating power of each component of the strain tensor recovered from the jth strain sensor $\boldsymbol{\varepsilon}_s^{(j)} = \left[\varepsilon_{\mathrm{xx}}^{(j)},\ \varepsilon_{\mathrm{yy}}^{(j)},\ \varepsilon_{\mathrm{xy}}^{(j)}\right]^T$, $j = 1, \ldots, N_s$.

As a preliminary step towards feature selection, an exploratory study was undertaken on a deterministic level exclusively within the numerical environment. As we are interested in the strain field perturbation induced by the existence of damage, studying the strain field difference between the healthy and damaged states can provide significant insight. This can be determined by subtracting the strain results extracted from the integration points of each shell element e referring to a damaged case scenario, from the respective quantities corresponding to a healthy case scenario. In mathematical terms, this is interpreted as the formulation of a column vector $\boldsymbol{\varepsilon}_i^{\mathrm{Diff}} = \left\{\varepsilon_{i,e}^{\mathrm{D}} - \varepsilon_{i,e}^{\mathrm{H}}\right\}_{e=1}^{N_e}$ where "i" denotes the different strain components (i.e., xx, yy or xy), superscript "H" stands for healthy, and "D" for damaged. Each vector related to a strain component is in turn collected to a matrix $\mathbf{E}^{\mathrm{Diff}} = \left[\boldsymbol{\varepsilon}_{\mathrm{xx}}^{\mathrm{Diff}},\ \boldsymbol{\varepsilon}_{\mathrm{yy}}^{\mathrm{Diff}},\ \boldsymbol{\varepsilon}_{\mathrm{xy}}^{\mathrm{Diff}}\right] \in \mathbb{R}^{N_e \times N_c}$.

For the healthy state a single realization of N_s independent and identically distributed (i.i.d.) random variables $\left\{w_{\mathrm{o}}^{(j)}\right\}_{j=1}^{N_s}$ was drawn from the PDF of W_{o}. To ensure that the reference healthy state scenario complied with the regulations offered by IACS, an upper cutoff limit of 8 mm (truncation in the PDF) was set for W_{o}. For the damaged case, initial deflections of 20 mm were considered in the damage-critical zone, while the rest of the adjacent platings were kept at their previous values. A representative load case was selected for demonstration purposes. As seen in Figure 4.1 which plots the strain difference in the vicinity of the damage-critical zone, $\varepsilon_{\mathrm{yy}}$ was the feature that directly correlates to damage presence. This is consistent with the problem physics, since according to plate theory the strains in the short dimension are the ones that are dominant in plate bending. Based on the results of this

deterministic analysis, it was determined that the ε_{xy} component should be discarded, as it reaches its maximum magnitude values in the corners of each plate element, which does not follow along with the deployed sensor topology.

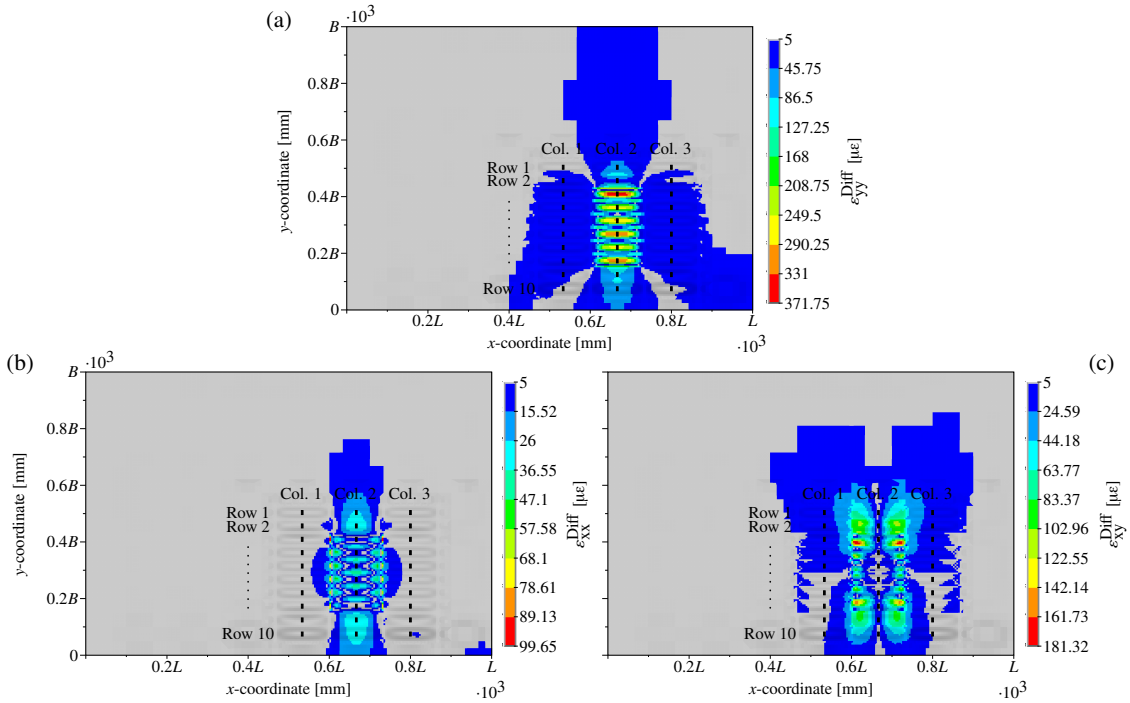

Figure 4.1: Strain differences (a) $\boldsymbol{\varepsilon}^{\text{Diff}}_{\text{yy}}$, (b) $\boldsymbol{\varepsilon}^{\text{Diff}}_{\text{xx}}$, and (c) $\boldsymbol{\varepsilon}^{\text{Diff}}_{\text{xy}}$ of the healthy and damaged structure for indicative load and deflection realizations. The gray elements indicate the area where there is zero strain difference or the strain difference is buried beneath the system's noise level (5 με).

The next analysis was aimed at comparing the damage-sensitivity of the two remaining candidate features, ε_{xx} and ε_{yy}, in statistical terms. For the healthy state, a number of $N_{MC} = 500$ samples of initial deflection vectors $\left\{\left[w^{(1)}_{\text{o},i}, \ldots, w^{(j)}_{\text{o},i}, \ldots, w^{(N_s)}_{\text{o},i}\right]\right\}_{i=1}^{N_{MC}} \in \mathbb{R}^{N_{MC}\times N_s}$, were drawn from the PDF of W_{o} within the context of an MCS supported by the LHS method. For the damaged case, the maximum deflection of 20 mm was applied again to specific plate elements, those containing sensors numbered from $j = 13, \ldots, 18$ according to the notation of Figure 3.2b, while for the rest, the same values as in the healthy case were retained. This was done to examine whether damage in its most severe form propagates to the nearby platings. The mean difference between a feature observed at the healthy state and the corresponding one observed at the damaged state is presented in Figure 4.2. In Figure 4.3, indicative histograms of these features from sensors $j = 8, 18$ are plotted to illustrate their statistical structure. As indicated, the sensors most sensitive to the strain field disturbance were the ones located in the damage-critical zone (thus, $j = 13, \ldots, 18$), while the highest sensitivity of ε_{yy} was again evident. Furthermore, a statistical conclusion that may be extracted is that the strain response in the damage-critical zone was statistically independent of the initial deflections far from its immediate vicinity. Ultimately, the damage-sensitive features that will guide

the damage identification strategy can be arranged in the (damage-sensitive) feature vector $\boldsymbol{\varepsilon} = \left[\varepsilon_{yy}^{(13)},\ \varepsilon_{yy}^{(14)},\ \varepsilon_{yy}^{(15)},\ \varepsilon_{yy}^{(16)},\ \varepsilon_{yy}^{(17)},\ \varepsilon_{yy}^{(18)}\right]^T \in D_{\boldsymbol{\varepsilon}} \subset \mathbb{R}^{d_{\boldsymbol{\varepsilon}}}$ with $d_{\boldsymbol{\varepsilon}} \in \mathbb{Z}^+$.

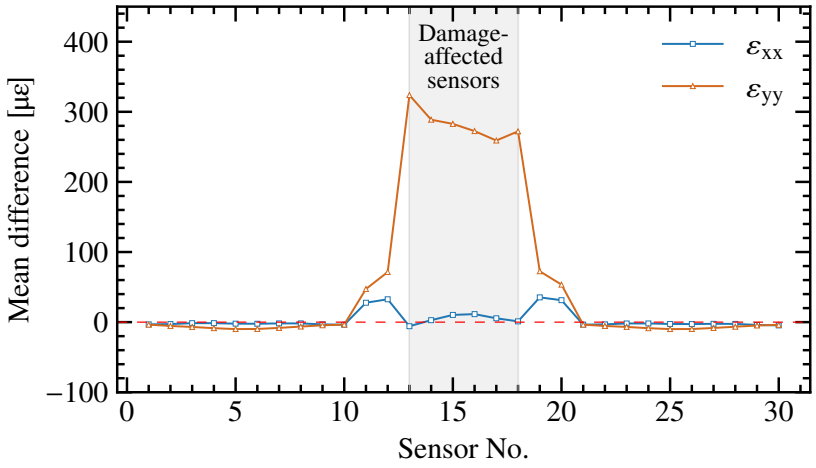

Figure 4.2: Mean difference of ε_{xx} and ε_{yy} over the potential sensor locations.

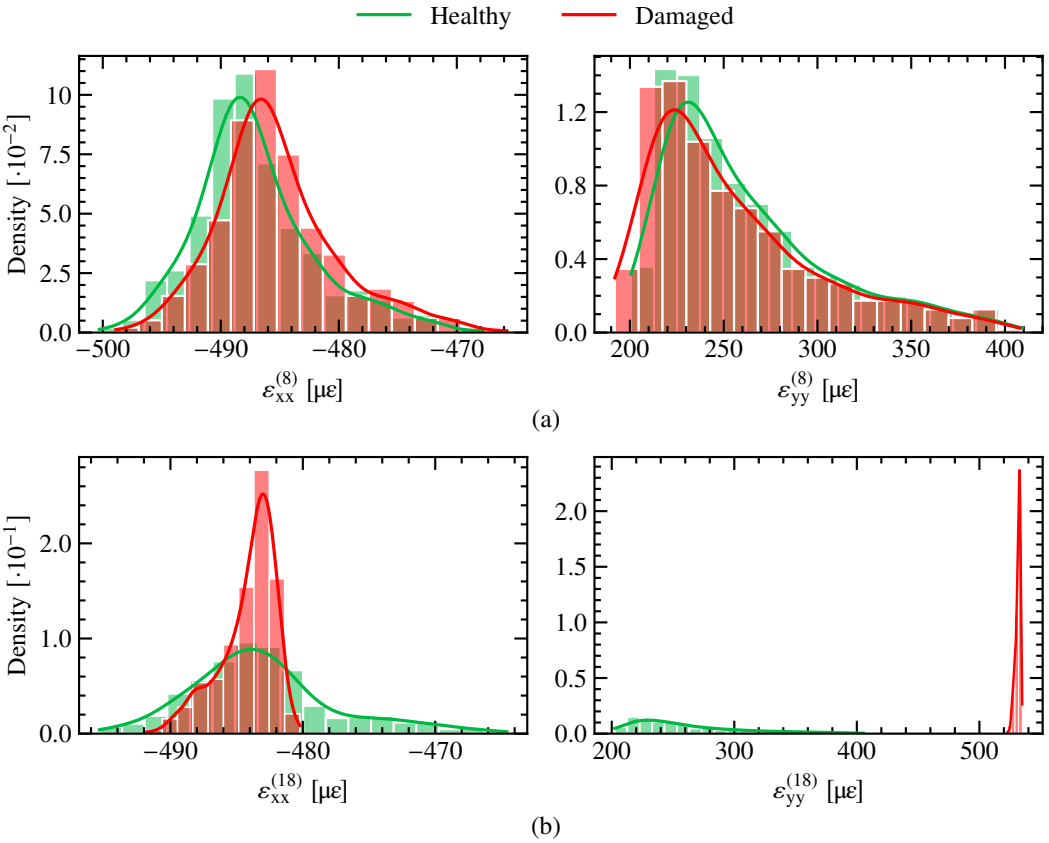

Figure 4.3: Statistical structure of the strain readings at sensors (a) ID 8 and (b) ID 18.

4.2 ANN-based surrogate modeling for strain estimates

To quantify the uncertainty in the present damage detection framework, a large amount of analyses is required. Specifically, the number of MCS samples in order to obtain estimates for the mean and standard deviation of ε_{yy} with an acceptable error of around 1% and a level of significance of 5% was estimated to be $\sim 10^4$. This was approximated using a representative value of the standard deviation of the sample obtained from the previous statistical exploration while following a well-established process [76] based on sampling distributions and the central limit theorem. The large number of required simulations highlights the need for the construction of a surrogate model $\mathcal{F}$. As such, an ANN model was employed and ultimately used in place of the original numerical model $\mathcal{M}$ created in the previous chapter. A visualization of the adopted ANN-based surrogate modeling process is provided in Figure 4.4.

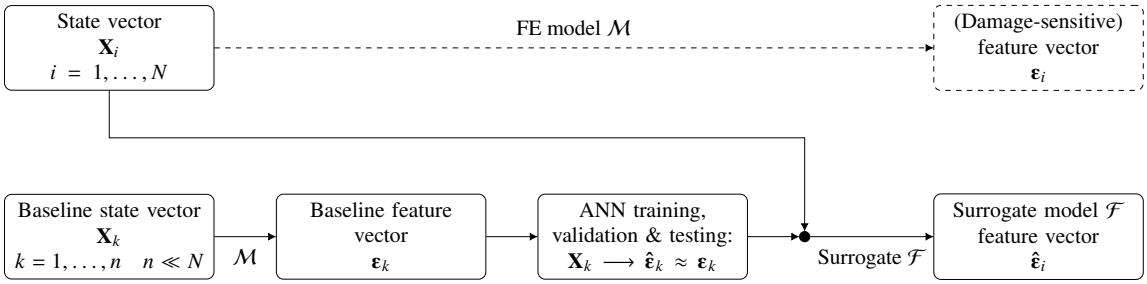

Figure 4.4: ANN-based surrogate modeling strategy.

The numerical model was exploited to create a baseline set $\boldsymbol{D}^{\text{base}}$ of synthetic data that would be used for training, validation and testing purposes, which was necessary for the construction of the surrogate model. Therefore, $n = 2000$ observations were uniformly sampled from the support set of all 34 input source variability parameters in order to encompass all potential solution trends. The resulting base set was formulated as $\boldsymbol{D}^{\text{base}} = \{\mathbf{x}_k; \boldsymbol{\varepsilon}_k\}_{k=1}^{n}$, where $\mathbf{x}_k = \left[s_{\text{xx},k},\ s_{\text{yy},k},\ p_k,\ q_k,\ w_{\text{o},k}^{(1)}, \ldots, w_{\text{o},k}^{(j)}, \ldots, w_{\text{o},k}^{(30)}\right]^T$ is the kth instance of the input state vector, and $\boldsymbol{\varepsilon}_k = \left[\varepsilon_{\text{yy},k}^{(13)}, \ldots, \varepsilon_{\text{yy},k}^{(j)}, \ldots, \varepsilon_{\text{yy},k}^{(18)}\right]^T$ is the corresponding output feature vector. The lower and upper bounds for each random variable were set according to their corresponding ranges.

From the total number of samples in $\boldsymbol{D}^{\text{base}}$, 80% were assigned for training and 20% for testing purposes. The training $\boldsymbol{D}^{\text{train}}$ and testing $\boldsymbol{D}^{\text{test}}$ data-sets were ensured to be mutually exclusive to avoid compromising the measure of generalization of the surrogate. To enhance network performance, the input data prior to training were standardized so that they have a zero mean and unit standard deviation, while the outputs (targets) were normalized so that they lie within the $[0, 1]$ range. Data normalization/standardization is a very common practice for regression tasks, where various continuous variables are usually measured at different scales. The employed neural network consisted of 4 hidden layers, with 32 neurons each, between the 34-dimensional input layer and the 6-dimensional output layer. ReLU activation

was used for all layers except the output one, where a sigmoid function was employed, aligned with the re-scaling scheme imposed to the output vectors. In terms of training, the Adaptive moment (Adam) optimizer based on mini-batch gradient descent was used with a learning rate of 0.005 and a batch size of 128. Training lasted 1500 epochs (i.e., 1500 iterations over all the training data) and the Mean Squared Error (MSE) was used as the loss function. A schematic representation of the ANN architecture design as applied for the task at hand can be found in Figure 4.5.

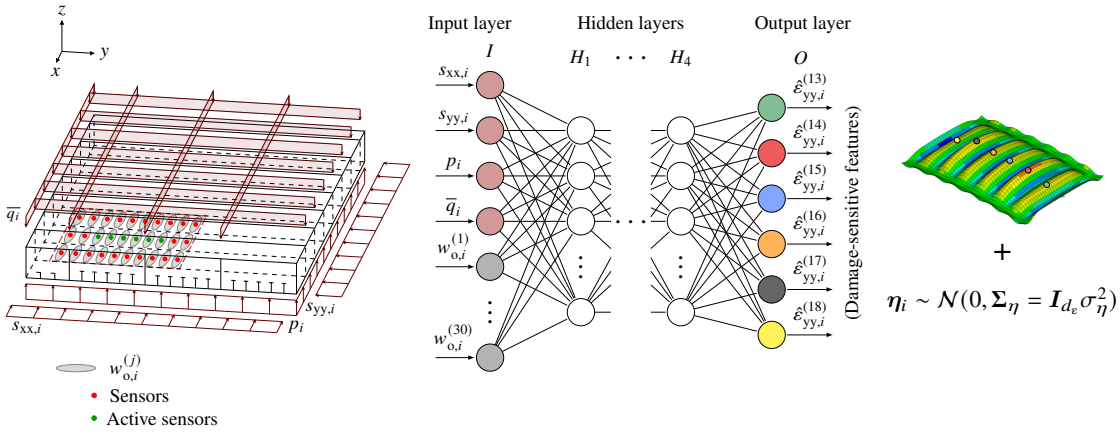

Figure 4.5: A schematic illustration of the ANN used as surrogate model for strain measurement prediction.

The ANN hyperparameters were tuned using heuristics based around a k-fold cross validation process of 10 folds and ultimately the network was trained over the entire data-set. During the 10-fold cross-validation procedure, the entire available data-set was split into 10 sets and the model was trained using the data from all sets except one (i.e., 9 of the 10 sets) while the remaining one was used for validation. This procedure was repeated for all 10 possible validation sets and the final validation score was obtained as the average of their respective scores. This method ensured good data splitting and better model generalization. Graphical representation of the validation and training Mean Absolute Error (MAE) curves derived from the average per-epoch MAE scores for all folds over all training epochs is provided in Figure 4.6a. To further assess the performance of the ANN model, the metric of coefficient of determination, known as R^2, was employed, which is widely used in DL-based applications [61, 84, 110]. In general, the larger the R^2 is, the higher the accuracy of the trained model is, and a value larger than 0.8 is believed to represent a high degree of accuracy. The value of R_j^2 between strain predictions and their corresponding targets, corresponding to

the jth strain component $\varepsilon_{yy}^{(j)}$, is defined as:

$$R_j^2 = 1 - \frac{\sum_{k=1}^{n^{\text{test}}} (\hat{\varepsilon}_{yy,k}^{(j)} - \varepsilon_{yy,k}^{(j)})^2}{\sum_{k=1}^{n^{\text{test}}} (\bar{\varepsilon}_{yy}^{(j)} - \varepsilon_{yy,k}^{(j)})^2}, \quad j = 13, \ldots, 18 \tag{4.1}$$

where n^{test} is the size of $\boldsymbol{D}_{\text{test}}$; $\varepsilon_{yy,k}^{(j)}$ is the kth strain observation; $\hat{\varepsilon}_{yy,k}^{(j)}$ is the jth component of the kth predicted output vector $\hat{\boldsymbol{\varepsilon}}_k = \mathcal{F}(\mathbf{x}_k)$; and $\bar{\varepsilon}_{yy}^{(j)}$ is the mean of the observed responses for all test samples. Then, the weighted (i.e., averaged) R^2 score over the outputs obtained from $\boldsymbol{D}_{\text{test}}$ is calculated as:

$$R^2 = \frac{\|\mathbf{R^2}\|}{d_{\boldsymbol{\varepsilon}}} \tag{4.2}$$

where $\mathbf{R^2} = \left\{R_j^2\right\}_{j=13}^{18} \in \mathbb{R}^{d_{\boldsymbol{\varepsilon}}}$, and $\|\cdot\|$ is the L^1-norm. The weighted R^2 score is presented in Figure 4.6b. From the latter two performance metrics, it can be ascertained that the model has been trained effectively with no over-fitting having occurred and that a sufficiently high performance has been achieved for the regression task ($R^2 = 0.994$).

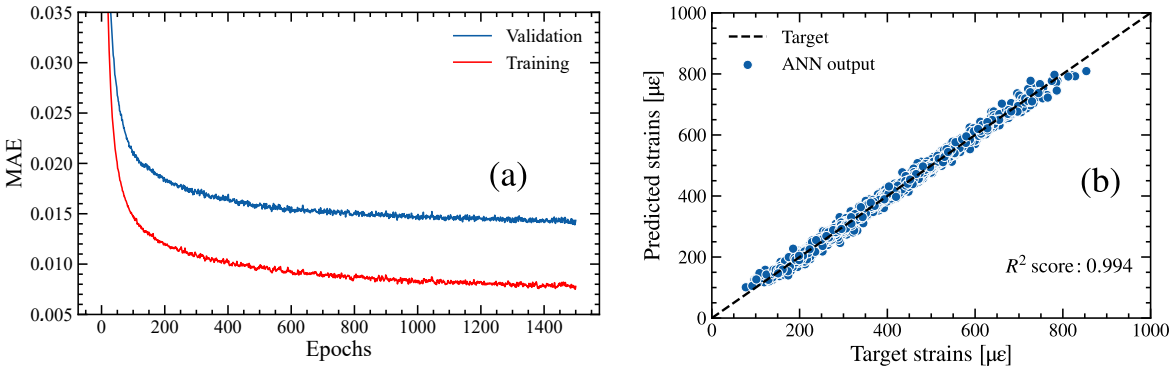

Figure 4.6: Evolution of ANN-based surrogate MAE over epochs (a) and indicative regression fit (b).

The statistical structure of the surrogate model error $\boldsymbol{\eta} = \boldsymbol{\varepsilon} - \hat{\boldsymbol{\varepsilon}}$ was further assessed using a pairplot presented in Figure 4.7. Histograms of the error term for individual strain components are what is contained in the diagonal entries, with scatter plots showcasing the joint distribution of different components being included in the upper triangular section and KDE-based joint distributions in the lower one. The error histograms are fitted with normal probability distributions and the results of the corresponding summary statistics are collected in Table 4.1 with units in microstrains. It is evident that the error structure is typical of what is known as prediction error, which showcases zero-mean behavior with standard deviation (~ 10 με) within the limits often found across relevant literature [62, 80]. Ultimately, it can be said the surrogate model error follows a zero-mean and uncorrelated multivariate Gaussian distribution

with variance $\sigma_{\boldsymbol{\eta}}^2 = 10\ \mu\varepsilon$, that is, $\boldsymbol{\eta} \sim \mathcal{N}(0, \boldsymbol{\Sigma}_{\boldsymbol{\eta}} = \boldsymbol{I}_{d_{\boldsymbol{\varepsilon}}} \sigma_{\boldsymbol{\eta}}^2)$, where $\boldsymbol{I}_{d_{\boldsymbol{\varepsilon}}}$ is the $d_{\boldsymbol{\varepsilon}} \times d_{\boldsymbol{\varepsilon}}$ identity matrix. This error term is commonly added to FE-data for synthetic data generation, in order to incorporate the effects of added noise. Considering that the surrogate error was found to be statistically equivalent, it was decided that when the surrogate is used for synthetic data generation, no further noise addition would be required.

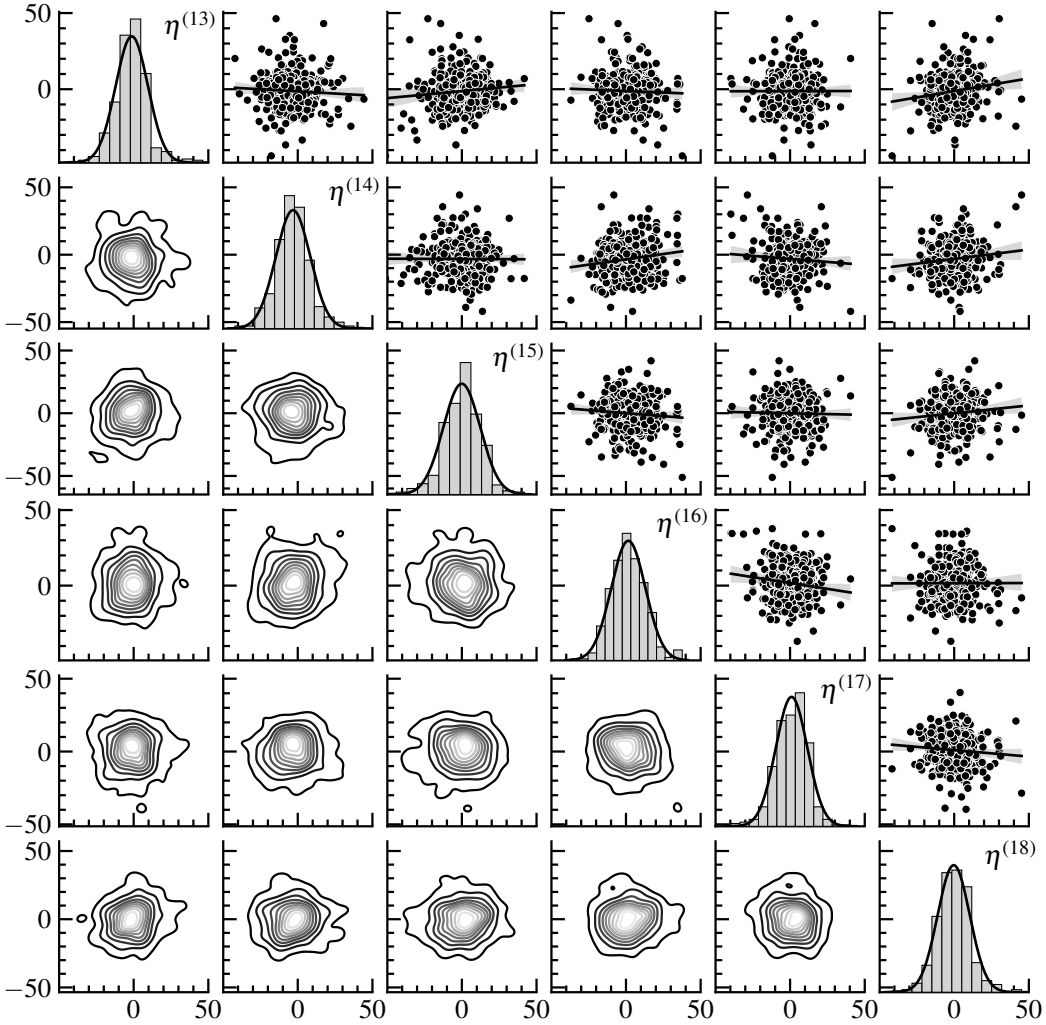

Figure 4.7: Involved error in the surrogate model construction.

Table 4.1: Surrogate model error distribution mean and standard deviation.

	ID 13	ID 14	ID 15	ID 16	ID 17	ID 18
$\mu_{\eta}^{(j)}[\mu\varepsilon]$	-1.3	-3.2	0.1	1.6	1.0	-0.3
$\sigma_{\eta}^{(j)}[\mu\varepsilon]$	10.8	11.5	12.3	11.4	10.5	10.7

Ultimately, with the trained ANN, a large set of predicted strain responses can be obtained for the purposes of adequately training the employed damage identification methods. Namely, applying the surrogate model $\mathcal{F}$ on the full set of an appropriate number of samples for the task at hand, e.g., N, gives: $\boldsymbol{D}^{\mathcal{F}} = \{\mathbf{x}_i; \hat{\boldsymbol{\varepsilon}}_i\}_{i=1}^{N}$. As described at the beginning of the previous

section, N for our case was estimated to be $\sim 10^4$, which can now be formally confirmed by producing a convergence plot of the Monte Carlo (MC) mean estimator of an indicative strain feature, as shown in Figure 4.8. Lower and upper bounds correspond to confidence intervals of 95%.

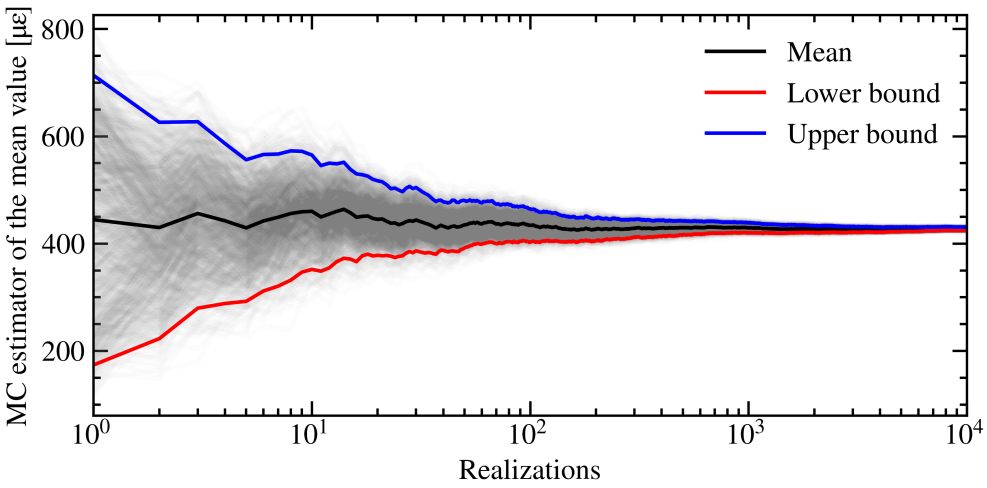

Figure 4.8: Monte Carlo convergence graph.

Chapter 5

Damage identification methods

In this chapter, using the essential theoretical context presented in the second chapter and tailoring it to the problem at hand, the formulation of the employed damage identification approaches is provided, and their performance is assessed on different representative damage scenarios. The first approach is termed as "detection theory-based approach" since elements from detection theory were used, while the second one is referred to as "probabilistic regression-based approach" to remain consistent with the original paper of Nix and Weigend [102].

5.1 Detection theory-based approach

In Section 2.4 it was mentioned that the Likelihood Ratio Test (LRT) is fundamentally built around binary detection problems. Thus, in order to use it to assess the existence of a damage feature that is described by a nominally continuous variable (i.e., herein, the amplitude W_o of out-of-plane deflections), this variable must be effectively described using a discrete expression. For this reason, it was decided that for the six plates in the damage-critical zone, the effective W_o range, i.e., $8 - 20$ mm, would be partitioned into $i = 12$ discrete damage states (DS-i), each corresponding to a range spanning 1 mm. Accordingly, DS1 corresponds to $W_o \in [8, 9]$ mm, DS2 to $W_o \in (9, 10]$, etc. For the healthy state H, on the other hand, it was considered that deflections would be measured after construction or repair operations during the quality assurance process, so they were taken to be deterministic and known a priori. Each damage state tested against a particular reference healthy state yields a distinct binary hypothesis test, which ultimately results in a total of 12 LRTs. For each test, the employed LRT-based detector will be called to determine whether the registered strain values correspond to the damage state in question. It is evident that the discretization of the problem not only enables damage identification but also offers a prediction range for the deflection magnitude.

According to the definition of the LRT provided in Section 2.4, it is necessary to select appropriate PDFs for the strain response data that correspond to the healthy and damaged states. For the latter, this amounts to 12 different PDFs, each corresponding to a particular damage state as defined earlier. In this work, non-parametric KDE-based PDFs were fitted using strain response data corresponding to each case obtained from the surrogate model using the following process. For the healthy state, since deflections were assumed deterministic, plates were assigned a particular instance of i.i.d. measure observations that were drawn from the lognormal distribution while ensuring that they lie under the damage threshold of 8 mm. Load realizations were subsequently obtained for each of the 72 loading conditions. This was achieved by drawing 140 samples from each loading condition using the joint PDF described in Equations (3.2) to (3.4). This ultimately led to a total of 10080 samples from the

random variables describing the input source variability. These were then fed to the surrogate to obtain an equal number of strain response samples, which were used to fit the KDE-based PDF for the healthy state. A similar process was employed to fit PDFs for the damaged states, with the only difference being that for the initial plate deflections of the six plates within the damage-critical zone, samples were drawn uniformly from each range. For example, for DS1, samples were drawn from $\mathcal{U}[8, 9]$, for DS2 from $\mathcal{U}[9, 10]$, and so on. Ultimately, a total of 13 data-sets were produced; one for the healthy class $\boldsymbol{D}_{\mathrm{H}}$, and 12 for the different damage classes, each labeled as $\boldsymbol{D}_{\mathrm{DS}-i}$. The estimated KDE densities corresponding to each structural condition are shown for a particular sensor (ID 14) in Figure 5.1. For this sensor, the out-of-plane deflection for the reference healthy state corresponds to 2.9 mm, as determined by the i.i.d sampling process. Observing Figure 5.1 reveals that as the level of damage increases, the overlap between the distributions decreases, suggesting that the proportion of misclassified strain data points will progressively decrease for more severe damage states.

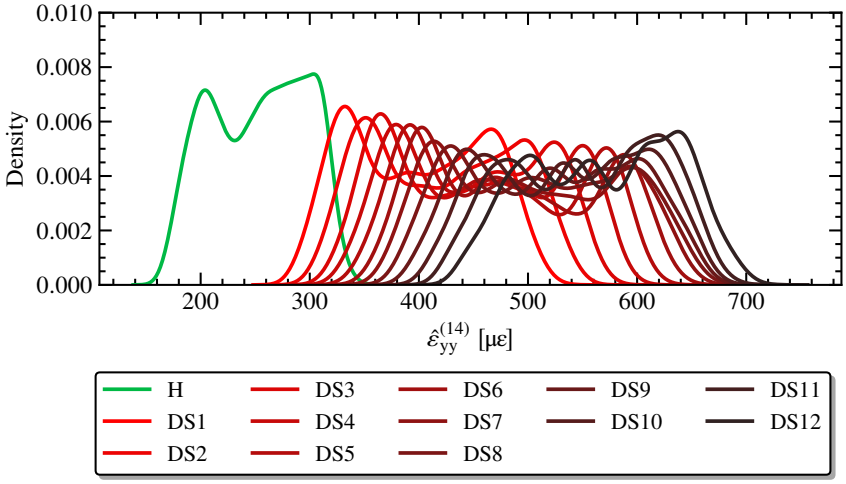

Figure 5.1: Estimated KDE densities for all damage states and the reference 2.9 mm healthy state (sensor ID 14).

The assessment of the detector was implemented in two stages for the same sensor, which was considered representative of the overall problem. In the first stage the probability of detection (P_{D}) curve was produced which shows the P_{D} as a function of the deflection level and for different acceptable probabilities of false alarm (P_{FA}). Since the estimates of the PDFs in Equation 2.24 are provided as the kernel density estimates under the reference healthy state H and the ith damage state DS-i, MC methods were employed to calculate the P_{D} given a specific acceptable P_{FA} level. Namely, for the reference healthy state the strain threshold ε_T corresponding to the desired P_{FA} was obtained from Equation 2.30 using the calculated empirical inverse CDF. Then the LRT (Equation 2.24) was conducted within an iterative process for every data point in the $\boldsymbol{D}_{\mathrm{DS}-i}$ considering this particular threshold value, and if the ratio was above it, the effective data point was counted as a TP. If the ratio for the occurring data point was below the threshold, the algorithm iterated to the next data point in

the sequence. The sum of the total TP divided by the number of elements in $\boldsymbol{D}_{\mathrm{DS}-i}$ yielded the P_{D} value for the ith hypothesis test. This process was repeated for every other P_{FA} level, while retaining the same data-sets. The results are summarized in Figure 5.2. Analyzing those results led to the conclusion that the employed detector was highly accurate, regardless of the false alarm threshold, for more severe damage states. Conversely, for those closer to the 8 mm threshold, its performance was overall diminished and also significantly affected by the imposed P_{FA} threshold.

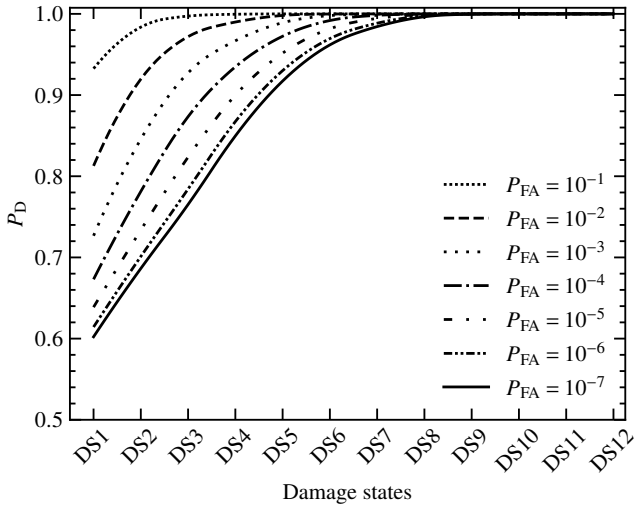

Figure 5.2: Detection performance for sensor ID 14 for different damage states for a 2.9 mm healthy state deflection magnitude.

In the second stage of assessing the performance of the proposed framework, ROC curves were produced for the detector that correspond to the different damage states and two different scenarios for the healthy state. In the first healthy state scenario, an out-of-plane deflection of 5 mm was considered, which corresponds to an intermediate case, while in the second the limit case was considered, i.e., 8 mm. Implementation-wise, generating the ROC curves involved defining a finite but sufficiently large set of thresholds $\varepsilon_{T,k}$ ranged from the minimum value of $\boldsymbol{D}_{\mathrm{H}}$ to the maximum value of $\boldsymbol{D}_{\mathrm{DS}-i}$. Next, a particular threshold value was chosen, and the likelihood ratio of each element in $\boldsymbol{D}_{\mathrm{DS}-i}$ was compared to that threshold. The trials above the threshold counted as TP, whereas the trials below the threshold counted as FP. The P_{FA} was then simply the ratio of the number of FP to the total number of the elements in $\boldsymbol{D}_{\mathrm{H}}$ (undamaged trials), and similarly the P_{D} was the ratio of TP to the number of elements in $\boldsymbol{D}_{\mathrm{DS}-i}$ (damaged trials). The process was repeated for all threshold values $\varepsilon_{T,k}$ and the resulting probability pairs were plotted. The ROC curves that correspond to the 5 mm case are plotted in Figure 5.3a while those corresponding to the 8 mm case are shown in Figure 5.3b. The gray area (lower triangle) represents a lack of information gain, and any conclusions drawn from it are based completely on random chance. The positive correlation between the magnitude of the excessive deflection and detector performance was confirmed by both sets of curves. Furthermore, what became clear was that detection performance was adversely

affected by the acceptable (healthy state) deflection magnitude. Taking all these findings into account, it may be concluded that the key factor determining detection performance was the relative difference between the out-of-plane deflection for the healthy and damaged states.

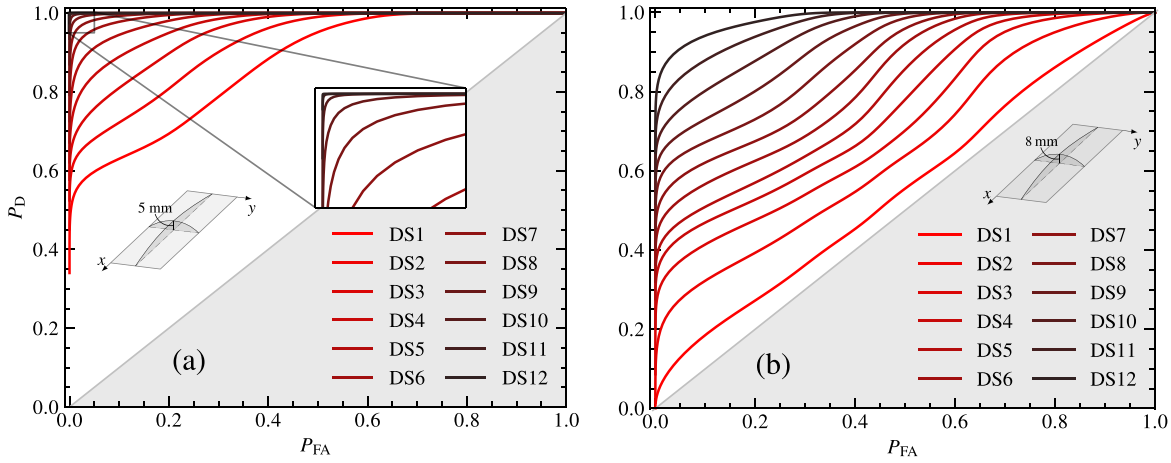

Figure 5.3: ROC curves (sensor ID 14) for a 5 mm (a) and an 8 mm (b) healthy state deflection magnitude.

5.2 Probabilistic regression-based approach

For the probabilistic regression-based approach, there is no need to discretize the problem since the employed mean–variance estimation (MVE) method is capable of learning a continuous mapping between monitored strains $\boldsymbol{\varepsilon}$ and out-of-plane deflections W_o. As mentioned in subsection 2.5.5, this method is capable of quantifying predictive uncertainty by assuming a Gaussian prediction error model, which in turn allows for the estimation of not only the mean W_o, but also the associated variance.

Two separate ANNs are employed by this method to learn the mappings between the inputs and mean and variance terms, which, for the sake of uniformity with the already-introduced notation, have been denoted here as NN_{W_o} and NN_{σ}, respectively. In the proposed damage identification framework, these were trained using data obtained from a single potential strain sensor $\varepsilon_{yy}^{(j)}$ of the damage-critical zone ($j = 13, \ldots, 18$) and sought to predict the mean and variance of the normally distributed W_o that corresponds to the same plate on which the sensor is located. Ultimately, the same 10080 load samples as in the detection theory-based case were employed, but this time out-of-plane deflections were drawn from a uniform distribution over the entire permissible range, i.e., $W_o \sim \mathcal{U}[0, 20]$ mm.

This is the fundamental difference between the two approaches, namely that the one using probabilistic regression does not require an a priori separation into different states (healthy and damaged). Rather, by efficiently learning to predict the parameters of the probability distribution of W_o, conditioned on strain response data, it is able to accommodate any deflection threshold, as long as it lies within its training set. Transforming the predicted W_o distribution into a decision on the existence of damage is straightforward and will be described later.

When it comes to the hyperparameters of the two ANNs, again as in the training process of the surrogate model, a heuristic trial-and-error process was employed to determine them. On the one hand, for NN_{W_o} two hidden layers with 16 neurons each were used between the 1-dimensional input and output layers. On the other hand, 3 hidden layers of 64, 64 and 32 units were required for NN_{σ}. For both networks, ReLU activation was used throughout except in the output layers, where a linear one was employed. However, since variance is by definition positive, the softplus function $\log(1 + \exp(\cdot))$ was passed through the second output to impose a positivity constraint, and also a minimum variance (i.e., 10^{-3}) was added for numerical stability. As in the detection theory-based approach, the training samples were obtained from the constructed surrogate model, and were split to 60% for training, 15% for validation, i.e., hyperparameter tuning, and the remaining 25% was used for testing the model. The data were standardized for the same reasons as stated in section 4.2, while no processing was applied to the targets and separated into batches of 128 prior to training. The NLL was used as the loss function, while Root Mean Square propagation (RMSprop) with a learning rate of 10^{-4} was selected to be the optimizer. A maximum of 3000 epochs was selected for training, but an early stopping criterion was employed with a patience of 300 epochs. This meant that if the NLL for the validation set failed to improve for 300 successive epochs, then training was to be terminated.

The evolution of the NLL over the training epochs is plotted for the same sensor as in the first method (i.e., ID 14) in Figure 5.4a for a representative instance of training the model. As indicated, the early stopping criterion has been triggered and $\sim$ 2570 epochs were required for training, while it is clear that no overfitting has occurred. The predictive capabilities of the trained model are illustrated in Figure 5.4a. In that, instances of W_o from the test set are depicted using a scatter plot, while the mean prediction of the probabilistic regression model is plotted with the red curve and the 95% PIs with the green curves. Observing the figure it is made clear that the trained model was capable of capturing the mean behavior of the data, as well as their heteroscedastic behavior. Moreover, an illustrative example of the out-of-plane deflection PDFs is provided using the blue curves, which correspond to different potential strain response measurements.

Apart from the visual inspection, the PICP and PINAW indexes introduced in subsection 2.5.5 were used to evaluate the quality of the constructed PIs, which is indicative of the model's performance. Namely, the acquired values were PICP = 96.90% and PINAW = 46.56%, which indicate high percentage of coverage, i.e., higher than the preset confidence level, and relatively narrow widths considering the intrinsically high sparsity of W_o data. These results further support our assertion that the model generates predictions with high accuracy and fairly high certainty. Furthermore, the PICP index can be visually interpreted by Figure 5.5. On the x-axis of the plot are the true targets of W_o and on the y-axis are the predicted distributions of W_o, where the 95th percentiles are shown as vertical blue bars. Green and red dots represent

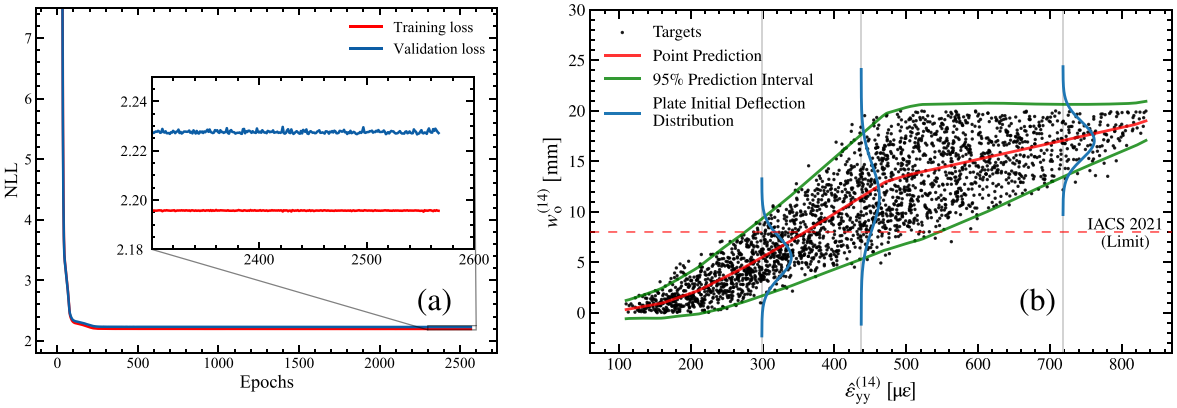

Figure 5.4: Evolution of NLL loss function over epochs (a) and probabilistic regression model predictions for the mean and 95% PIs versus target data (b) corresponding to sensor ID 14.

the means of the distributions, where green denotes that the true W_o falls within the 95th percentile range ("hit") and red denotes that it does not ("miss"). As already suggested by the PICP index, this model has 97% hits and 3% misses, meaning that it tends to be slightly under-confident in its predictions.

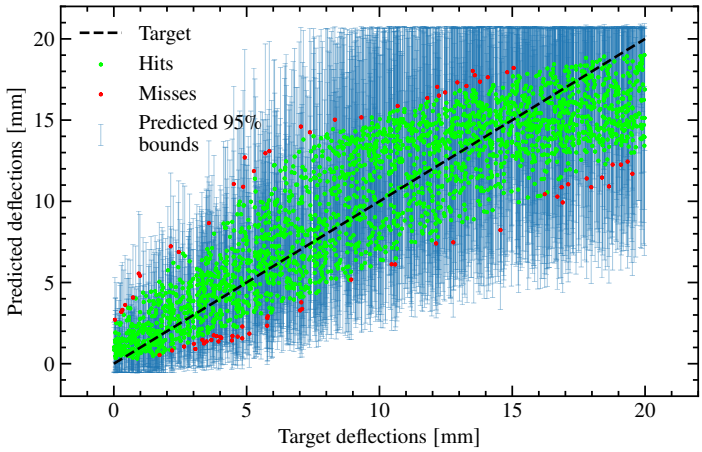

Figure 5.5: Performance of the probabilistic regression model for the synthetic deflection data.

As mentioned, with the trained model at hand it is fairly simple to tackle the damage detection problem. The process that may be followed is illustrated in Figure 5.6. As a first step, an alarm threshold of $W_o = 8$ mm is considered. Due to the presence of uncertainty, this cannot be mapped to a unique strain value by which to obtain a strain threshold for damage identification. As evidenced by Figure 5.6a, a potential strain reading may correspond to various out-of-plane deflections, associated with a different probability of occurrence. Therefore, in order to set the strain threshold, the out-of-plane deflection threshold must be associated with some probability of occurrence, or more pertinently for this case a probability of exceedance. This constitutes a particularly reasonable choice since it imbues the system with a consideration of risk, expressed as the maximum allowed probability of damage occurrence.

Thus, a more accurate description of the alarm threshold would be that of the strain measurement

for which $\Pr[W_o \geq 8] = 5\%$. This threshold can be readily obtained using the trained probabilistic regression model through a simple grid search process which, for the case illustrated in Figure 5.6, led to an estimated value of $\varepsilon_T = 286$ με. With that in hand, the trained model can be leveraged again to estimate the probability of detection and probability of false alarm. More specifically, 10^4 W_o samples were generated for every strain response value contained in the test set. Then, the strain measurements for which the generated W_o samples were up to 0.1% from $W_o = 8$ mm were retained and plotted using a histogram (see Figure 5.6b) on top of which then a KDE-based PDF was fitted (see Figure 5.6c). Using that PDF and the strain response threshold determined earlier, the probability of false alarm can be stated as $P_{FA} = \Pr[\varepsilon \leq \varepsilon_T]$, which can be easily calculated using the Cumulative Density Function (CDF) of the strain distribution, which is depicted in Figure 5.6d. The complement of this probability can be viewed as an equivalent expression of the probability of detection. Considering that adapting this process to any threshold value associated with a desirable probability of exceedance, highlights the versatility of the probabilistic regression-based approach. However, it must be noted that the method is bound by a strong assumption in terms of the distribution model of the predictions, which might hinder its accuracy in cases where more complex data distributions are observed or when they span higher dimensions.

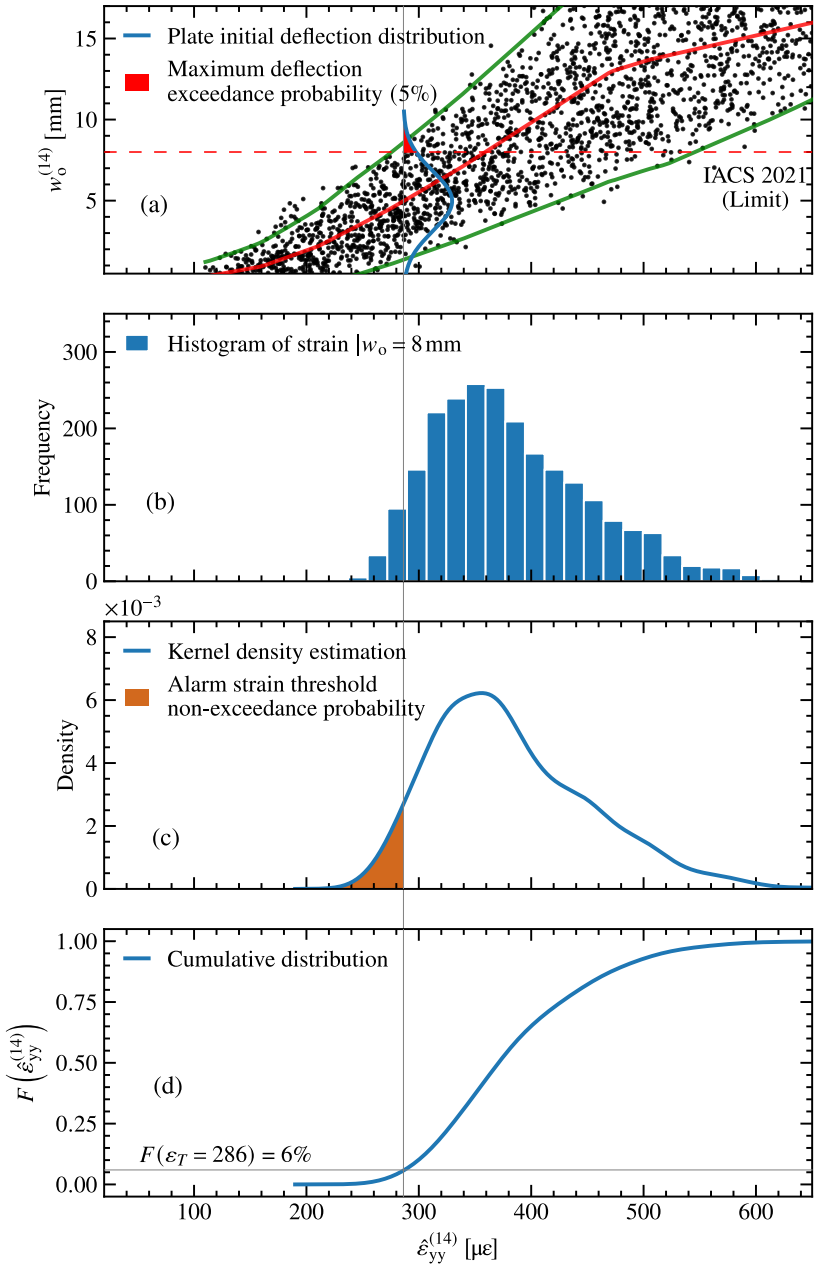

Figure 5.6: Probability of non-exceedance of alarm strain threshold for a given exceedance probability (5% selected herein) of the maximum allowable deflection (8 mm).

Chapter 6

Concluding remarks

The goal of the present work was to investigate an SHM system for damage identification of excessive plate deflections in large-scale ship structures, which constitute a particularly important damage mode as they may act as triggers for buckling collapse. The implementation of the methods was carried out in a numerical setting, using a high-fidelity FE model and an ANN-based surrogate to generate synthetic strain response data. Different sources of uncertainty affecting structural loading, as well as the damage mode, were considered and propagated to the synthetic data through an MCS. Static strain response was employed as the damage-sensitive feature, with the particular strain monitoring locations and components selected by an exploratory analysis of the strain response.

Two alternative methods for damage identification were employed, both capable of quantifying predictive uncertainty. The first employed a detection theory-based approach which treated the problem as a series of binary classification tasks between a healthy state and damaged states corresponding to progressively more severe damage levels. The method showcased decreased accuracy for less severe damage cases, thus compromising its potential for early detection. Conversely, the alternative method, based around a probabilistic regression model (MVE method), which mapped strain to out-of-plane deflection was proven to be more robust to damage extent. Furthermore, it offers significantly greater flexibility as it does not require discretizing the problem into different binary ones and can also account for varying thresholds. Moreover, it offers an inherent quantification of decision-related risk as it requires a probability of exceedance for a specific out-of-plane detection threshold in order to set corresponding strain measurement alarm thresholds. Despite its improved flexibility, it may still be insufficient for high-dimensional problems or ones where the predictive data distribution is complex, due to its assumption of Gaussian prediction error at each point. Finally, it is by definition not capable to update its predictive capacity as more data becomes available, a task for which Bayesian methods are suitable and which can be viewed as a natural extension to this work. Essentially, Bayesian methods relate to probabilistic approaches for model updating (inverse problem) where the goal is to evaluate the posterior PDF of the unknown model parameters that are of interest conditioned on the measured data. The deployment of more complex sensor topologies coupled with optimization of sensor placements is also encouraged, either within the framework shown here or by applying the Bayesian approach mentioned previously.

References

[1] IACS-REC 84, *Guidelines for surveys, assessment and repair of hull structures—container ships, rev. 1*, International Association of Classification Societies, https://iacs.org.uk/download/1870, November 2017 [last accessed May 5, 2023].

[2] G. Wang, C. Serratella, and S. Kalghatgi, "1 - Current practices in condition assessment of aged ships and floating offshore structures", in *Condition Assessment of Aged Structures*, ser. Woodhead Publishing Series in Civil and Structural Engineering, J. K. Paik and R. E. Melchers, Eds., Cambridge England: Woodhead Publishing, 2008, pp. 3–35. DOI: 10.1533/9781845695217.1.3.

[3] P. Hess *et al.*, "Report of the ISSC technical committee V.7 — Structural Longevity", in *Proceedings of the 19th International Ship and Offshore Structures Congress (ISSC)*, vol. 2, UK: Taylor Francis Ltd. (CRC press), 2015, pp. 817–864.

[4] IACS-REC 106, *IACS guideline for rule development — ship structure.* International Association of Classification Societies, https://iacs.org.uk/download/1903, July 2009 [last accessed May 5, 2023].

[5] ClassNK, *Investigation report on structural safety of large container ships*. Tokyo, Japan: The investigative panel on large container ship safety, 2014, September 2014, https://www.classnk.or.jp/hp/pdf/news/Investigation_Report_on_Structural_Safety_of_Large_Container_Ships_EN_ClassNK.pdf [last accessed May 5, 2023].

[6] Y. Sumi *et al.*, *Interim report of committee on large container ship safety*. Tokyo, Japan: Committee on large container ship safety, Maritime Bureau of Japan's Ministry of Land, Infrastructure, Transport and Tourism (MILT), 2013, December 2013, http://www.mlit.go.jp/common/001029660.pdf [last accessed May 5, 2023].

[7] Y. Sumi *et al.*, *Final report of committee on large container ship safety*. Tokyo, Japan: Committee on large container ship safety, Maritime Bureau of Japan's Ministry of Land, Infrastructure, Transport and Tourism (MILT), 2015, March 2015, http://www.mlit.go.jp/common/001081297.pdf [last accessed May 5, 2023].

[8] R. Ahmad and S. Kamaruddin, "An overview of time-based and condition-based maintenance in industrial application", *Computers and Industrial Engineering*, vol. 63, no. 1, pp. 135–149, 2012, ISSN: 0360-8352. DOI: 10.1016/j.cie.2012.02.002.

[9] R. Xie, M. Chen, W. Liu, H. Jian, and Y. Shi, "Digital twin technologies for turbomachinery in a life cycle perspective: A review", *Sustainability*, vol. 13, no. 5, e2495, 2021. DOI: 10.3390/su13052495.

[10] K. Reifsnider and P. Majumdar, "Multiphysics stimulated simulation digital twin methods for fleet management", in *54th AIAA/ASME/ASCE/AHS/ASC Structures, Structural Dynamics, and Materials Conference*. DOI: 10.2514/6.2013-1578.

[11] K. Worden, E. J. Cross, R. J. Barthorpe, D. J. Wagg, and P. Gardner, "On Digital Twins, Mirrors, and Virtualizations: Frameworks for Model Verification and Validation", *ASCE-ASME Journal of Risk and Uncertainty in Engineering Systems, Part B: Mechanical Engineering*, vol. 6, no. 3, e030902, May 2020. DOI: 10.1115/1.4046740.

[12] P. Hess *et al.*, "Report of the ISSC technical committee V.7 — Structural Longevity", in *Proceedings of the 20th International Ship and Offshore Structures Congress (ISSC)*, IOS Press, vol. 2, 2018, pp. 391–460.

[13] H. Millwater, J. Ocampo, and N. Crosby, "Probabilistic methods for risk assessment of airframe digital twin structures", *Engineering Fracture Mechanics*, vol. 221, e106674, 2019, ISSN: 0013-7944. DOI: 10.1016/j.engfracmech.2019.106674.

[14] Z. B. Miled and M. O. French, "Towards a reasoning framework for digital clones using the digital thread", in *55th AIAA Aerospace Sciences Meeting*. DOI: 10.2514/6.2017-0873.

[15] R. Bitton *et al.*, "Deriving a cost-effective digital twin of an ics to facilitate security evaluation", in *Computer Security*, J. Lopez, J. Zhou, and M. Soriano, Eds., Cham: Springer International Publishing, 2018, pp. 533–554.

[16] P. M. Karve, Y. Guo, B. Kapusuzoglu, S. Mahadevan, and M. A. Haile, "Digital twin approach for damage-tolerant mission planning under uncertainty", *Engineering Fracture Mechanics*, vol. 225, e106766, 2020. DOI: 10.1016/j.engfracmech.2019.106766.

[17] E. Glaessgen and D. Stargel, "The digital twin paradigm for future nasa and u.s. air force vehicles", in *53rd AIAA/ASME/ASCE/AHS/ASC Structures, Structural Dynamics and Materials Conference*. DOI: 10.2514/6.2012-1818.

[18] C. Zhou *et al.*, "Analytics with digital-twinning: A decision support system for maintaining a resilient port", *Decision Support Systems*, vol. 143, e113496, 2021, ISSN: 0167-9236. DOI: 10.1016/j.dss.2021.113496.

[19] M. Macchi, I. Roda, E. Negri, and L. Fumagalli, "Exploring the role of digital twin for asset lifecycle management", *IFAC-PapersOnLine*, vol. 51, no. 11, pp. 790–795, 2018, 16th IFAC Symposium on Information Control Problems in Manufacturing INCOM 2018. DOI: 10.1016/j.ifacol.2018.08.415.

[20] C. Li, S. Mahadevan, Y. Ling, S. Choze, and L. Wang, "Dynamic bayesian network for aircraft wing health monitoring digital twin", *AIAA Journal*, vol. 55, pp. 930–941, 2017.

[21] Z. Pietrzykowski and J. Hajduk, "Operations of maritime autonomous surface ships", *TransNav, the International Journal on Marine Navigation and Safety of Sea Transportation*, vol. 13, no. 4, pp. 725–733, 2019. DOI: 10.12716/1001.13.04.04.

[22] ABS, *Enhancing safety on FPSOs: Leveraging digital technologies*, American Bureau of Shipping, https://ww2.eagle.org/content/dam/eagle/advisories-and-debriefs/ABS_Enhancing_Safety_on_FPSOs_Leveraging_Digital_Technologies.pdf, 2022 [last accessed May 5, 2023].

[23] ClassNK, *ClassNK digital ground design 2030*, Nippon Kaiji Kyokai, https://www.classnk.or.jp/hp/en/activities/techservices/dgd2030/index.html, 2020 [last accessed May 5, 2023].

[24] O. Smogeli, *Digital twins at work in maritime and energy.* DNV GL, https://www.dnvgl.com/Images/DNV%20GL%20Feature%20%2303%20ORIG2b_tcm8-85106.pdf, 2017 [last accessed May 5, 2023].

[25] C. R. Farrar and K. Worden, "An introduction to structural health monitoring", *Philosophical Transactions of the Royal Society A: Mathematical, Physical and Engineering Sciences*, vol. 365, no. 1851, pp. 303–315, 2007. DOI: 10.1098/rsta.2006.1928.

[26] C.-P. Fritzen and P. Kraemer, "Self-diagnosis of smart structures based on dynamical properties", *Mechanical Systems and Signal Processing*, vol. 23, no. 6, pp. 1830–1845, 2009, Special Issue: Inverse Problems, ISSN: 0888-3270. DOI: 10.1016/j.ymssp.2009.01.006.

[27] A. Rytter, "Vibrational based inspection of civil engineering structures", Ph.D. dissertation, Aalborg University, Denmark, 1993.

[28] R. Barthorpe, "On model- and data-based approaches to structural health monitoring", Ph.D. dissertation, Department of Mechanical Engineering, University of Sheffield, 2011.

[29] C. R. Farrar and K. Worden, *Structural Health Monitoring: A Machine Learning Perspective*. John Wiley & Sons, Ltd, 2012. DOI: 10.1002/9781118443118.

[30] K. Worden, C. R. Farrar, G. Manson, and G. Park, "The fundamental axioms of structural health monitoring", *Proceedings of the Royal Society A: Mathematical, Physical and Engineering Sciences*, vol. 463, no. 2082, pp. 1639–1664, 2007. DOI: 10.1098/rspa.2007.1834.

[31] S. W. Doebling, C. R. Farrar, M. B. Prime, and D. W. Shevitz, *Damage identification and health monitoring of structural and mechanical systems from changes in their vibration characteristics: A literature review*. Washington, DC: Los Alamos National Lab, 1996. DOI: http://doi.org/10.2172/249299.

[32] H. Sohn, C. R. Farrar, F. M. Hemez, and J. J. Czarnecki, *A Review of Structural Health Monitoring Literature : 1996-2001; Los Alamos National Laboratory Report, LA-13976-MS.* Washington, DC: Los Alamos National Lab, 2004.

[33] W. Fan and P. Qiao, "Vibration-based Damage Identification Methods: A Review and Comparative Study", *Struct. Health Monit.*, vol. 10, no. 1, pp. 83–111, 2011. DOI: http://doi.org/10.1177/1475921710365419.

[34] S. Pereira, F. Magalhães, J. P. Gomes, Á. Cunha, and J. V. Lemos, "Vibration-based damage detection of a concrete arch dam", *Eng. Struct.*, vol. 235, e112032, 2021, ISSN: 0141-0296. DOI: http://doi.org/10.1016/j.engstruct.2021.112032.

[35] O. Avci, O. Abdeljaber, S. Kiranyaz, M. Hussein, M. Gabbouj, and D. J. Inman, "A review of vibration-based damage detection in civil structures: From traditional methods to Machine Learning and Deep Learning applications", *Mech. Syst. Signal Process.*, vol. 147, e107077, 2021, ISSN: 0888-3270. DOI: http://doi.org/10.1016/j.ymssp.2020.107077.

[36] Z. Zhou, L. D. Wegner, and B. F. Sparling, "Data quality indicators for vibration-based damage detection and localization", *Eng. Struct.*, vol. 230, e111703, 2021, ISSN: 0141-0296. DOI: http://doi.org/10.1016/j.engstruct.2020.111703.

[37] E. Tronci, M. De Angelis, R. Betti, and V. Altomare, "Vibration-based structural health monitoring of a RC-masonry tower equipped with non-conventional TMD", *Eng. Struct.*, vol. 224, e111212, 2020, ISSN: 0141-0296. DOI: http://doi.org/10.1016/j.engstruct.2020.111212.

[38] D. Anastasopoulos, M. D. Smedt, L. Vandewalle, G. D. Roeck, and E. P. Reynders, "Damage identification using modal strains identified from operational fiber-optic Bragg grating data", *Struct. Health Monit.*, vol. 17, no. 6, pp. 1441–1459, 2018. DOI: http://doi.org/10.1177/1475921717744480.

[39] F. Lorenzoni, F. Casarin, M. Caldon, K. Islami, and C. Modena, "Uncertainty quantification in structural health monitoring: Applications on cultural heritage buildings", *Mech. Syst. Signal Process.*, vol. 66-67, pp. 268–281, 2016, ISSN: 0888-3270. DOI: http://doi.org/10.1016/j.ymssp.2015.04.032.

[40] A. Panopoulou, T. Loutas, D. Roulias, S. Fransen, and V. Kostopoulos, "Dynamic fiber Bragg gratings based health monitoring system of composite aerospace structures", *Acta Astronaut.*, vol. 69, no. 7, pp. 445–457, 2011, ISSN: 0094-5765. DOI: http://doi.org/10.1016/j.actaastro.2011.05.027.

[41] T. Loutas and A. Bourikas, "Strain sensors optimal placement for vibration-based structural health monitoring. The effect of damage on the initially optimal configuration", *J. Sound Vib.*, vol. 410, pp. 217–230, 2017, ISSN: 0022-460X. DOI: http://doi.org/10.1016/j.jsv.2017.08.022.

[42] J. Alvarez-Montoya, A. Carvajal-Castrillón, and J. Sierra-Pérez, "In-flight and wireless damage detection in a UAV composite wing using fiber optic sensors and strain field pattern recognition", *Mech. Syst. Signal Process.*, vol. 136, e106526, 2020, ISSN: 0888-3270. DOI: http://doi.org/10.1016/j.ymssp.2019.106526.

[43] D. Ma and D. Wang, "A deep learning-based method for hull stiffened plate crack detection", *Proc. Inst. Mech. Eng. Part M- J. Eng. Marit. Environ.*, vol. 235, no. 2, pp. 570–585, 2021. DOI: http://doi.org/10.1177/1475090220966465.

[44] A. Budipriyanto, M. Haddara, and A. Swamidas, "Identification of damage on ship's cross stiffened plate panels using vibration response", *Ocean Eng.*, vol. 34, no. 5, pp. 709–716, 2007, ISSN: 0029-8018. DOI: http://doi.org/10.1016/j.oceaneng.2006.05.009.

[45] A. Zubaydi, M. Haddara, and A. Swamidas, "Damage identification in a ship's structure using neural networks", *Ocean Eng.*, vol. 29, no. 10, pp. 1187–1200, 2002, ISSN: 0029-8018. DOI: http://doi.org/10.1016/S0029-8018(01)00077-4.

[46] M. M. Luczak, J. Telega, N. Zagato, and E. Mucchi, "On the damage detection of a laboratory scale model of a tripod supporting structure by vibration-based methods", *Mar. Struct.*, vol. 64, pp. 146–160, 2019, ISSN: 0951-8339. DOI: http://doi.org/10.1016/j.marstruc.2018.11.002.

[47] M. Mieloszyk and W. Ostachowicz, "An application of Structural Health Monitoring system based on FBG sensors to offshore wind turbine support structure model", *Mar. Struct.*, vol. 51, pp. 65–86, 2017, ISSN: 0951-8339. DOI: http://doi.org/10.1016/j.marstruc.2016.10.006.

[48] W.-H. Hu, S. Thöns, R. G. Rohrmann, S. Said, and W. Rücker, "Vibration-based structural health monitoring of a wind turbine system Part II: Environmental/operational effects on dynamic properties", *Eng. Struct.*, vol. 89, pp. 273–290, 2015, ISSN: 0141-0296. DOI: http://doi.org/10.1016/j.engstruct.2014.12.035.

[49] Y. Ou, E. N. Chatzi, V. K. Dertimanis, and M. D. Spiridonakos, "Vibration-based experimental damage detection of a small-scale wind turbine blade", *Struct. Health Monit.*, vol. 16, no. 1, pp. 79–96, 2017. DOI: http://doi.org/10.1177/1475921716663876.

[50] Y. Ou, K. E. Tatsis, V. K. Dertimanis, M. D. Spiridonakos, and E. N. Chatzi, "Vibration-based monitoring of a small-scale wind turbine blade under varying climate conditions. Part I: An experimental benchmark", *Struct. Control Health Monit.*, vol. 28, e2660, 6 2021, ISSN: 15452263. DOI: http://doi.org/10.1002/stc.2660.

[51] J. N. Kudva, N. Munir, and P. W. Tan, "Damage detection in smart structures using neural networks and finite-element analyses", *Smart Materials and Structures*, vol. 1, no. 2, p. 108, Jun. 1992. DOI: 10.1088/0964-1726/1/2/002.

[52] K. Worden, A. D. Ball, and G. R. Tomlinson, "Fault location in a framework structure using neural networks", *Smart Materials and Structures*, vol. 2, no. 3, p. 189, Sep. 1993. DOI: 10.1088/0964-1726/2/3/007.

[53] C. Sbarufatti, A. Manes, and M. Giglio, "Performance optimization of a diagnostic system based upon a simulated strain field for fatigue damage characterization", *Mech. Syst. Signal Process.*, vol. 40, no. 2, pp. 667–690, 2013, ISSN: 0888-3270. DOI: http://doi.org/10.1016/j.ymssp.2013.06.003.

[54] S. Goossens *et al.*, "A global assessment of barely visible impact damage for CFRP sub-components with FBG-based sensors", *Compos. Struct.*, vol. 272, e114025, 2021, ISSN: 0263-8223. DOI: http://doi.org/10.1016/j.compstruct.2021.114025.

[55] T. Bergmayr, S. Höll, C. Kralovec, and M. Schagerl, "Local residual random forest classifier for strain-based damage detection and localization in aerospace sandwich structures", *Compos. Struct.*, vol. 304, e116331, 2023, ISSN: 0263-8223. DOI: http://doi.org/10.1016/j.compstruct.2022.116331.

[56] D. P. Milanoski and T. H. Loutas, "Strain-based health indicators for the structural health monitoring of stiffened composite panels", *Journal of Intelligent Material Systems and Structures*, vol. 32, no. 3, pp. 255–266, 2021. DOI: http://doi.org/10.1177/1045389X20924822.

[57] T. Bergmayr, M. Winklberger, C. Kralovec, and M. Schagerl, "Structural health monitoring of aerospace sandwich structures via strain measurements along zero-strain trajectories", *Eng. Fail. Anal.*, vol. 126, e105454, 2021, ISSN: 1350-6307. DOI: http://doi.org/10.1016/j.engfailanal.2021.105454.

[58] F. Terroba, M. Frövel, and R. Atienza, "Structural health and usage monitoring of an unmanned turbojet target drone", *Struct. Health Monit.*, vol. 18, no. 2, pp. 635–650, 2019. DOI: http://doi.org/10.1177/1475921718764082.

[59] S. R. Hunt and I. G. Hebden, "Validation of the Eurofighter Typhoon structural health and usage monitoring system", *Smart Mater. Struct.*, vol. 10, no. 3, 497, Jun. 2001. DOI: http://doi.org/10.1088/0964-1726/10/3/311.

[60] K. N. Anyfantis, "An abstract approach toward the structural digital twin of ship hulls: A numerical study applied to a box girder geometry", *Proceedings of the Institution of Mechanical Engineers, Part M: Journal of Engineering for the Maritime Environment*, vol. 235, no. 3, pp. 718–736, 2021. DOI: 10.1177/1475090221989188.

[61] N. E. Silionis and K. N. Anyfantis, "Static strain-based identification of extensive damages in thin-walled structures", *Structural Health Monitoring*, 2021. DOI: 10.1177/14759217211050605.

[62] N. E. Silionis and K. N. Anyfantis, "On the detection of thickness loss in ship hull structures through strain sensing", in *European Workshop on Structural Health Monitoring*, P. Rizzo and A. Milazzo, Eds., Cham: Springer International Publishing, 2023, pp. 207–216.

[63] C. R. Farrar, S. W. Doebling, and D. A. Nix, "Vibration–based structural damage identification", *Philosophical Transactions of the Royal Society of London. Series A: Mathematical, Physical and Engineering Sciences*, vol. 359, no. 1778, pp. 131–149, 2001. DOI: 10.1098/rsta.2000.0717.

[64] S. M. Kay, *Fundamentals of Statistical Signal Processing: Detection theory*. Prentice-Hall PTR, 1998.

[65] A. S. Katsoudas, N. E. Silionis, and K. N. Anyfantis, "Structural health monitoring for corrosion induced thickness loss in marine plates subjected to random loads", *Ocean Eng.*, vol. 273, e114037, 2023. DOI: https://doi.org/10.1016/j.oceaneng.2023.114037.

[66] N. Cholevas, K. N. Anyfantis, G. Mußbach, G. Korompili, and C. Riziotis, "Crack identification in solid rocket motors through the neyman–pearson detection theory", *AIAA J.*, vol. 0, no. 0, pp. 1–14, 0. DOI: https://doi.org/10.2514/1.J062728.

[67] N. E. Silionis and K. N. Anyfantis, "Data-driven probabilistic quantification and assessment of the prediction error model in damage detection applications", *Probab. Eng. Mech.*, vol. 71, e103412, 2023, ISSN: 0266-8920. DOI: https://doi.org/10.1016/j.probengmech.2023.103412.

[68] L. Colombo, M. Todd, C. Sbarufatti, and M. Giglio, "On statistical multi-objective optimization of sensor networks and optimal detector derivation for structural health monitoring", *Mech. Syst. Signal Process.*, vol. 167, e108528, 2022, ISSN: 0888-3270. DOI: https://doi.org/10.1016/j.ymssp.2021.108528.

[69] T. Liangou, A. Katsoudas, N. Silionis, and K. Anyfantis, "Statistical pattern recognition for optimal sensor placement in damage detection applications", in *European Workshop on Structural Health Monitoring*, P. Rizzo and A. Milazzo, Eds., Cham: Springer International Publishing, 2023, pp. 217–226.

[70] M. A. Vega and M. D. Todd, "A variational bayesian neural network for structural health monitoring and cost-informed decision-making in miter gates", *Struct. Health Monit.*, vol. 21, no. 1, pp. 4–18, 2022. DOI: https://doi.org/10.1177/1475921720904543.

[71] A. Amer and F. Kopsaftopoulos, "Gaussian process regression for active sensing probabilistic structural health monitoring: Experimental assessment across multiple damage and loading scenarios", *Struct. Health Monit.*, vol. 22, no. 2, pp. 1105–1139, 2023. DOI: https://doi.org/10.1177/14759217221098715.

[72] Q.-A. Wang, C. Zhang, Z.-G. Ma, and Y.-Q. Ni, "Modelling and forecasting of shm strain measurement for a large-scale suspension bridge during typhoon events using variational heteroscedastic gaussian process", *Eng. Struct.*, vol. 251, e113554, 2022. DOI: https://doi.org/10.1016/j.engstruct.2021.113554.

[73] M. Pereira and B. Glisic, "Detection and quantification of temperature sensor drift using probabilistic neural networks", *Expert Systems with Applications*, vol. 213, e118884, 2023. DOI: https://doi.org/10.1016/j.eswa.2022.118884.

[74] J. Chen and Y. Liu, "Probabilistic physics-guided machine learning for fatigue data analysis", *Expert Systems with Applications*, vol. 168, e114316, 2021. DOI: https://doi.org/10.1016/j.eswa.2020.114316.

[75] R. E. Melchers and A. T. Beck, *Structural Reliability Analysis and Prediction*, 3th. New York, NY: John Wiley and Sons Inc., 2018.

[76] R. Ranganathan, *Structural Reliability Analysis and Design*. Jaico Publishing House, 1999.

[77] M. Arnst and J.-P. Ponthot, "An overview of nonintrusive characterization, propagation, and sensitivity analysis of uncertainties in computational mechanics", *International Journal for Uncertainty Quantification*, vol. 4, no. 5, pp. 387–421, 2014, ISSN: 2152-5080.

[78] *Randomized Designs — pyDOE 0.3.6 documentation*, https://pythonhosted.org/pyDOE/randomized.html, [last accessed May 5, 2023].

[79] M. A. Fakih, M. Chiachío, J. Chiachío, and S. Mustapha, "A bayesian approach for damage assessment in welded structures using lamb-wave surrogate models and minimal sensing", *NDT & E International*, vol. 128, e102626, 2022, ISSN: 0963-8695. DOI: https://doi.org/10.1016/j.ndteint.2022.102626.

[80] M. K. Ramancha, M. A. Vega, J. P. Conte, M. D. Todd, and Z. Hu, "Bayesian model updating with finite element vs surrogate models: Application to a miter gate structural system", *Engineering Structures*, vol. 272, e114901, 2022, ISSN: 0141-0296. DOI: https://doi.org/10.1016/j.engstruct.2022.114901.

[81] D. Cristiani, C. Sbarufatti, and M. Giglio, "Damage diagnosis and prognosis in composite double cantilever beam coupons by particle filtering and surrogate modelling", *Structural Health Monitoring*, vol. 20, no. 3, pp. 1030–1050, 2021. DOI: https://doi.org/10.1177/1475921720960067.

[82] D. Cristiani, C. Sbarufatti, F. Cadini, and M. Giglio, "Fatigue damage diagnosis and prognosis of an aeronautical structure based on surrogate modelling and particle filter", *Structural Health Monitoring*, vol. 20, no. 5, pp. 2726–2746, 2021. DOI: https://doi.org/10.1177/1475921720971551.

[83] T. Bhattacharyya, S. Brat Singh, S. Sikdar (Dey), S. Bhattacharyya, W. Bleck, and D. Bhattacharjee, "Microstructural prediction through artificial neural network (ann) for development of transformation induced plasticity (trip) aided steel", *Materials Science and Engineering: A*, vol. 565, pp. 148–157, 2013. DOI: https://doi.org/10.1016/j.msea.2012.11.110.

[84] T. Pham *et al.*, "Characterization, propagation, and sensitivity analysis of uncertainties in the directed energy deposition process using a deep learning-based surrogate model", *Probabilistic Engineering Mechanics*, vol. 69, e103297, 2022, ISSN: 0266-8920. DOI: https://doi.org/10.1016/j.probengmech.2022.103297.

[85] P. Kersaudy, B. Sudret, N. Varsier, O. Picon, and J. Wiart, "A new surrogate modeling technique combining kriging and polynomial chaos expansions – application to uncertainty analysis in computational dosimetry", *Journal of Computational Physics*, vol. 286, pp. 103–117, 2015, ISSN: 0021-9991. DOI: https://doi.org/10.1016/j.jcp.2015.01.034.

[86] K. J. Bathe, *Finite element procedures in engineering analysis*. Prentice-Hall, 1982.

[87] R. D. Cook *et al.*, *Concepts and applications of finite element analysis*, 4th ed. John wiley & sons, 2007.

[88] J. K. Paik, *Ultimate limit state analysis and design of plated structures*. Chichester, UK: John Wiley & Sons, 2018.

[89] I. Goda, M. Assidi, and J. F. Ganghoffer, "Equivalent mechanical properties of textile monolayers from discrete asymptotic homogenization", *Journal of the Mechanics and Physics of Solids*, vol. 61, no. 12, pp. 2537–2565, 2013. DOI: 10.1016/j.jmps.2013.07.014.

[90] S. Ahmad, B. M. Irons, and O. Zienkiewicz, "Analysis of thick and thin shell structures by curved finite elements", *International journal for numerical methods in engineering*, vol. 2, no. 3, pp. 419–451, 1970. DOI: 10.1002/nme.1620020310.

[91] J. Marcum, "A statistical theory of target detection by pulsed radar", *IRE Transactions on Information Theory*, vol. 6, no. 2, pp. 59–267, 1960. DOI: 10.1109/TIT.1960.1057560.

[92] W. Peterson, T. Birdsall, and W. Fox, "The theory of signal detectability", *Transactions of the IRE Professional Group on Information Theory*, vol. 4, no. 4, pp. 171–212, 1954. DOI: 10.1109/TIT.1954.1057460.

[93] D. M. Green and J. A. Swets, *Signal detection theory and psychophysics*. New York: John Wiley, 1966, vol. 1.

[94] K. P. Murphy, *Machine learning: a probabilistic perspective*. Cambridge, Massachusetts, London, England: MIT press, 2012.

[95] C. C. Aggarwal *et al.*, "Neural networks and deep learning", *Springer*, vol. 10, pp. 978–3, 2018. DOI: 10.1007/978-3-319-94463-0.

[96] M. T. Hagan, H. B. Demuth, and M. Beale, *Neural network design*. PWS Publishing Co., 1997.

[97] F. Chollet, *Deep Learning with Python*, 2nd ed. Manning Publications, 2021.

[98] S. S. Haykin, *Neural networks and learning machines*, 3rd ed. Pearson Education, 2009.

[99] F. Rosenblatt, "The perceptron: A probabilistic model for information storage and organization in the brain.", *Psychological review*, vol. 65 6, pp. 386–408, 1958.

[100] X. Glorot, A. Bordes, and Y. Bengio, "Deep sparse rectifier neural networks", in *International Conference on Artificial Intelligence and Statistics*, 2011.

[101] J. R. R. A. Martins and A. Ning, *Engineering Design Optimization*. Cambridge University Press, 2021. DOI: 10.1017/9781108980647.

[102] D. Nix and A. Weigend, "Estimating the mean and variance of the target probability distribution", in *Proceedings of 1994 IEEE International Conference on Neural Networks (ICNN'94)*, vol. 1, 1994, pp. 55–60. DOI: https://doi.org/10.1109/ICNN.1994.374138.

[103] A. Khosravi, S. Nahavandi, D. Creighton, and A. F. Atiya, "Lower upper bound estimation method for construction of neural network-based prediction intervals", *IEEE Transactions on Neural Networks*, vol. 22, no. 3, pp. 337–346, 2011. DOI: 10.1109/TNN.2010.2096824.

[104] R. M. Neal, *Bayesian Learning for Neural Networks*. New York, NY: Springer New York, 1996. DOI: https://doi.org/10.1007/978-1-4612-0745-0.

[105] D. J. C. MacKay, "A Practical Bayesian Framework for Backpropagation Networks", *Neural Computation*, vol. 4, no. 3, pp. 448–472, May 1992. DOI: 10.1162/neco.1992.4.3.448.

[106] IACS-REC 47, *Shipbuilding and repair quality standard, rev. 10*, International Association of Classification Societies, https://iacs.org.uk/download/1985, September 2021 [last accessed May 5, 2023].

[107] BMA, *Report of the investigation into the sinking of the "MOL Comfort" in the Indian Ocean*. 120 Old Broad Street, London, EC2N 1AR, UK: Bahamas Maritime Authority (BMA), 2015, September 2015, https://www.bahamasmaritime.com/wp-content/uploads/2020/10/BMA-Investigation-Report-Loss-of-the-MOL-Comfort.pdf [last accessed May 5, 2023].

[108] Sonderforschungsbereich 98 *et al.*, "Ship structure loads and stresses", *Ocean Eng.*, vol. 7, no. 5, pp. 571–658, 1980, ISSN: 0029-8018. DOI: https://doi.org/10.1016/0029-8018(80)90001-3.

[109] A. Teixeira and C. Guedes Soares, "Reliability assessment of plate elements with random properties", *Mar. Technol. Eng.*, vol. 2, pp. 1361–1375, Jan. 2011.

[110] N. J. D. NAGELKERKE, "A note on a general definition of the coefficient of determination", *Biometrika*, vol. 78, no. 3, pp. 691–692, Sep. 1991. DOI: https://doi.org/10.1093/biomet/78.3.691.

Appendix A

Loading Conditions Summary Table

In the present appendix, the mean values associated with the marginal distributions of the four load-related random variables are provided in table form for all 72 loading conditions.

Table A.1: Population mean values of the load-related random variables for each loading condition.

Condition No.	$\mu_{S_{xx}}$ (MPa)	$\mu_{S_{yy}}$ (MPa)	μ_P (kPa)	μ_Q (kN/m)
1	117.76	15.18	110.84	71.41
2	102.39	15.16	110.79	71.41
3	98.43	15.18	110.85	71.41
4	81.76	15.18	110.86	77.78
5	71.20	15.18	110.85	77.78
6	63.90	15.18	110.84	77.78
7	82.64	15.19	110.87	67.70
8	69.24	15.18	110.85	67.70
9	63.68	15.19	110.88	67.70
10	81.01	15.18	110.85	64.33
11	68.69	15.17	110.81	64.33
12	60.72	15.17	110.80	64.33
13	58.18	15.18	110.86	64.12
14	49.32	15.18	110.84	64.12
15	43.34	15.18	110.83	64.12
16	66.73	15.18	110.86	59.55
17	53.72	15.18	110.83	59.55
18	43.27	15.16	110.77	59.55
19	121.60	18.06	120.91	71.41
20	110.57	18.07	120.92	71.41
21	101.51	18.06	120.91	71.41
22	114.60	18.05	120.86	95.22
23	99.85	18.04	120.83	95.22
24	96.33	18.07	120.92	95.22
25	105.92	18.07	120.92	107.12
26	94.12	18.06	120.89	107.12

(Continued on next page)

Table A.1 (Continued).

Condition No.	$\mu_{S_{xx}}$ (MPa)	$\mu_{S_{yy}}$ (MPa)	μ_P (kPa)	μ_Q (kN/m)
27	88.26	18.07	120.92	107.12
28	71.47	18.06	120.89	108.12
29	61.62	18.05	120.86	108.12
30	57.32	18.06	120.90	108.12
31	59.39	18.05	120.87	90.27
32	50.66	18.04	120.85	90.27
33	46.83	18.06	120.90	90.27
34	57.80	18.02	120.76	90.06
35	46.03	18.01	120.73	90.06
36	42.91	18.03	120.81	90.06
37	135.46	21.16	130.86	71.41
38	125.18	21.12	130.76	71.41
39	129.76	21.13	130.77	71.41
40	132.63	21.15	130.83	95.22
41	122.53	21.16	130.87	95.22
42	104.09	21.11	130.71	95.22
43	124.94	21.15	130.85	107.12
44	111.46	21.14	130.81	107.12
45	107.95	21.17	130.91	107.12
46	107.46	21.16	130.87	119.02
47	103.79	21.21	131.02	119.02
48	93.25	21.18	130.94	119.02
49	87.45	21.16	130.88	129.75
50	76.35	21.15	130.83	129.75
51	73.19	21.18	130.93	129.75
52	70.08	21.18	130.94	120.86
53	58.36	21.17	130.90	120.86
54	51.38	21.16	130.88	120.86
55	126.82	26.35	146.05	71.41
56	131.63	25.46	143.54	71.41
57	130.14	24.34	140.36	71.41
58	127.32	26.30	145.91	95.22
59	117.42	26.32	145.95	95.22
60	108.18	26.32	145.94	95.22

(Continued on next page)

Table A.1 (Continued).

Condition No.	$\mu_{S_{xx}}$ (MPa)	$\mu_{S_{yy}}$ (MPa)	μ_P (kPa)	μ_Q (kN/m)
61	120.81	26.29	145.86	107.12
62	115.00	26.33	145.98	107.12
63	108.58	26.34	146.01	107.12
64	132.63	26.23	145.70	119.02
65	123.33	26.25	145.75	119.02
66	115.41	26.23	145.71	119.02
67	115.63	26.34	146.01	142.83
68	104.31	26.34	146.02	142.83
69	95.88	26.34	146.00	142.83
70	111.33	26.33	145.99	151.37
71	99.78	26.35	146.03	151.37
72	88.00	26.32	145.96	151.37